ABSTRACT

Title of Document: VIBRATION OF PERIODIC DRILLSTRINGS WITH LOCAL SOURCES OF RESONANCE

Hajid Alsupie, Doctor of Philosophy, 2016

Directed By: Professor, Amr Baz,
Department of Mechanical Engineering

The vibration of drillstrings is, in general, detrimental to the drilling process and may induce premature wear and damage of the drilling equipment which eventually results in fatigue failures. In this dissertation, a new design of drillstrings is proposed for mitigating such undesirable vibrations in an attempt to avoid wear and premature failures. In the new design, the drillstring is provided with optimally designed and placed periodic inserts which can be either passive or active. The inserts will make the drillstring act as a mechanical filter for vibration transmission. As a result, vibration can propagate along the periodic drillstring only within specific frequency bands called the '***pass bands***' and the vibration is completely blocked within other frequency bands called the '***stop bands'***. The spectral width of these bands can be tuned **actively** according to the nature of the external excitation which can be either passive or active. The inserts are introduce impedance mismatch zones along the vibration transmission path to impede the propagation of vibration along the string. The design and the location of the inserts will be optimized to confine the dominant modes of vibration of the drillstring within the stop bands generated by the periodic arrangement of the inserts in order to completely **block** the propagation of the vibration.

The theory governing the operation of this new class of drillstrings is developed to describe the complex nature of the vibration encountered during drilling operations. The developed model will account for the bending, torsional, and axial vibrations of the drillstring while operating under the influence of "*slip-stick*" frictional torques between the drill-bit at the rock surface, "*bit-bounce*" which make the drill-bit to intermittently lose contact with the rock surface, and the motion of the bit in the **B**ore-**H**ole **A**ssembly "*bit in **BHA***".

Experimental prototypes of the periodic drillstrings are built and tested under various operating conditions to demonstrate the feasibility and effectiveness of the concept of periodic drillstring in mitigating undesirable vibrations. The experimental results are used to validate the developed theoretical model in order to develop a scalable design tool that can be used to predict the dynamical behavior of this new class of drillstrings.

Keywords: *periodic shafts, periodic drillstrings, periodic inserts with internal resonance, theory and experiments*

VIBRATION OF PERIODIC DRILLSTRINGS WITH LOCAL SOURCES OF RESONANCE

By

Hajid Alsupie

Thesis submitted to the Faculty of the Graduate School of the
University of Maryland, College Park, in partial fulfillment
of the requirements for the degree of
Doctor of Philosophy
2016

Advisory Committee:
Professor Amr Baz, (Chair)
Professor William Fourney
Assoc. Professor Nikhil Chopra
Asst. Professor Siddhartha Das
Professor Roberto Celi (Dean's Representative)

© Copyright by
Hajid Alsupie
2016

Table of Contents

Acknowledgements

Special thanks are due to Qatar National Research Foundation (QNRF) for funding this work under grant number NPRP No.: 7-124-2-060.

Thanks are also due to Professors Amr Baz (University of Maryland) and Sadok Sassi (Qatar University) for their invaluable technical inputs and guidance throughout this study.

Thanks are due to my colleague Yaser Alsaffar for his continuous help in the experimental work.

This work would have been impossible without the tireless help of my family.

CHAPTER 1: INTRODUCTION

1.1. Background / Literature Review

1.1.1. Background

In most applications involving drillstrings with emphasize on higher speed operation with greater misalignment and torque, while reducing weight and cost are very critical to the effective operation of practical drillstrings. Because of their high specific stiffness and strength, engineering tailoring capability, high fatigue strength and corrosion resistance, composite materials offer a significant advantage over their metallic counterpart, and consequently composite materials have been applied to modern drillstrings. The demand for drillstrings to operate at higher speeds (near and post resonance) necessitates the implementation of a vibration suppression technique.

El Rahab and Wagner (1994) used vibration absorbers consisting of strips evenly distributed around the cylinder to control its vibration. Napolitano *et al.* (1998) designed two co-cured damped composite torsion shafts using the extension-twist coupling mechanism and embedded constraining layer damping, respectively. They demonstrated, experimentally and analytically, that both concepts provide significant torsion damping. Hu and Huang (1996) developed a general theory for a three-layer damped sandwich shell with viscoelastic core to investigate the damping ability of this approach. Later Chen and Huang (2001) applied constrained layer damping using axial strips covering the whole length of the cylinder and partially covering the circumference. They studied the effect of varying parameters on the damping effectiveness of the technique. In their analysis of the forced vibration of a rotating tapered composite shaft, Kim *et al.* (2001) introduced an equivalent viscous damping coefficient to account for external and internal damping. Song *et al.* (2002) presented a dual approach to control the flexure vibration of a spinning circular composite shaft. The approach is based on both structural tailoring (passive) and adaptive capability using embedded piezoelectric strips that spreads over the entire shaft length. They showed the potential of the technique to enhance the dynamic response characteristics of the shaft and expand its domain of stability.

The dynamical behavior of drillstrings used in the oil or gas industry is very complex and needs to be effectively controlled to avoid undesirable destructive potential. The complexity stems from the fact that typical drillstrings have diameter-to-length ratios in the order of 10^{-5} which is less than that of the average human hair. Furthermore, such very slender drillstrings are subjected to complex vibrational phenomena that include: torsional relaxation oscillations induced by non-linear "*slip-stick*" frictional torques between the drill-bit at the rock surface, axial vibrations that induce "*bit-bounce*" which make the drill-bit to intermittently lose contact with the rock surface, and whirling motion of the drillstring and the motion of the bit in the **B**ore-**H**ole **A**ssembly *"bit in **BHA"***.

A summary of the different modes of vibrations encountered by the drillstrings and the associated physical mechanisms contributing to such modes is given by Spanos *et al*. (2003) and Table 1 lists these modes and the corresponding mechanisms as reported by Besaisow and Payne (1988).

Table 1- Drillstring excitation mechanisms (Besaisow and Payne, 1988)

Physical Mechanism	Primary Excitation	Secondary Excitation
Mass Imbalance	Lateral	Axial-Torsional-Lateral
Misalignment	Lateral	Axial
Three-cone bit	Axial	Torsional-Lateral
Loose drillstring	Axial-Torsional-Lateral	
Rotational walk	Lateral	Axial-Torsional
Asynchronous Walk or Whirl	Lateral	Axial-Torsional
Drillstring Whip	Lateral	Axial-Torsional

1.1.2 Literature Review

Extensive efforts have therefore been exerted during the past decades to understand the underlying physical phenomena governing such complex vibration behavior of the drillstrings in order to develop appropriate means for mitigating the resulting destructive effects. These efforts include mathematical modeling, simulation, and/or experimental investigation. Examples of these efforts include the work of Aarrested *et al*. (1986), Jansen (1991), Chen and Geradin (1995), Yigit and Christoforou (1996-2000), Christoforou and Yigit (1997-2003), Leine *et al.* (2002), Al-Hiddabi *et al*. (2003), Spanos *et al*., (2003), Khulief and Al-Nasr (2005), Khulief *et al*. ((2007, 2008), Khuleif and Al-Sulaiman (2009), Mihajlović *et al*. (2005-2006), Hoie (2012), Esmaeili *et al*. (2012), Boussaada *et al.* (2012), Ghasemloonia *et al.* (2013), and Liu *et al*. (2014*a*,*b*).

In 1986, Aarrested *et al*. presented the first theoretical and experimental investigation of the vibration of full-scale drilling rig. In 1991, Jansen modeled the bottom-hole-assembly (*BHA*) to study the nonlinearities due to the interaction between the drillstring and the outer shell. Chen and Geradin (1995) presented a finite element model of transverse vibration of drillstrings under axial loading. A linear finite element model has been developed by Khulief and Al-Naser, (2005) to predict the buckling loads and critical rotational speeds of drillstrings. In 1996 and 1998, Yigit and Christoforou developed finite element models to study the coupled torsional and bending vibration as well as the axial and transverse vibrations of passive drillstrings. In 2000 and 2003, their models were extended to simulate the dynamics of drillstrings with active control capabilities. Similar attempt has been reported by Al-Hiddabi *et al*. (2003) to control the nonlinearly coupled torsional and bending vibration of drillstrings. The effect of interaction with the bore hole has been analyzed theoretically by Christoforou and Yigit (1997) and both theoretically and experimentally by Melakhessou *et al.* (2003).

The effect of stick-slip and whirl vibrations on the stability and bifurcation of drillstrings were studied by Leine *et al.* (2002) using a two degrees-of-freedom model. In 2006, Mihajlović *et al*. presented an extensive study of the limit cycles of torsional vibrations of drillstrings subjected to constant input torque. Also, the equilibrium points are determined and related stability properties are discussed. In 2007, Khulief *et al*. extended their finite element model to study the dynamics of drillstring system in the presence of stick–slip excitations.

Several attempts have been carried out to suppress passively the vibration of drillstrings. Distinct among these attempts are the nonlinear energy sink approach of Ahmadabadi and Khadem (2013), the magnetoreheological damping method of Zhu and Lai (2012), the adjustable vibration

absorber of Moradi *et al*. (2012), and the anti-stalling technology (AST) and V-stab vibration reduction tools of Aldushaashi (2012).

In parallel to these attempts, other active control studies using simple active control algorithms have been considered (*e.g*. Yigit and Christoforou 2000, Sarker *et al*. 2012). However, these control methods are no longer suitable for handling the complex nature of the drillstring dynamics and account adequately for the numerous sources of uncertainties resulting from friction, weight-on-hook, as well as interaction models between bit and rocks [Ritto *et al*. (2009*a*,*b*, 2010, and 2013)]. Therefore, extensive efforts have been exerted to develop more sophisticated control methods that can accommodate parameter uncertainty and reject the effect of disturbances. Among these methods are those developed by Al-Hiddabi *et al*. (2003), Karkoub *et al*. (2010), Li *et al*. (2011), and Downton (2012).

In all the above mentioned studies, the emphasis has been placed on conventional drillstrings of uniform cross sections. No attempt has been made to considering radically different designs such as periodic drillstrings in spite of the potential of this class of drillstrings in minimizing the vibration transmission. **It is therefore the purpose of this dissertation to introduce the concept of periodic drillstrings, and demonstrate theoretically and experimentally its unique mechanical filtering characteristics.** Our efforts will focus on developing the theory governing the operation of this new class of drillstrings to account for the simultaneous bending, torsional, and axial vibrations. Experimental prototypes will be built and tested to demonstrate the feasibility of the concept of periodic drillstring in mitigating undesirable vibrations. The experimental results will be used to validate the theoretical model in order to develop a scalable design tool that can be used to predict the dynamical behavior of this new class of drillstrings.

1.1.3. Motivation

Periodic structures, whether passive or active, are structures that consist of identical substructures, or cells, connected in an identical manner. The periodicity can be introduced either by geometrical or material discontinuities as shown in Figure (1.1). Because of such periodicity, these periodic structures exhibit unique dynamic characteristics that make them act as mechanical filters for wave propagation. As a result, waves can propagate along the periodic structures only within specific frequency bands called the ‘pass bands’ and wave propagation is completely blocked within other frequency bands called the ‘stop bands’. The spectral width of these bands can be tuned actively according to the nature of the external excitation (Asiri *et al*., 2005-2006; Baz, 2001).

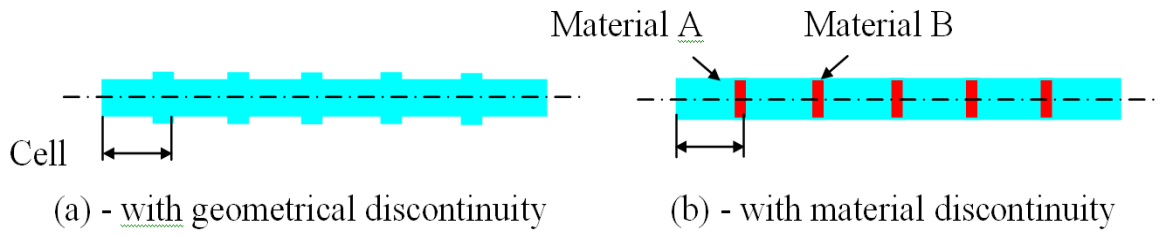

(a) - with geometrical discontinuity (b) - with material discontinuity

Figure (1.1) – Types of passive periodic structures

The finite element equations of a typical periodic structure can be rewritten as (Asiri *et al*., 2005-2006; Baz, 2001):

$$\begin{Bmatrix} u_L \\ F_L \end{Bmatrix}_{k+1} = \begin{bmatrix} t_{11} & t_{12} \\ t_{21} & t_{22} \end{bmatrix} \begin{Bmatrix} u_L \\ F_L \end{Bmatrix}_k \quad or \quad S_{k+1} = [T_k] S_k \tag{1.1}$$

where S and $[T_k]$ denote the state vector = $\{u_L \quad F_L\}^T$ and the transfer matrix of the k^{th} cell. Note that the transfer matrix relates the state vector at the left end of $k+1^{th}$ cell to that at the left end of the k^{th} cell. Also, note that u_L and F_L define the deflection and force vectors.

Equation (1.1) can also be writes as (Asiri *et al.*, 2005-2006; Baz, 2001):

$$S_{k+1} = \lambda S_k \tag{1.2}$$

indicating that the eigenvalue λ of the matrix $[T]$ is the ratio between the state vectors at two consecutive cells.

Therefore, one can draw the following conclusions:

i. If $|\lambda| = 1$, then $S_{k+1} = S_k$ and the state vector propagates along the structure as is. This condition defines a "***Pass Band***" condition.

and ii. If $|\lambda| < 1$, then $S_{k+1} < S_k$ and the state vector is attenuated as it propagates along the structure. This condition defines a "***Stop Band***" condition.

A further explanation of the physical meaning of the eigenvalue λ can be extracted by rewriting it as:

$$\lambda = e^{\mu} = e^{\alpha + i\beta} \tag{1.3}$$

where μ is defined as the "*Propagation Constant*" which has a real part (α) = the logarithmic decay and imaginary part (β) = the phase difference between the adjacent cells.

Asiri *et al*., 2006 showed that plain struts (rods) can act as wave guides that not only transmit completely the vibration from one end to the other but also can amplify the vibration at the structural resonances as indicated in Figure (1.2) by the grey lines. Using passive periodic struts result in completely blocking the transmission of vibration at frequencies above 600 Hz. This is indicated by the blue characteristics in Figure (1.2). This range is extended to almost 0Hz when the periodic strut is provided with active control capabilities as shown by the green lines in Figure (1.2).

The displayed characteristics indicate that the periodic strut behaves as a low pass mechanical filter. Also, the periodic struts generate a non-zero apparent damping, throughout the stop band, which is quantified by the parameter α shown in Figure (1.2-b) for plain, passive periodic, and active periodic struts. For plain struts, α =0 suggesting that all the vibration will be transmitted while α is high for passive periodic struts and much higher and broader for the active periodic struts.

Such unique characteristics can be further emphasized by considering the vibration contour plots shown in Figure (1.3) for plain, passive periodic, and active periodic struts at different frequency of excitation.

It is evident that vibration transmission can be effectively blocked by introducing periodicity along the structure. **We will therefore attempt to extend this well-proven technology to drillstrings to minimize their vibrations and extend their service life by avoiding premature wear and failure due to excessive and undesirable vibrations**.

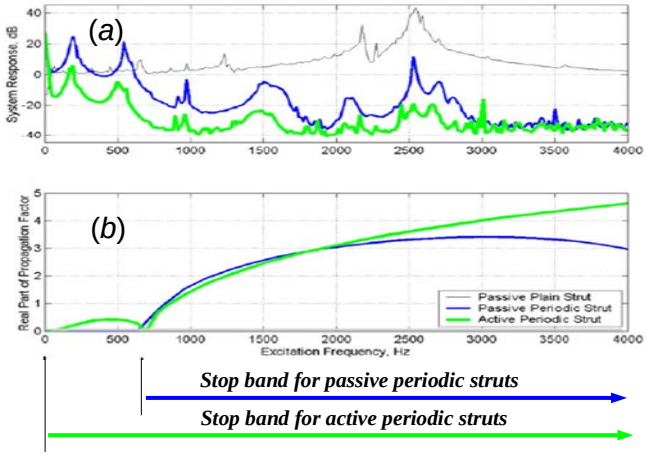

Figure (1.2) – Typical characteristics of passive and active periodic structures

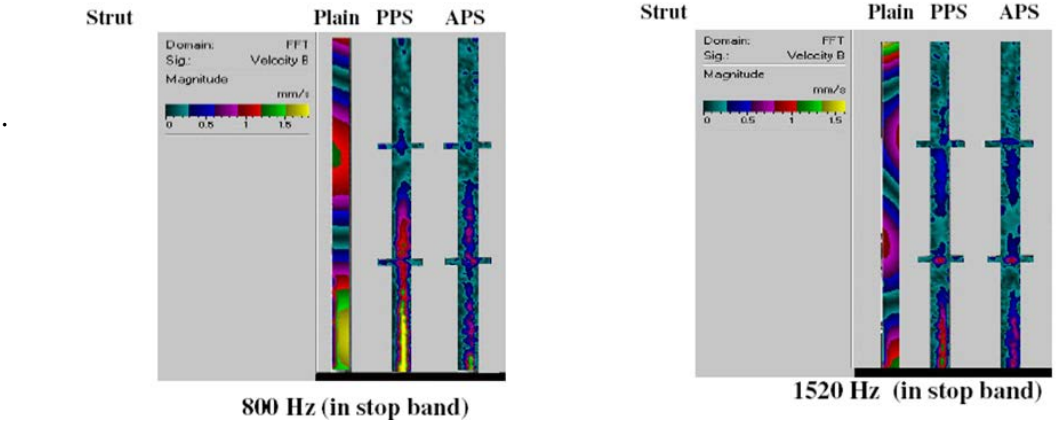

Figure (1.3) – Vibration contour maps for plain, passive (*PPS*) and active periodic (*APS*) struts

1.2. Concept of Passive Drillstrings with Periodic Inserts and Periodic Local Resonances

The concept of the periodic drillstring can best be understood by considering the schematic drawings shown in Figures (1.4a) and (1.4b).

In Figure (1.4a), the periodic drillstring will be provided with optimally designed and placed periodic inserts which can be either passive or active. The passive inserts will introduce zones of impedance mismatch along the vibration transmission path to impede the propagation through geometrical or material discontinuities. On the other hand, the active inserts will be computer-controlled to tune and enhance the mechanical filtering characteristics of the drillstring.

In the passive periodic drillstrings, the design and the location of the inserts will be optimized to confine the dominant modes of vibration of the drillstring within the stop bands generated by the periodic arrangement of the inserts.

It is important to note that the concept and filtering characteristics of periodic drillstring is particularly suitable for mitigating and blocking the vibration over a wide range of drilling depths as shown in Figure (1.4b). The figure indicates that at shallow drilling depth, the drillstring dominant natural frequency is usually high and is bound to lie inside the stop band. But, as the drilling depth becomes deeper, the drillstring becomes longer and softer, hence is likely to vibrate at higher amplitudes. But, if the periodic inserts are designed properly, either passively or actively, then the corresponding dominant natural frequency can still be maintained confined within the stop band. Hence, the expected severe vibrations can be completely blocked. This is unlike the current passive or active conventional drillstrings which are tuned to operate effectively **only at one operating condition** (either speed or drilling depth).

A promising new direction would be achieved by augmenting the periodic drillstring with "local resonance" capabilities in order to extend its "stop band" characteristics to low frequency zones. Such capabilities will enable operating the drillstrings at low speeds which in turn will result in reducing the induced vibrations. This class of periodic drillstrings will consist of a conventional drillstring with periodic inserts that have cavities which house resonating masses connected to the cavity wall by springs and dampers. The macroscopic dynamical properties of the resulting periodic drillstrings depend on the resonant properties of substructures which contribute to the rise of interesting effects such as broad stop band characteristics which can be adjusted by tuning of the local resonance sources. Figure (1.4) shows typical schematic drawings of a drillstring structure with periodic inserts fitted with local sources of resonances.

The potential application spectrum of the proposed new class of periodic drillstrings is envisioned to be beneficial to improving the quality and the state-of-the-art of drilling operations both in land and in sea. Furthermore, this spectrum is only limited by our imagination.

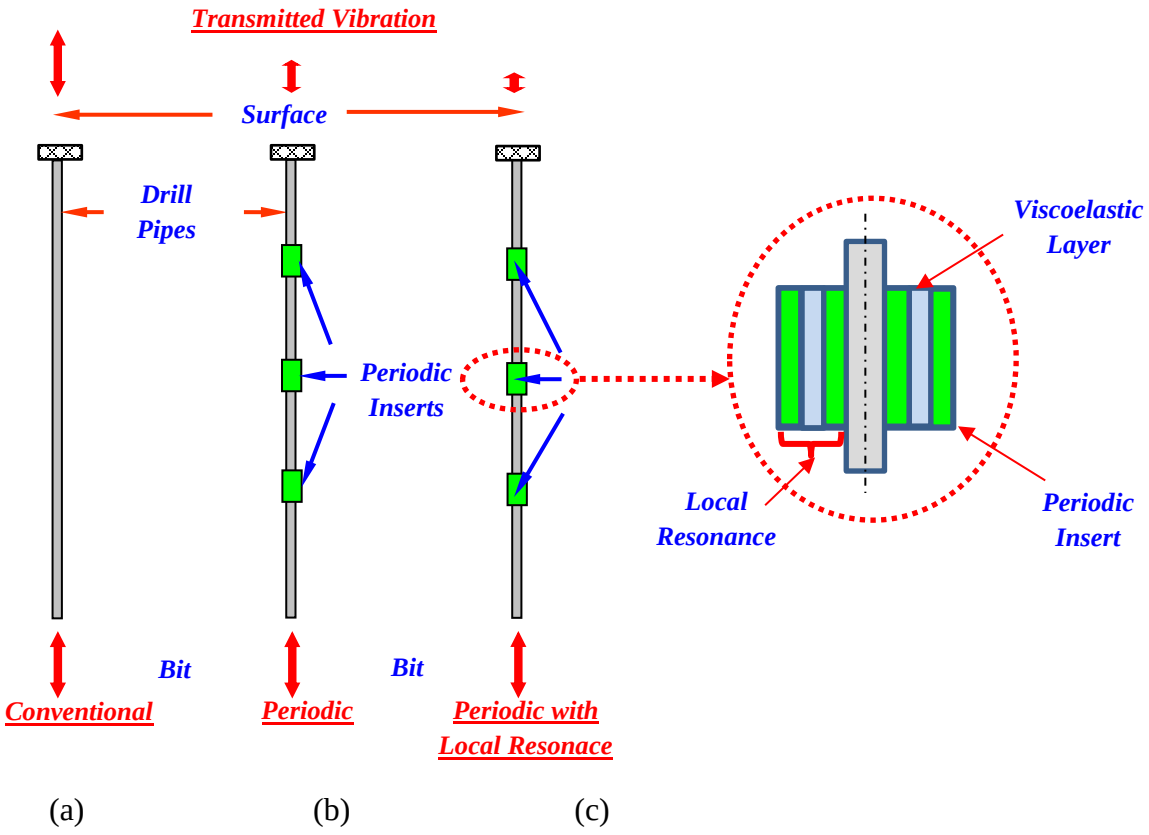

Figure (1.4) : Schematic drawings and characteristics of conventional and periodic drillstrings

Figure (1.4c) shows a special class of periodic structures with local sources of resonances. This class of structures have been introduced because of their unusual response to elastic wave propagation as has been recently reported, for example, by Liu *et al*. (2005), Milton and Willis (2007), Huang and Sun (2011), Zhou and Hu (2013), and Hussein and Frazier (2013).

This class of structures is distinctly different from conventional periodic structures as shown in Figure (1.5). In conventional periodic structures, as shown in Figure (1.5a), the unit cell consists of spring-mass assembly. Figure (1.5b) displays the second class of structures which has periodic assembly of mass-in-mass and spring assembly whereby the internal mass-spring subassembly acts as a local source of internal resonance. The macroscopic dynamical properties of the resulting periodic structures depend on the resonant properties of substructures which contribute to the rise of interesting effects such as broad stop band characteristics.

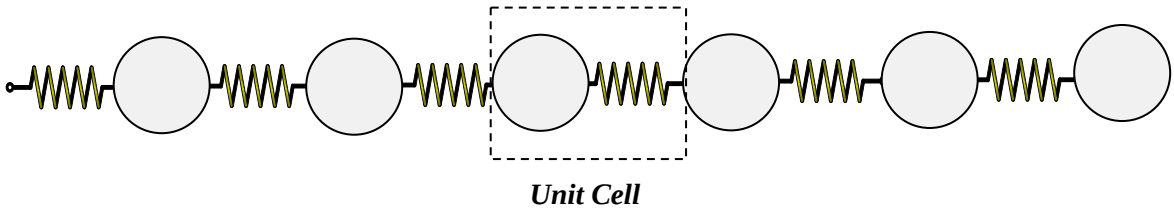

(a) - conventional periodic structure

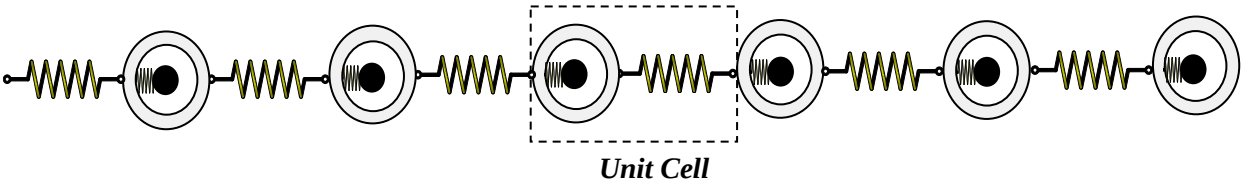

(b)– periodic structure with local resonances
(Milton and Willis, 2007; Huang and Sun, 2011)

Figure (1.5) - Periodic structures with and without local resonances

A physical realization of the periodic structure with local resonances is reported by Nouh et al. (2014) whereby a 1-D metamaterial beam-like configuration is manufactured as displayed in Figure (1.6). In the considered configuration, the metamaterial beam is manufactured of assemblies of periodic cells with built-in local resonances. Each cell consists of a base beam-like structure which is provided with cavities filled by a viscoelastic membrane that supports a small mass to form a source of local resonance. The resemblance between the idealized configuration of Figure (1.5b) and its physical realization of Figure (1.6) can be easily seen by comparing the unit cells of each configuration.

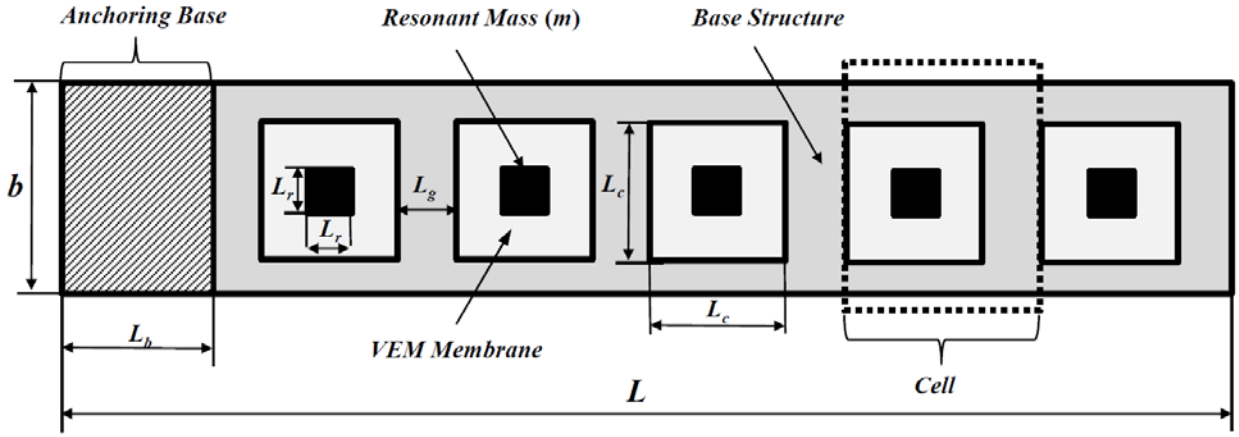

Figure (1.6) – Beam-like structure with periodic sources of local resonances

The benefit of using structures with periodic sources of local resonances is evident from the broad stop band characteristics displayed in Figure (1.7) as reported by Nouh *et al.* (2014).

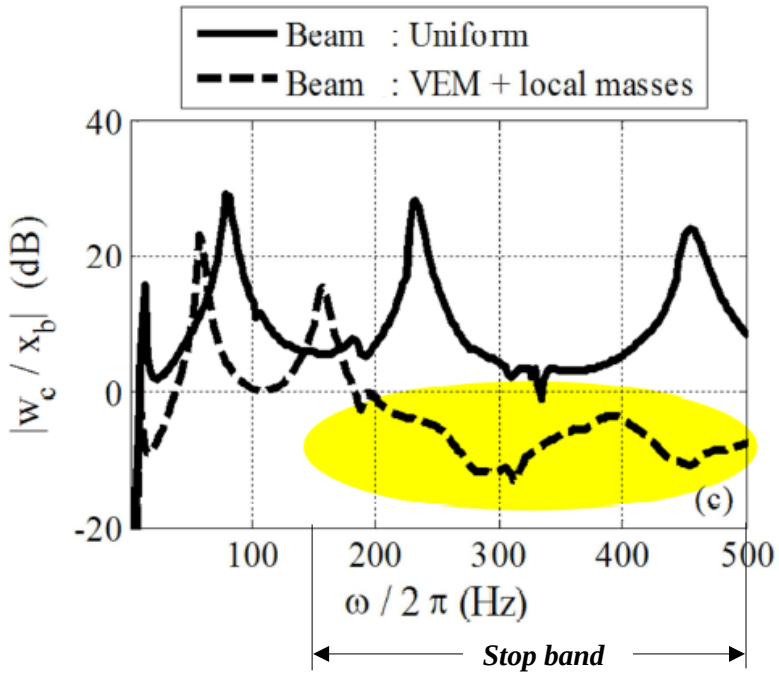

Figure (1.7) – Stop band characteristics of beam-like structure with periodic sources of local resonances (Nouh *et al.*, 2014)

Such a concept will be utilized and extended to the application of periodic inserts with sources of local resonance to the control of the vibration of rotating shafts and drillstrings.

1.3. SCOPE OF THE DISSERTATION

This dissertation aims at extending the current state-of-the-art of the field of periodic structures by developing a class of rotating structures with periodic inserts with sources of local resonance in order to the control of the vibration of rotating shafts and drillstrings. Such a development will constitute the major contribution of this dissertation.

The development of such a class of structures will involve the development of finite element modeling (*FEM*) to describe the dynamics and vibrations of rotating structures at different rotating speeds. The developed *FEM* will be exercised to generate the equivalent transfer matrix method of the rotating structures. The transfer matrices will be utilized to study the pass and stop

band characteristics of the rotating structures as influenced by the design parameters of the local sources of resonances. It is envisioned that the proposed class of periodic structures will have enhanced ability of operating over frequency bands that are wider than those possible with conventional periodic structures.

The effectiveness of the proposed periodic inserts with local resonances will be demonstrated numerically. The predictions of the numerical models will be validated experimentally for prototypes of the rotating shafts.

Comparisons will also be established between the performance of the proposed periodic inserts with local resonances and that of conventional periodic inserts in order to emphasize the potential and merits of the proposed approach.

1.4. ORGANIZATION OF THE DISSERTATION

In order to achieve the goals presented in the scope of the dissertation section, this dissertation is organized in six chapters. In chapter 1, a brief introduction is presented. In chapter 2, the development of a finite element model is described to simulate the dynamics and vibration of rotating shafts with periodic inserts with local resonances. In chapter 3, the finite element model will be utilized to generate the transfer matrix of the unit cell which governs the wave propagation through the rotating shaft system. In chapter 4, the predictions of the finite element models will be validated against the predictions of commercial finite element package (*ANSYS*). In chapter 5, further validation of the predictions of the *FEM* will be carried out against the performance of experimental prototype of the rotating shaft. In chapter 6, a brief summary will be presented of the conclusions of the arrived at theoretical and experimental results. Furthermore, a brief summary of the future work are outlined in chapter 6.

1.5. SUMMARY

This chapter has presented a brief review of the field of the vibration of rotating shafts and conventional periodic structures. Furthermore, this chapter has outlined the scope and organization of this dissertation where the focus is placed on extending the current state-of-the-art by developing a new approach to the vibration control of rotating shafts by using periodic inserts with built-in sources of local resonances. Such a development will constitute the major contribution of this dissertation.

Chapter 2: Finite Element Modeling of Drillstrings with Periodic Sources of Local Resonance

2.1. Overview

This chapter presents the development of a finite element model to predict the dynamics and characteristics of drillstrings and rotating shafts with periodic sources of local resonance such as shown in Fig. 2.1. The model development will involve the derivation of expressions of the potential and kinetic energies of the shaft assembly. Expressions of the energy dissipated in the damping treatments and the work done by all external forces acting on the shaft assembly will also be developed.

The theory of finite elements with appropriate interpolating functions will be utilized to determine the stiffness and mass matrices of the assembly as well as the dissipative forces and external forces acting of the shaft system.

Lagrange dynamics approach will then be employed to extract the equations of motion of the shaft assembly. The resulting equations of motion will be exercised to predict the performance characteristics of the shaft assembly at different rotational speeds and design parameters. Distinct between the considered performance characteristics are the model parameters of the assembly, the stop and pass band behavior, and Campbell diagram.

The predicted characteristics will be validated, in chapter 3, against the predictions of the commercial finite element code *ANSYS*. Furthermore, the developed finite element model will be utilized to extract the transfer matrix of the assembly as will outlined in chapter 4 in order to validate the predictions of the stop and pass band behavior of the shaft system.

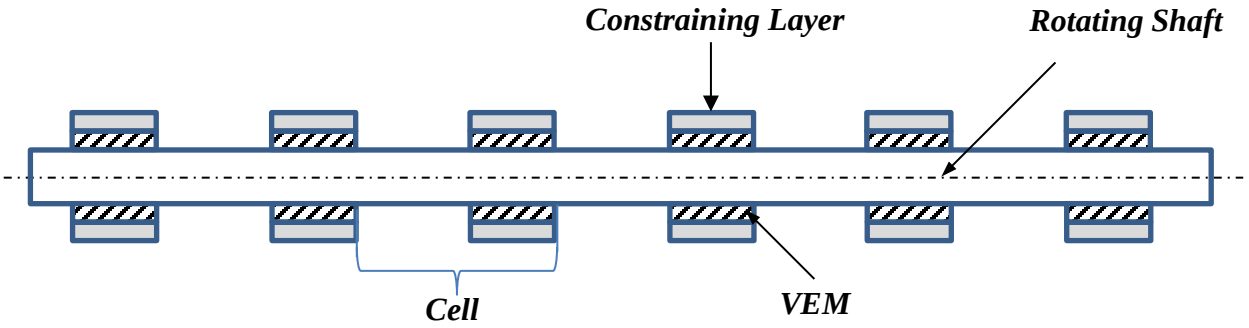

Figure (2.1) - Drillstring shaft with periodic sources of local resonance

2.2. Finite Element Model

In this section, the equations of motion of the unit cell of the drillstring assembly, shown in Figure (2.2), is developed.

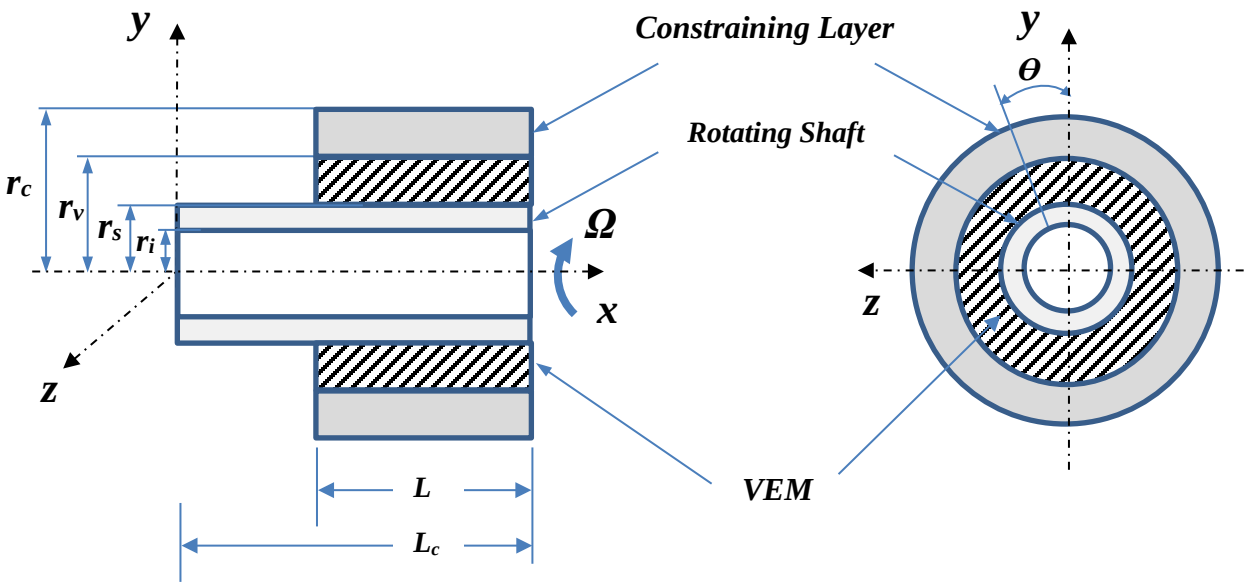

Figure (2.2) - Unit cell of the rotating drillstring with periodic inserts that have built-in local resonance

2.2.1. Kinetic Energy of the drillstring/Sources of Local Resonance

A. Kinematics of the Shaft

The kinematic of the drillstring shaft can best be understood by considering the geometrical configurations of the un-deflected and deflected shafts as displayed in Figure (2.3). Two coordinate systems are associated with the shaft. These coordinate systems are the inertial and the body-fixed systems (X, Y, Z) and (x', y', z') respectively.

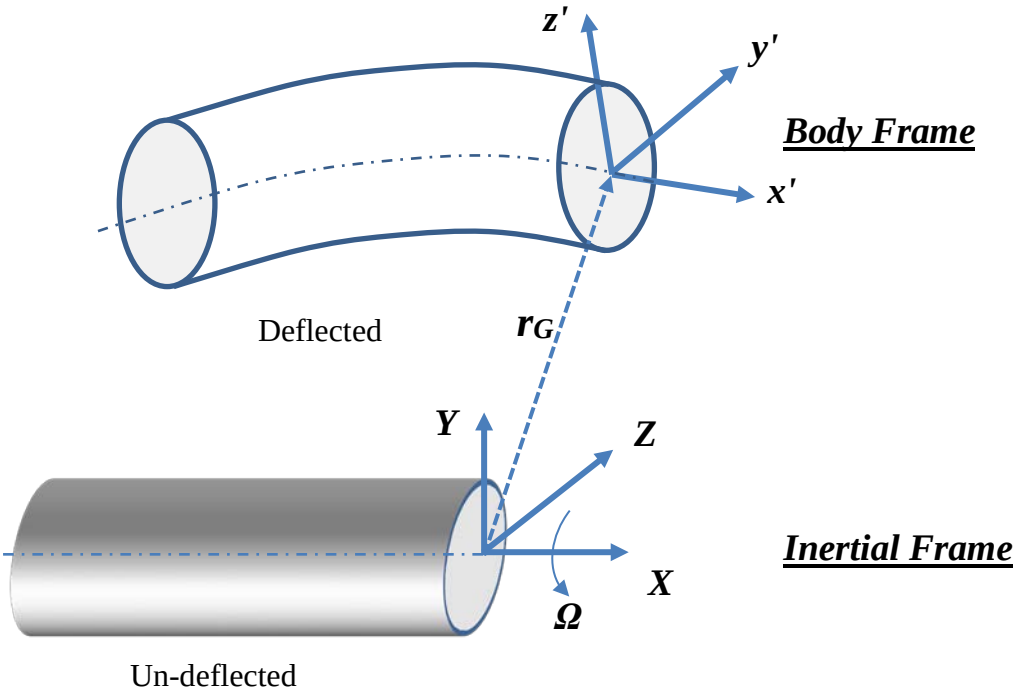

Figure (2.3) – Basic geometrical parameters of the drillstring shaft

A close-up of the deflected shaft as shown in Figure (2.4) displays the position vectors of any point *P* and the *C.G.* of the shaft cross section *G*.

The figure displays also the different rotations experienced by the shaft around the z, y, and x axes respectively. These rotations are namely β_y, β_x and $\psi = \phi + \Omega t$ with ϕ and Ω denoting the twist angle of the shaft and spinning speed of the shaft respectively. Note that the spinning speed Ω is assumed constant in this dissertation.

Based on the geometry of the deflected configuration,

$$\mathbf{R_P} = \mathbf{R_G} + \mathbf{R_{P/G}} \tag{2.1}$$

which can be rewritten as follows:

$$\mathbf{R_P} = \left(u_s\mathbf{i} + v_s\mathbf{j} + w_s\mathbf{k}\right) + \left(y'\mathbf{j}' + z'\mathbf{k}'\right) \tag{2.2}$$

where u_s, v_s, w_s are the global coordinates of the *C.G.* of the shaft cross section following its deflection. Also, $\mathbf{i},\mathbf{j},\mathbf{k}$ are unit vectors associated with the global inertial coordinate system. Furthermore, y',z' are the local coordinates of point P relative to the local body-fixed coordinate system that has the unit vectors $\mathbf{i}',\mathbf{j}',\mathbf{k}'$.

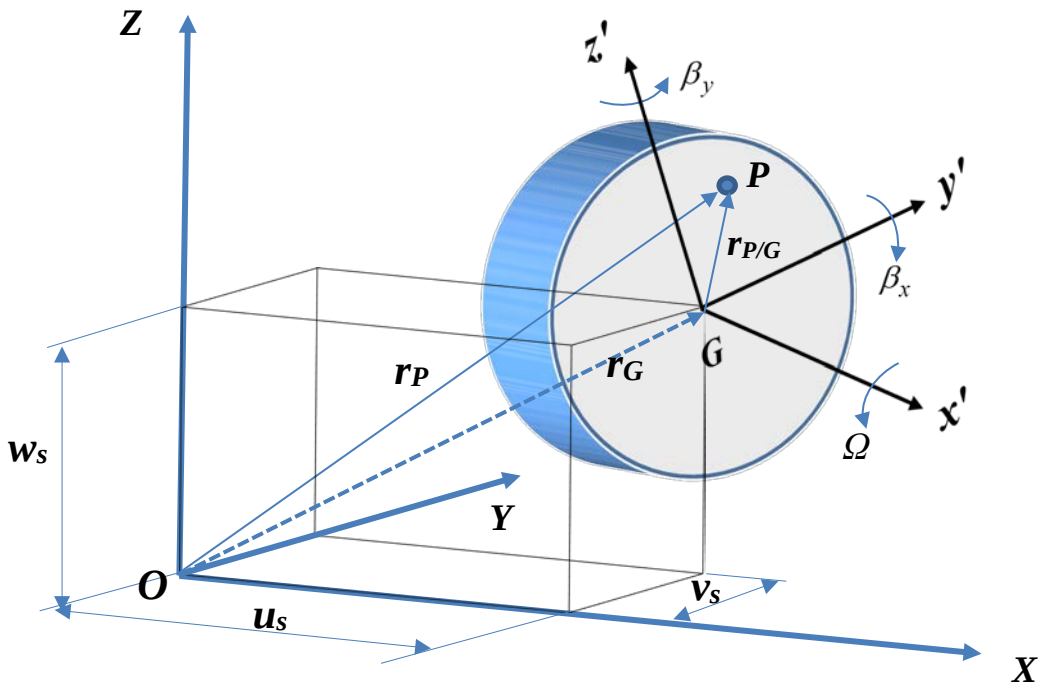

Figure (2.4) – Close-up of the parameters of the deflected shaft

Using NASA's standard Euler angle transformations 3-2-1, then:

$$[R_1]=\begin{bmatrix} c\beta_y & s\beta_y & 0 \\ -s\beta_y & c\beta_y & 0 \\ 0 & 0 & 1 \end{bmatrix},\quad [R_2]=\begin{bmatrix} c\beta_x & 0 & -s\beta_x \\ 0 & 1 & 0 \\ s\beta_x & 0 & c\beta_x \end{bmatrix},\quad [R_3]=\begin{bmatrix} 1 & 0 & 0 \\ 0 & c\phi & s\phi \\ 0 & -s\phi & c\phi \end{bmatrix} \qquad (2.3)$$

Then, total transformation matrix [*R*]:

$$[R]=[R_3][R_2][R_1],\ \text{and}\ \begin{Bmatrix} \mathbf{i}' \\ \mathbf{j}' \\ \mathbf{k}' \end{Bmatrix}=[R]^{-1}\begin{Bmatrix} \mathbf{i} \\ \mathbf{j} \\ \mathbf{k} \end{Bmatrix}. \qquad (2.4)$$

Using the following approximations which are based on small angle deflections:

then $c\beta_x=1, s\beta_x=0, c\beta_y=1,$ and $s\beta_y=0$. With these approximations, equation (2.4) reduces to:

$$\begin{Bmatrix}\mathbf{i}'\\ \mathbf{j}'\\ \mathbf{k}'\end{Bmatrix}=[R]^{-1}\begin{Bmatrix}\mathbf{i}\\ \mathbf{j}\\ \mathbf{k}\end{Bmatrix}=\begin{bmatrix}1 & \left(\beta_x s\phi-\beta_y c\phi\right) & \left(\beta_x c\phi+\beta_y s\phi\right)\\ \beta_y & \left(\beta_x\beta_y s\phi+c\phi\right) & \left(\beta_x\beta_y c\phi-s\phi\right)\\ -\beta_x & s\phi & c\phi\end{bmatrix}\begin{Bmatrix}\mathbf{i}\\ \mathbf{j}\\ \mathbf{k}\end{Bmatrix} \tag{2.5}$$

Substituting equation (2.5) into equation (2.2), it reduces to:

$$\mathbf{R_P = R_G + R_{P/G}}$$

$$\begin{aligned}
&=\left(u_s\mathbf{i}+v_s\mathbf{j}+w_s\mathbf{k}\right)+\left(y'\mathbf{j}'+z'\mathbf{k}'\right)\\
&=\begin{Bmatrix}u_s & v_s & w_s\end{Bmatrix}\begin{Bmatrix}\mathbf{i}\\ \mathbf{j}\\ \mathbf{k}\end{Bmatrix}+\begin{Bmatrix}0 & y' & z'\end{Bmatrix}\begin{Bmatrix}\mathbf{i}'\\ \mathbf{j}'\\ \mathbf{k}'\end{Bmatrix}\\
&=\begin{Bmatrix}u_s & v_s & w_s\end{Bmatrix}\begin{Bmatrix}\mathbf{i}\\ \mathbf{j}\\ \mathbf{k}\end{Bmatrix}+\begin{Bmatrix}0 & y' & z'\end{Bmatrix}\begin{bmatrix}1 & \left(\beta_x s\phi-\beta_y c\phi\right) & \left(\beta_x c\phi+\beta_y s\phi\right)\\ \beta_y & \left(\beta_x\beta_y s\phi+c\phi\right) & \left(\beta_x\beta_y c\phi-s\phi\right)\\ -\beta_x & s\phi & c\phi\end{bmatrix}\begin{Bmatrix}\mathbf{i}\\ \mathbf{j}\\ \mathbf{k}\end{Bmatrix}\\
&=\left[u_s+\left(\beta_x s\phi-\beta_y c\phi\right)y'+\left(\beta_x c\phi+\beta_y s\phi\right)z'\right]\mathbf{i}\\
&+\left[v_s+\left(\beta_x\beta_y s\phi+c\phi\right)y'+\left(\beta_x\beta_y c\phi-s\phi\right)z'\right]\mathbf{j}\\
&+\left[w_s+s\phi\,y'+c\phi\,z'\right]\mathbf{k}
\end{aligned} \tag{2.6}$$

Differentiating equation (2.6) with respect to the time, yields the velocity of point P relative to the inertial frame of reference as follows:

$$\begin{aligned}
\mathbf{\dot{R}_P = \dot{R}_G + \boldsymbol{\omega}\times R_{P/G}}\\
&=\left(\dot{u}_s\mathbf{i}+\dot{v}_s\mathbf{j}+\dot{w}_s\mathbf{k}\right)+\boldsymbol{\omega}\times\begin{Bmatrix}0 & y' & z'\end{Bmatrix}[R]^{-1}\begin{Bmatrix}\mathbf{i}\\ \mathbf{j}\\ \mathbf{k}\end{Bmatrix}
\end{aligned} \tag{2.7}$$

where $\boldsymbol{\omega}$ is the rotation vector the shaft which can be determined in terms of the Euler angles β_y, β_x and ϕ as follows (Baruh, 1999):

$$\begin{Bmatrix}\omega_1\\ \omega_2\\ \omega_3\end{Bmatrix}=\begin{Bmatrix}\dot{\phi}+\Omega\\ \dot{\beta}_x\\ \dot{\beta}_y\end{Bmatrix}+\begin{bmatrix}0 & 0 & -s\beta_x\\ 0 & c\beta_y-1 & c\beta_x s\beta_y\\ 0 & -s\beta_y & c\beta_x c\beta_y-1\end{bmatrix}\begin{Bmatrix}\dot{\phi}+\Omega\\ \dot{\beta}_x\\ \dot{\beta}_y\end{Bmatrix} \tag{2.8}$$

Using small angle approximation and neglecting the higher order terms, equation (2.8) reduces to:

$$\begin{Bmatrix}\omega_1\\ \omega_2\\ \omega_3\end{Bmatrix}\cong\begin{Bmatrix}\dot{\phi}+\Omega\\ \dot{\beta}_x\\ \dot{\beta}_y\end{Bmatrix} \quad or \quad \boldsymbol{\omega}\cong\left(\dot{\phi}+\Omega\right)\mathbf{i}'+\dot{\beta}_x\mathbf{j}'+\dot{\beta}_y\mathbf{k}' \tag{2.9}$$

Combining equations (2.7) and (2.9) yields:

$$\begin{aligned}\dot{\mathbf{R}}_\mathbf{P} &= \dot{\mathbf{R}}_\mathbf{G}+\boldsymbol{\omega}\times\mathbf{R}_{\mathbf{P/G}}\\ &=\left(\dot{u}_s\mathbf{i}+\dot{v}_s\mathbf{j}+\dot{w}_s\mathbf{k}\right)+\left(\left[\dot{\phi}+\Omega\right]\mathbf{i}'+\dot{\beta}_x\mathbf{j}'+\dot{\beta}_y\mathbf{k}'\right)\times\left\{0 \quad y'\mathbf{j}'+z'\mathbf{k}'\right\}\\ &=\left(\dot{u}_s\mathbf{i}+\dot{v}_s\mathbf{j}+\dot{w}_s\mathbf{k}\right)+\left(\left[z'\dot{\beta}_x-y'\dot{\beta}_y\right] \quad -z'\left[\dot{\phi}+\Omega\right] \quad y'\left[\dot{\phi}+\Omega\right]\right)[R]^{-1}\begin{Bmatrix}\mathbf{i}\\ \mathbf{j}\\ \mathbf{k}\end{Bmatrix}\end{aligned} \tag{2.10}$$

Expanding equation (2.10) yields:

$$\begin{aligned}\dot{\mathbf{R}}_\mathbf{P} &= \left(\dot{u}_s\mathbf{i}+\dot{v}_s\mathbf{j}+\dot{w}_s\mathbf{k}\right)\\ &+\left[\left(\dot{\beta}_x z'-\dot{\beta}_y y'\right)-z'\Omega\beta_y+y'\Omega\beta_x\right]\mathbf{i}\\ &+\left[-\beta_y\left(\dot{\beta}_x z'-\dot{\beta}_y y'\right)-z'\left(\dot{\phi}+\Omega\right)+y'\Omega\phi\right]\mathbf{j}\\ &+\left[\ \beta_x\left(\dot{\beta}_x z'-\dot{\beta}_y y'\right)+z'\phi\Omega-y'\left(\dot{\phi}+\Omega\right)\right]\mathbf{k}\end{aligned} \tag{2.11}$$

B. The Kinetics Energy of the Shaft

The kinetic energy of the shaft can be determined from:

$$
\begin{aligned}
T_s &= \frac{1}{2}\int_V \rho_s \left(\dot{\mathbf{R}}_\mathbf{P}.\dot{\mathbf{R}}_\mathbf{P}\right) dV \\
&= \frac{1}{2}\rho_s A_s \int_0^L \left(\dot{u}_s^2 + \dot{v}_s^2 + \dot{w}_s^2\right) dx \\
&+ \frac{1}{2}\rho_s \int_V \left[\left(\dot{\beta}_x z' - \dot{\beta}_y y'\right) - z'\Omega\beta_y + y'\Omega\beta_x\right]^2 dV \\
&+ \frac{1}{2}\rho_s \int_V \left[-\beta_y\left(\dot{\beta}_x z' - \dot{\beta}_y y'\right) - z'\left(\dot{\phi} + \Omega\right) + y'\Omega\phi\right]^2 dV \\
&+ \frac{1}{2}\rho_s \int_V \left[\ \beta_x\left(\dot{\beta}_x z' - \dot{\beta}_y y'\right) + z'\phi\Omega - y'\left(\dot{\phi} + \Omega\right)\right]^2 dV \\
&\cong \frac{1}{2}\rho_s \int_0^L \left[\left(\dot{u}_s^2 + \dot{v}_s^2 + \dot{w}_s^2\right) + \left(\dot{\beta}_x^2 + \dot{\beta}_y^2\right) z'^2 + \left(\dot{\phi}^2 y'^2\right) + \Omega y'^2\right. \\
&\qquad \left. + \left(\beta_x^2 z'^2 + \beta_y^2 y'^2\right)\Omega^2 - 2\left(\beta_x \dot{\beta}_y z'^2\right)\Omega + 2\left(\dot{\phi}\,\Omega\, y'^2\right)\right] dV
\end{aligned}
\tag{2.12}
$$

Note that as:

$$
I_d = \rho\int_V y'^2 dA,\ I_d = \rho\int_V z'^2 dA,\ \text{and}\ I_p = \rho\int_V \left(y'^2 + z'^2\right) dA
$$

Then,

$$
\begin{aligned}
T_s &= \frac{1}{2}\int_0^L \left[\rho_s A_s\left(\dot{u}_s^2 + \dot{v}_s^2 + \dot{w}_s^2\right)\right. \\
&+ \frac{1}{2} I_d\left(\dot{\beta}_{x_s}^2 + \dot{\beta}_{y_s}^2\right) + \frac{1}{2} I_d\left(\beta_{x_s}^2 + \beta_{y_s}^2\right)\Omega^2 \\
&\left. - I_P\,\Omega\,\beta_{x_s}\dot{\beta}_{y_s} + \frac{1}{2} I_P\dot{\phi}^2 + \frac{1}{2} I_P\Omega^2 + I_P\dot{\phi}\Omega\right] dx
\end{aligned}
\tag{2.13}
$$

where ρ_s is the shaft density, A_s is the shaft cross sectional area, L is the length of the shaft element, I_d is the diametrical mass moment of inertia, and I_p is the polar mass moment of inertia. Note that subscript s is used to denote the shaft.

Note that the term $-I_P\,\Omega\,\beta_x\dot{\beta}_y$ defines the kinetic energy due to gyroscopic forces.

C. The Kinetics Energy of the Constraining Layer

The kinetic energy T_c of the constraining layer can be determined in a similar manner as the shaft from:

$$T_c = \frac{1}{2}\int_0^L \Big[\rho_c A_c \left(\dot{u}_c^2 + \dot{v}_c^2 + \dot{w}_c^2\right) + \frac{1}{2} I_{d_c}\left(\dot{\beta}_{x_c}^2 + \dot{\beta}_{y_c}^2\right) + \frac{1}{2} I_{d_c}\left(\beta_{x_c}^2 + \beta_{y_c}^2\right)\Omega^2 - I_{P_c}\,\Omega\,\beta_{x_c}\dot{\beta}_{y_c} + \frac{1}{2} I_{P_c}\dot{\phi}_c^2 + \frac{1}{2} I_{P_c}\Omega^2 + I_{P_c}\dot{\phi}_c\,\Omega \Big] dx \tag{2.14}$$

where u_c, v_c, w_c are the global coordinates of the constraining layer. Also, ρ_c is the density of the constraining layer, A_c is its cross sectional area, L is the length of the constraining layer element, I_{d_c} is the diametrical mass moment of inertia, and I_{P_c} is the polar mass moment of inertia.

Furthermore, β_{y_c} ,β_{x_c} and ϕ_c denote the Euler angles of the constraining layer.

Hence, the total kinetic energy of the element is given by:

$$T_{total} = T_s + T_c \tag{2.15}$$

2.2.2. Potential Energy of the Shaft/Internal Sources of Resonance Element

A. Stresses and Strains in the shaft and constraining Layer

The axial, tangential, and shear strains (ε_{xx}, $\gamma_{x\theta}$,γ_{rx}) at the neutral surface of the shaft are displayed in Figure (2.5).

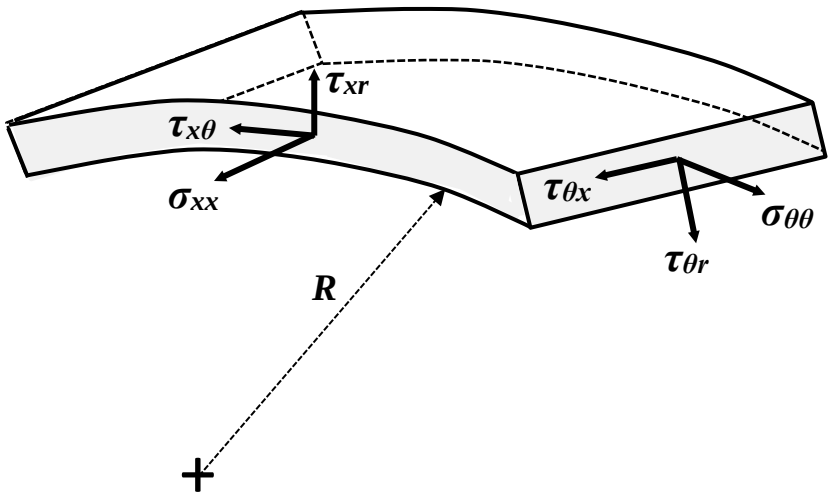

Figure (2.5) – The stress components acting of the shaft element

The displacement field of the shaft element can be described by considering the kinematics of deflected and undeflected shafts shown in Figure (2.6).

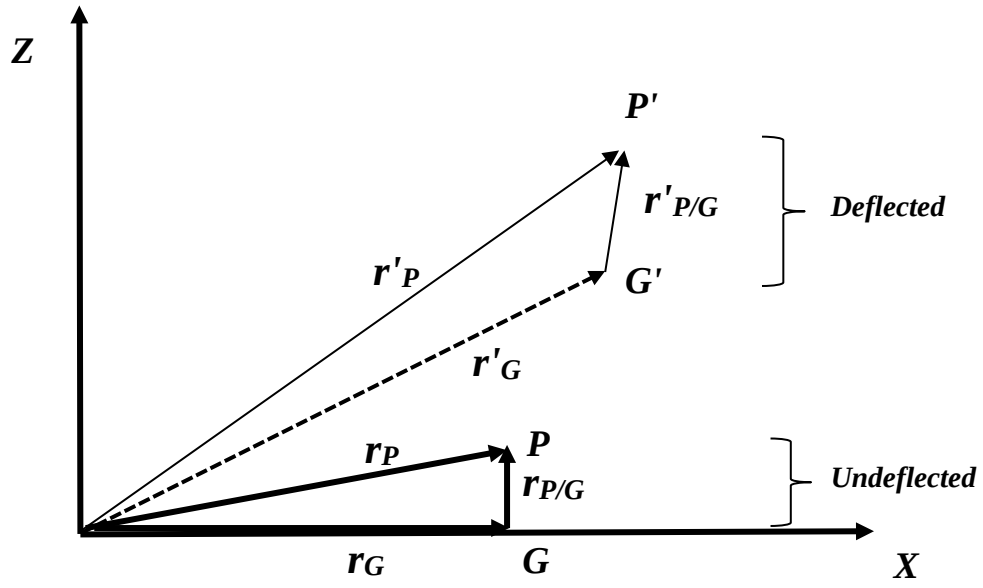

Figure (2.6) – Kinematics of the deflected and undeflected shaft element

As $\mathbf{R_P = R_G + R_{P/G}}$ for the undeflected shaft (2.16)

and $\mathbf{R'_P = R'_G + R'_{P/G}}$ for the deflected shaft (2.17)

But, from equation (2.5), the vector $\mathbf{R'_{P/G}}$ can be written in terms of $\mathbf{R_{P/G}}$ as follows:

$$\mathbf{R'_{P/G}} = [R]^{-1}\mathbf{R_{P/G}} = \begin{bmatrix} 1 & (\beta_x s\phi - \beta_y c\phi) & (\beta_x c\phi + \beta_y s\phi) \\ \beta_y & (\beta_x\beta_y s\phi + c\phi) & (\beta_x\beta_y c\phi - s\phi) \\ -\beta_x & s\phi & c\phi \end{bmatrix}\mathbf{R_{P/G}} \quad (2.18)$$

Using the small angle approximation, equation (2.18) reduces to:

$$\mathbf{R'_{P/G}} = \left(\begin{bmatrix} 1 & 0 & 0 \\ 0 & 1 & 0 \\ 0 & 0 & 1 \end{bmatrix} + \begin{bmatrix} 0 & -\beta_y & \beta_x \\ \beta_y & 0 & -\phi \\ -\beta_x & \phi & 0 \end{bmatrix}\right)\mathbf{R_{P/G}} \quad (2.19)$$

Or
$$\mathbf{R'_{P/G}} = \mathbf{R_{P/G}} + \begin{bmatrix} 0 & -\beta_y & \beta_x \\ \beta_y & 0 & -\phi \\ -\beta_x & \phi & 0 \end{bmatrix} \mathbf{R_{P/G}} \tag{2.20}$$

Subtracting equation (2.16) from equation (2.17) and using equation (2.20), yields:

$$\left(\mathbf{R'_P} - \mathbf{R_P}\right) = \left(\mathbf{R'_G} - \mathbf{R_G}\right) + \begin{bmatrix} 0 & -\beta_y & \beta_x \\ \beta_y & 0 & -\phi \\ -\beta_x & \phi & 0 \end{bmatrix} \mathbf{R_{P/G}} \tag{2.21}$$

Or
$$\mathbf{u_s} = \mathbf{u} + \begin{bmatrix} 0 & -\beta_y & \beta_x \\ \beta_y & 0 & -\phi \\ -\beta_x & \phi & 0 \end{bmatrix} \begin{Bmatrix} x \\ y \\ z \end{Bmatrix} \tag{2.22}$$

where $\mathbf{u_s} = \left(\mathbf{R'_P} - \mathbf{R_P}\right)$, $\mathbf{u} = \left(\mathbf{R'_G} - \mathbf{R_G}\right)$, and $\mathbf{R_{P/G}} = \begin{Bmatrix} x \\ y \\ z \end{Bmatrix}$.

Expanding equation (2.22) yields:

$$u_s = u + z\beta_x - y\beta_y,$$

$$v_s = v_{shear} + x\beta_y - z\phi$$

and
$$w_s = w_{shear} - x\beta_x + y\phi. \tag{2.23}$$

where u_s, v_s, w_s are the incremental displacement components of vector $\mathbf{r_P}$ and u, v_{shear}, w_{shear} are the incremental displacement components of the vector $\mathbf{r_G}$.

From equation (2.23), the strain field can be extracted as follows:

$$\varepsilon_{xx} = \frac{\partial u}{\partial x} + z\frac{\partial \beta_x}{\partial x} - y\frac{\partial \beta_y}{\partial x},$$

$$\gamma_{xy} = \frac{\partial v_{shear}}{\partial x} = \frac{1}{2}\left(-\beta_y + \frac{\partial v}{\partial x} - z\frac{\partial \phi}{\partial x} \right),$$

$$\gamma_{xz} = \frac{\partial w_{shear}}{\partial x} = \frac{1}{2}\left(\beta_x + \frac{\partial w}{\partial x} + y\frac{\partial \phi}{\partial x} \right),$$

and $$\varepsilon_{yy} = 0, \varepsilon_{zz} = 0, \gamma_{yz} = 0. \tag{2.24}$$

It is more convenient to express the strain field in the cylindrical coordinates using the following transformation equation:

$$\begin{Bmatrix} \varepsilon_{xx} \\ \varepsilon_{\theta\theta} \\ \varepsilon_{rr} \\ \gamma_{x\theta} \\ \gamma_{r\theta} \\ \gamma_{xr} \end{Bmatrix} = \begin{bmatrix} 1 & 0 & 0 & 0 & 0 & 0 \\ 0 & n^2 & m^2 & 0 & -2nm & 0 \\ 0 & m^2 & n^2 & 0 & 2nm & 0 \\ 0 & 0 & 0 & -n & 0 & m \\ 0 & -mn & mn & 0 & \left(m^2 - n^2\right) & 0 \\ 0 & 0 & 0 & m & 0 & n \end{bmatrix} \begin{Bmatrix} \varepsilon_{xx} \\ \varepsilon_{yy} \\ \varepsilon_{zz} \\ \gamma_{xy} \\ \gamma_{yz} \\ \gamma_{xz} \end{Bmatrix} \tag{2.25}$$

where $m = cos\,\theta$ and $n = sin\,\theta$.

Let $y = r\,cos\,\theta$ and $z = r\,sin\,\theta$, then equations (2.24) and (2.25) gives:

$$\varepsilon_{xx} = \frac{\partial u}{\partial x} + r\,sin\,\theta\frac{\partial \beta_x}{\partial x} - r\,cos\,\theta\frac{\partial \beta_y}{\partial x} \quad , \tag{2.26}$$

$$\gamma_{x\theta} = \frac{1}{2}\left(\beta_y\,sin\,\theta + \beta_x\,cos\,\theta - sin\,\theta\frac{\partial v}{\partial x} + cos\,\theta\frac{\partial w}{\partial x} + r\frac{\partial \phi}{\partial x} \right), \tag{2.27}$$

$$\gamma_{xr} = \frac{1}{2}\left(\beta_x\,sin\,\theta - \beta_y\,cos\,\theta - s\,in\,\theta\frac{\partial w}{\partial x} + cos\,\theta\frac{\partial v}{\partial x} \right), \tag{2.28}$$

and $$\varepsilon_{rr} = 0, \varepsilon_{\theta\theta} = 0, \text{ and } \gamma_{r\theta} = 0. \tag{2.29}$$

The constitutive equations of the shaft, in the cylindrical coordinate system, are given by:

$$\begin{Bmatrix}\sigma_x\\ \tau_{x\theta}\\ \tau_{rx}\end{Bmatrix}=\frac{E}{2(1+\upsilon)}\begin{bmatrix}\frac{2(1-\upsilon)}{(1-2\upsilon)} & 0 & 0\\ 0 & 1 & 0\\ 0 & 0 & 1\end{bmatrix}\begin{Bmatrix}\varepsilon_x\\ \gamma_{x\theta}\\ \gamma_{rx}\end{Bmatrix} \tag{2.30}$$

B. Stresses and Strains in the *VEM* Layer

The shear strains the *VEM* layer can be written as:

$$\gamma^v_{x\theta}=\frac{1}{h_v}\left[(u_s-u_c)+\left(r_s\beta^s_y-r_c\beta^c_y\right)\cos\theta-\left(r_s\beta^s_x-r_c\beta^c_x\right)\sin\theta\right] \tag{2.31}$$

and

$$\gamma^v_{rx}=\frac{1}{h_v}\left[r_v(\phi_s-\phi_c)+\left(r_s\beta^s_y-r_c\beta^c_y\right)\sin\theta+\left(r_s\beta^s_x-r_c\beta^c_x\right)\cos\theta\right] \tag{2.32}$$

2.3. Mass and Stiffness Matrices of the Shaft/Local Sources of Resonance Element

A. Mass Matrix

The mass matrix of the shaft/local sources of resonance element is determined by modifying the shape function matrices defined in Appendix 2A to match the parameters of the shaft and the constraining layer such that:

For the Shaft:

$$\begin{aligned}&u_s=\left[N_{u_s}\right]\{\Delta\},\ \phi_s=\left[N_{\theta_{xs}}\right]\{\Delta\},v_s=\left[N_{vs}\right]\{\Delta\},\\ &w_s=\left[N_{ws}\right]\{\Delta\},\ \beta_{xs}=\left[N_{\theta_{ys}}\right]\{\Delta\},\text{ and }\beta_{ys}=\left[N_{\theta_{zs}}\right]\{\Delta\}\end{aligned} \tag{2.33}$$

For the Constraing Layer:

$$\begin{aligned}&u_c=\left[N_{u_c}\right]\{\Delta\},\ \phi_c=\left[N_{\theta_{xc}}\right]\{\Delta\},v_c=\left[N_{vc}\right]\{\Delta\},\\ &w_c=\left[N_{wc}\right]\{\Delta\},\ \beta_{xc}=\left[N_{\theta_{yc}}\right]\{\Delta\},\text{ and }\beta_{yc}=\left[N_{\theta_{zc}}\right]\{\Delta\}\end{aligned} \tag{2.34}$$

The above shape functions are used to extract the mass matrix of the shaft/constraining layer assembly from the expression of the shaft and the constraining layer kinetic energies given by equations (2.13) and (2.14) as follows:

$$T_s = \frac{1}{2}\{\dot{\Delta}\}^T \int_0^{L_e} \Big[\rho_s A_s \left([N_{us}]^T [N_{us}] + [N_{vs}]^T [N_{vs}] + [N_{ws}]^T [N_{ws}] \right) + I_{d_s} \left(\left[N_{\theta_{xs}} \right]^T \left[N_{\theta_{xs}} \right] + \left[N_{\theta_{ys}} \right]^T \left[N_{\theta_{ys}} \right] \right) + I_{Ps} \left[N_{\theta_{xs}} \right]^T \left[N_{\theta_{xs}} \right] \Big] dx \{\dot{\Delta}\} - \{\Delta\}^T \int_0^{L_e} I_{Ps} \Omega \left[N_{\theta_{xs}} \right]^T \left[N_{\theta_{ys}} \right] dx \{\dot{\Delta}\} \tag{2.35}$$

and,

$$T_c = \frac{1}{2}\{\dot{\Delta}\}^T \int_0^{L_e} \Big[\rho_c A_c \left([N_{uc}]^T [N_{uc}] + [N_{vc}]^T [N_{vc}] + [N_{wc}]^T [N_{wc}] \right) + I_{d_c} \left(\left[N_{\theta_{xc}} \right]^T \left[N_{\theta_{xc}} \right] + \left[N_{\theta_{yc}} \right]^T \left[N_{\theta_{yc}} \right] \right) + I_{Pc} \left[N_{\theta_{xc}} \right]^T \left[N_{\theta_{xc}} \right] \Big] dx \{\dot{\Delta}\} - \{\Delta\}^T \int_0^{L_e} I_{Pc} \Omega \left[N_{\theta_{xc}} \right]^T \left[N_{\theta_{yc}} \right] dx \{\dot{\Delta}\} \tag{2.36}$$

Combining equations (2.35) and (2.36) yields:

$$T = \frac{1}{2}\{\dot{\Delta}\}^T \left[[M_s] + [M_c] \right] \{\dot{\Delta}\} + \frac{1}{2}\{\dot{\Delta}\}^T \left[[I_{\theta s}] + [I_{\theta c}] \right] \{\dot{\Delta}\} - \{\Delta\}^T \left[\left[I_{\theta xys} \right] + \left[I_{\theta xyc} \right] \right] \{\dot{\Delta}\} \tag{2.37}$$

where

$$[M_s] = \int_0^{L_e} \Big[\rho_s A_s \left([N_{us}]^T [N_{us}] + [N_{vs}]^T [N_{vs}] + [N_{ws}]^T [N_{ws}] \right) dx,$$

$$[M_c] = \int_0^{L_e} \Big[\rho_c A_c \left([N_{uc}]^T [N_{uc}] + [N_{vc}]^T [N_{vc}] + [N_{wc}]^T [N_{wc}] \right) dx,$$

$$[I_{\theta s}] = \int_0^{L_e} \Big[I_{d_s} \left(\left[N_{\theta_{xs}} \right]^T \left[N_{\theta_{xs}} \right] + \left[N_{\theta_{ys}} \right]^T \left[N_{\theta_{ys}} \right] \right) + I_{Ps} \left[N_{\theta_{xs}} \right]^T \left[N_{\theta_{xs}} \right] \Big] dx$$

$$[I_{\theta c}] = \int_0^{L_e} \Big[I_{d_c} \left(\left[N_{\theta_{xc}} \right]^T \left[N_{\theta_{xc}} \right] + \left[N_{\theta_{yc}} \right]^T \left[N_{\theta_{yc}} \right] \right) + I_{Pc} \left[N_{\theta_{xc}} \right]^T \left[N_{\theta_{xc}} \right] \Big] dx,$$

,

$$\left[I_{\theta xys}\right] = \int_0^{L_e} I_{Ps}\,\Omega\left[N_{\theta_{xs}}\right]^T\left[N_{\theta_{ys}}\right]dx,$$

and
$$\left[I_{\theta xyc}\right] = \int_0^{L_e} I_{Pc}\,\Omega\left[N_{\theta_{xc}}\right]^T\left[N_{\theta_{yc}}\right]dx. \tag{2.38}$$

B. Stiffness Matrix

The stiffness matrix of the shaft/local sources of resonance element is determined by using the following expression of the total potential energy *U:*

$$U = U_s + U_c + U_v \tag{2.39}$$

where U_s, U_c, and U_v are the potential energies of the shaft, the constraining layer, and the VEM respectively. These energies are given by:

$$U_s = \frac{1}{2}\int_V \{\sigma_{xs} \quad \tau_{x\theta s} \quad \tau_{rxs}\}\begin{Bmatrix}\varepsilon_{xs}\\ \gamma_{x\theta s}\\ \gamma_{rxs}\end{Bmatrix}dV, \tag{2.40}$$

But as,
$$\begin{Bmatrix}\sigma_{xs}\\ \tau_{x\theta s}\\ \tau_{rxs}\end{Bmatrix} = \frac{E_s}{2(1+\upsilon_s)}\begin{bmatrix}\frac{2(1-\upsilon_s)}{(1-2\upsilon_s)} & 0 & 0\\ 0 & 1 & 0\\ 0 & 0 & 1\end{bmatrix}\begin{Bmatrix}\varepsilon_{xs}\\ \gamma_{x\theta s}\\ \gamma_{rxs}\end{Bmatrix} = D_s\begin{Bmatrix}\varepsilon_{xs}\\ \gamma_{x\theta s}\\ \gamma_{rxs}\end{Bmatrix} \tag{2.41}$$

Then, equation (2.40) reduces to:

$$U_s = \frac{1}{2}D_s\int_V \{\varepsilon_{xs} \quad \gamma_{x\theta s} \quad \gamma_{rxs}\}\begin{Bmatrix}\varepsilon_{xs}\\ \gamma_{x\theta s}\\ \gamma_{rxs}\end{Bmatrix}dV \tag{2.42}$$

where $D_s = \frac{E_s}{2(1+\upsilon_s)}\begin{bmatrix}\frac{2(1-\upsilon_s)}{(1-2\upsilon_s)} & 0 & 0\\ 0 & 1 & 0\\ 0 & 0 & 1\end{bmatrix}$.

Similarly, the potential energy of the constraining layer U_c is given by:

$$U_c = \frac{1}{2} D_c \int_V \{\varepsilon_{xc} \quad \gamma_{x\theta c} \quad \gamma_{rxc}\} \begin{Bmatrix} \varepsilon_{xc} \\ \gamma_{x\theta c} \\ \gamma_{rxc} \end{Bmatrix} dV \tag{2.43}$$

where $D_c = \frac{E_c}{2(1+\upsilon_c)} \begin{bmatrix} \frac{2(1-\upsilon_c)}{(1-2\upsilon_c)} & 0 & 0 \\ 0 & 1 & 0 \\ 0 & 0 & 1 \end{bmatrix}$.

Finally, the potential energy of the *VEM* U_v is given by:

$$U_v = \frac{1}{2} G_v \int_V \{0 \quad \gamma_{x\theta v} \quad \gamma_{rxv}\} \begin{Bmatrix} 0 \\ \gamma_{x\theta v} \\ \gamma_{rxv} \end{Bmatrix} dV \tag{2.44}$$

Using the shape function matrices defined in Appendix 2A and by equations (2.33) and (2.34) as well as combining equations (2.42) through (2.44) yields:

$$U = \frac{1}{2} \{\Delta\}^T \left[[K_s] + [K_c] + [K_v] \right] \{\Delta\} \tag{2.45}$$

where $[K_s]$,$[K_c]$, and $[K_v]$ are the stiffness matrices of the shaft, the constraining layer, and the viscoelastic material.

2.4 Equations of Motion of the Shaft/Local Sources of Resonance Assembly:

Applying the Lagrangian dynamics on the expressions of kinetic and potential energies given by equations (2.37) and (2.45), yields the following equations of motion that govern the torsional, axial , and bending vibrations of the shaft/local sources of resonance assembly:

$$[M]\{\ddot{\Delta}\} + (\Omega[G] + [C])\{\dot{\Delta}\} + [K]\{\Delta\} = \{F\} \tag{2.46}$$

where $[M],[G],[C],[K]$, $\{\Delta\}$,and $\{F\}$ are the mass matrix, the gyroscopic matrix, the damping matrix, the stiffness matrix, the nodal deflection vector, and the vector of external loads respectively.

2.5. Summary

This chapter has presented the development a finite element model to predict the dynamics and characteristics of drillstrings and rotating shafts with periodic sources of local resonance. The model will be utilized as a basis for developing the transfer matrix of a unit cell of the drillstrings and rotating shafts with periodic sources of local resonance to investigate the stop and pass band characteristics of this class of rotating shafts as will be presented in chapter 4.

The predictions of the model will be validated experimentally as will be outlined in chapter 5.

APPENDIX 2A

Timoshenko Beam Theory

2A.1 Kinematics

The Timoshenko beam theory accounts for the shear deformation and rotational inertia effects of beams. This makes it suitable for describing the behavior of short beams, sandwich composite beams or beams subject to high-frequency excitation when the wavelength approaches the thickness of the beam.

A typical Timoshenko beam element is shown in Figure (2A.1). The beam element has two bounding nodes , each of which has 6 degrees of freedom (3 translation and 3 rotations).

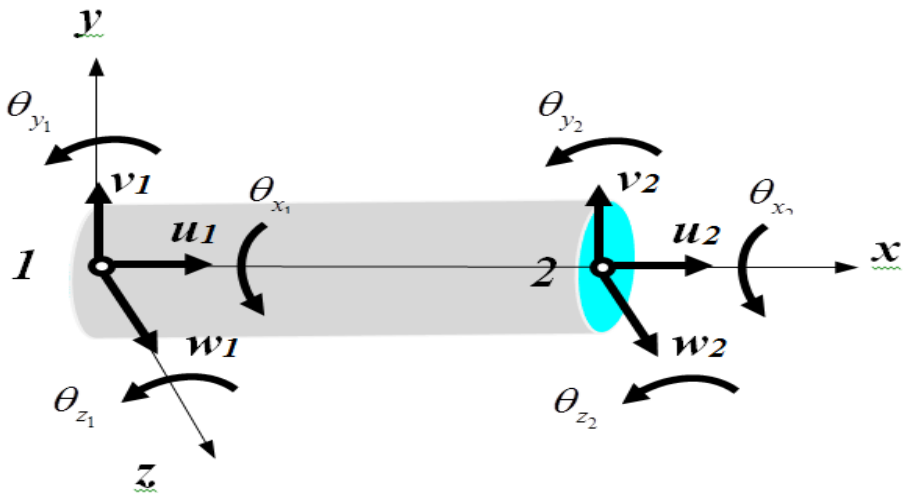

Figure (2A.1) – Timoshenko 2-node beam element

The nodal deflection vector $\{\Delta\}$ is given by:

$$\{\Delta\} = \{u_1 \quad v_1 \quad w_1 \quad \theta_{x1} \quad \theta_{y1} \quad \theta_{z1} \quad u_2 \quad v_2 \quad w_2 \quad \theta_{x2} \quad \theta_{y2} \quad \theta_{z2}\}^T \qquad (2A.1)$$

The linear ($u_i \quad v_i \quad w_i$) and angular ($\theta_{xi} \quad \theta_{yi} \quad \theta_{zi}$) deflections of the i^{th} node are displayed in Figure (2A.1).

Note that the linear deflections v and w consist of the contributions of the bending and shear components such that (Bazoune *et al*., 2003):

$$v = v_{bending} + v_{shear} \tag{2A.2}$$

Hence, $$\frac{\partial v}{\partial x} = \frac{\partial v_{bending}}{\partial x} + \frac{\partial v_{shear}}{\partial x} = \theta_z + \gamma_{xy} \tag{2A.3}$$

Integrating equation (2A.3) *wrt* x, gives:

$$v = \theta_z x + v_{shear} \tag{2A.4}$$

Similarly, $$w = w_{bending} + w_{shear} \tag{2A.6}$$

Hence, $$\frac{\partial w}{\partial x} = \frac{\partial w_{bending}}{\partial x} + \frac{\partial w_{shear}}{\partial x} = -\theta_y + \gamma_{xz} \tag{2A.7}$$

Integrating equation (2A.7) *wrt* x, gives:

$$w = -\theta_y x + w_{shear} \tag{2A.8}$$

Substituting equations (2A.4) and (2A.8) into equation (2.23), yields:

$$u_s = u + z\beta_x - y\beta_y,$$

$$v_s = v_{shear} + x\beta_y - z\phi = v - z\phi$$

and $$w_s = w_{shear} - x\beta_x + y\phi = w + y\phi. \tag{2A.9}$$

2A.2 Shape Functions

The shape function matrices $[N_i]$ describe the deflection i inside a shaft element in terms of the nodal deflection vector $\{\Delta\}$ as follows:

$$u = [N_u]\{\Delta\},\ \theta_x = \left[N_{\theta_x}\right]\{\Delta\}, v = [N_v]\{\Delta\},$$
$$w = [N_w]\{\Delta\},\ \theta_y = \left[N_{\theta_y}\right]\{\Delta\}, \text{ and } \theta_z = \left[N_{\theta_z}\right]\{\Delta\} \tag{2A.10}$$

In equation (2A.10), the shape function matrices corresponding to the axial and torsional deflections $[N_u]$ and $\left[N_{\theta_x}\right]$ are based on linear shape functions such that:

$$[N_u] = = \left[(1-\zeta)\ \ 0\ \ 0\ \ 0\ \ 0\ \ 0\ \ \zeta\ \ 0\ \ 0\ \ 0\ \ 0\ \ 0\right] \quad \text{where } \zeta = x / L_e$$

$$\text{and} \qquad \left[N_{\theta_x}\right] = \left[0\ \ 0\ \ 0\ \ (1-\zeta)\ \ 0\ \ 0\ \ 0\ \ 0\ \ 0\ \ \zeta\ \ 0\ \ 0\right] \tag{2A.11}$$

where x denotes the local coordinate along the longitudinal axis of the shaft and L_e denotes the length of the shaft element.

The remaining four shape function matrices are based on the classical cubic shape function of beams after proper modification to account for the shear correction of Timoshenko beams.

For example, for the bending deflection v, the shape function is assumed to be:

$$v = a_o + a_1 x + a_2 x^2 + a_3 x^3 \tag{2A.12}$$

Or

$$v = \left\{1\ \ x\ \ x^2\ \ x^3\right\} \begin{Bmatrix} a_0 \\ a_1 \\ a_2 \\ a_3 \end{Bmatrix} \tag{2A.13}$$

It is assumed that the shear strain is constant along the element, *i.e.*

$$\gamma_{xy} = constant = \gamma_o \tag{2A.14}$$

The bending moment M_z is related to the shear force Q_y by:

$$\frac{dM_z}{dx} = Q_y \tag{2A.15}$$

where the bending moment M_z and the shear force Q_y are given by:

$$M_z = -EI_{zz} \frac{\partial \theta_z}{\partial x}, \tag{2A.16}$$

$$\text{and} \qquad Q_y = \kappa_y GA\gamma_{xy} \tag{2A.17}$$

where EI is the flexural rigidity of the shaft, G is the shear modulus, A is the cross-sectional area, and κ_y is the shear correction factor that accounts for the non-uniform distribution of the shear

stress over the cross section of the shaft. Typical values of the shear correction factor are listed in Table 2A.1.

Table 2A.1 - Shear Correction Factor

Shaft Section	Solid Rectangular	Solid Circular
Shear correction factor - κ	$\kappa = \frac{10(1+\nu)}{12+11\nu}$	$\kappa = \frac{6(1+\nu)}{7+6\nu}$

ν =Poisson's ratio

Now, as equation (2A.3) indicates that: $\theta_z = \frac{\partial v}{\partial x} - \gamma_o$, then:

$$\theta_z = a_1 + 2a_2 x + 3a_3 x^2 - \gamma_o \tag{2A.18}$$

Hence, combining equations (2A.16) and (2A.17) gives:

$$M_z = -EI_{zz}\left(2a_2 + 6a_3 x\right) \tag{2A.19}$$

Substituting equation (2A.19) into equation (2A.17) gives:

$$\gamma_o = -6\Lambda_z a_3 \tag{2A.20}$$

where $\Lambda_z = \frac{EI_{zz}}{\kappa_y GA}$.

Accordingly, equation (2A.18) reduces to:

$$\theta_z = a_1 + 2a_2 x + \left(3x^2 + 6\Lambda_z\right)a_3 \tag{2A.21}$$

Therefore the constants a_0 through a_3 can be determined from the components of the nodal deflection vector as follows:

$$\begin{Bmatrix} v_1 \\ \theta_{z_1} \\ v_2 \\ \theta_{z_2} \end{Bmatrix} = \begin{bmatrix} 1 & 0 & 0 & 0 \\ 0 & 1 & 0 & 6\Lambda_z \\ 1 & L_e & L_e^2 & L_e^3 \\ 0 & 1 & 2L_e & \left(3L_e^2 + 6\Lambda_z\right) \end{bmatrix} \begin{Bmatrix} a_0 \\ a_1 \\ a_2 \\ a_3 \end{Bmatrix} \tag{2A.22}$$

The constants a_0 through a_3 are then substituted in equation (2A.12) to give:

$$\left[N_v\right]=\left[0\ \ N_{v1}\ \ 0\ \ 0\ \ 0\ \ N_{v2}\ \ 0\ \ N_{v3}\ \ 0\ \ 0\ \ 0\ \ N_{v4}\right] \tag{2A.23}$$

and $$\left[N_{\theta_z}\right]=\left[0\ \ N_{\theta z1}\ \ 0\ \ 0\ \ 0\ \ N_{\theta z2}\ \ 0\ \ N_{\theta z3}\ \ 0\ \ 0\ \ 0\ \ N_{\theta z4}\right] \tag{2A.24}$$

where $$N_{v1}=\bar{\Phi}_z\left(1-3\zeta^2+2\zeta^3+\Phi_z\left[1-\zeta\right]\right) \tag{2A.25}$$

$$N_{v2}=L_e\bar{\Phi}_z\left(\zeta-2\zeta^2+\zeta^3+\frac{1}{2}\Phi_z\zeta\left[1-\zeta\right]\right) \tag{2A.26}$$

$$N_{v3}=\bar{\Phi}_z\left(3\zeta^2-2\zeta^3+\Phi_z\zeta\right) \tag{2A.27}$$

$$N_{v4}=L_e\bar{\Phi}_z\left(-\zeta^2+\zeta^3-\frac{1}{2}\Phi_z\zeta\left[1-\zeta\right]\right) \tag{2A.28}$$

$$N_{\theta z1}=\frac{6}{L_e}\bar{\Phi}_z\left(-\zeta+\zeta^3\right) \tag{2A.29}$$

$$N_{\theta z2}=\bar{\Phi}_z\left(1-4\zeta+3\zeta^2+\zeta^3+\Phi_z\left[1-\zeta\right]\right) \tag{2A.30}$$

$$N_{\theta z3}=-\frac{6}{L_e}\bar{\Phi}_z\left(-\zeta+\zeta^2\right) \tag{2A.31}$$

$$N_{\theta z4}=\bar{\Phi}_z\left(-2\zeta+3\zeta^2+\Phi_z\zeta\right) \tag{2A.32}$$

where $$\bar{\Phi}_z=\frac{1}{1+\Phi_z}\quad\text{and}\quad\Phi_z=\frac{12EI_{zz}}{\kappa_y GAL_e^2} \tag{2A.33}$$

In a similar manner, it can be easily shown the shape function matrices for *w* and θ_y are give by

$$\left[N_w\right]=\left[0\ \ 0\ \ N_{w1}\ \ 0\ \ N_{w2}\ \ 0\ \ 0\ \ 0\ \ N_{w3}\ \ 0\ \ N_{w4}\ \ 0\right] \tag{2A.34}$$

and $$\left[N_{\theta_y}\right]=\left[0\ \ 0\ \ N_{\theta y1}\ \ 0\ \ N_{\theta y2}\ \ 0\ \ 0\ \ 0\ \ N_{\theta y3}\ \ 0\ \ N_{\theta y4}\ \ 0\right] \tag{2A.35}$$

where $$N_{w1}=\bar{\Phi}_y\left(1-3\zeta^2+2\zeta^3+\Phi_y\left[1-\zeta\right]\right) \tag{2A.36}$$

$$N_{w2} = L_e \bar{\Phi}_y \left(\zeta - 2\zeta^2 + \zeta^3 + \frac{1}{2}\Phi_y \zeta \left[1 - \zeta \right] \right) \tag{2A.37}$$

$$N_{w3} = \bar{\Phi}_y \left(3\zeta^2 - 2\zeta^3 + \Phi_y \zeta \right) \tag{2A.38}$$

$$N_{w4} = L_e \bar{\Phi}_y \left(-\zeta^2 + \zeta^3 - \frac{1}{2}\Phi_y \zeta \left[1 - \zeta \right] \right) \tag{2A.39}$$

$$N_{\theta y1} = \frac{6}{L_e} \bar{\Phi}_y \left(-\zeta + \zeta^3 \right) \tag{2A.40}$$

$$N_{\theta y2} = \bar{\Phi}_y \left(1 - 4\zeta + 3\zeta^2 + \zeta^3 + \Phi_y \left[1 - \zeta \right] \right) \tag{2A.41}$$

$$N_{\theta y3} = -\frac{6}{L_e} \bar{\Phi}_y \left(-\zeta + \zeta^2 \right) \tag{2A.42}$$

$$N_{\theta y4} = \bar{\Phi}_y \left(-2\zeta + 3\zeta^2 + \Phi_y \zeta \right) \tag{2A.43}$$

where $\bar{\Phi}_y = \dfrac{1}{1 + \Phi_y}$ and $\Phi_y = \dfrac{12 E I_{yy}}{\kappa_z G A L_e^2}$ (2A.44)

Chapter 3: Modeling of a Drillstrings with Periodic Local Sources of Resonance Using ANSYS

3.1. Overview:

This chapter presents the potential application of the concept of rotating shaft with periodic local sources of resonance to oil well drillstrings. Such an effort aims at demonstrating the effectiveness of the proposed concept in simultaneously controlling the axial, bending, and torsional modes of vibration of practical drillstrings particularly at low excitation frequencies. Such effectiveness stems from the ability of the periodic local sources of resonance in shifting the zones of the stop bands to low frequencies which are compatible to the frequencies experienced by practical drillstrings.

It is important to note that with such low frequency filtering capabilities of the periodic local sources of resonance, the proposed concept constitutes a major contribution to the area of mitigating the vibration of drillstrings.

In this chapter comparisons will be established between the filtering characteristics of the periodic local sources of resonance and conventional passive inserts in order to demonstrate the merits and practicality of the proposed concepts.

The effect of the design parameters of the inserts and the local sources of resonance on the location and bandwidth of the stop band zones will be investigated in great details. In this regard, the practical configuration of the drillstring studied extensively by Khulief and co-workers (2005, 2007, 2008, and 2009) is considered as the basis for comparison between conventional uniform drillstrings and drillstrings provided with passive inserts and inserts with built-in sources of local resonance.

3.2. Finite element model for Drillstring

3.2.1 Parameters of Considered Drillstring

The drillstring model considered by Khulief and co-workers (2005, 2007, 2008, and 2009) has the characteristics listed in Table 3.1.

Table 3.2 lists the main physical and geometrical parameters of the periodic inserts and Table 3.3 displays the corresponding values of the parameters of the inserts with the sources of local resonance.

In Table 3.4, the properties of the considered *VEM* intermediate layer are included.

Table 3.1 – Main physical and geometrical parameters of the drillstring under consideration (Khulief and co-workers (2005, 2007, 2008, and 2009)

SPECIFICATIONS	VALUE
Drill Pipe	
Length (L_p)	1000 *m*
Outer Diameter (D_o)	0.127*m*
Inner Diameter (D_i)	0.095 *m*
Materials	
Density (ρ)	7850 kg/m^3
Modulus of Elasticity (E)	210 *GPa*
Shear Modulus (G)	77.9 *GPa*

Table 3.2 - **Main physical and geometrical parameters of the considered periodic inserts**

SPECIFICATIONS	VALUE
Periodic Inserts	
Width (W)	0.25 *m*
Outer Diameter$_i$ (D_{oi})	0.2286*m*
Inner Diameter$_i$ (D_{ii})	0.127 *m*
Materials	
Density (ρ)	7800 kg/m^3
Modulus of Elasticity (E)	210 *GPa*
Poisson's ratio (ν)	0.365
Loss factor (η)	2E-5

Table 3.3 - Main geometrical parameters of the considered periodic inserts with sources of local resonance (3 layers: inner steel ring, *VEM*, Outer steel ring)

SPECIFICATIONS	VALUE
Inner Layer	
Width (W)	0.2500 *m*
Outer Diameter$_i$ (D_{oi})	0.1524 *m*
Inner Diameter$_i$ (D_{ii})	0.1270 *m*
Intermediate Layer	
Outer Diameter$_i$ (D_{oi})	0.1905 m
Inner Diameter$_i$ (D_{ii})	0.1524 m
Outer Layer	
Outer Diameter$_i$ (D_{oi})	0.2286 m
Inner Diameter$_i$ (D_{ii})	0.1905 m

Table 3.4 - Main physical parameters of the considered VEM Intermediate layer of the periodic inserts

SPECIFICATIONS	VALUE
Case # 1	
Constant Storage Modulus (E')	15E3, 5E4, 10E4, 15E4 N/m^2
Loss Factor (η)	0.10
Poisson's ratio (ν)	0.49
Density (ρ)	1,100 kg/m^3
Case#2	
Variable Storage Modulus (E')	15E4-75E4, 15E3-75E3 N/m^2
Loss Factor (η)	0.1
Poisson's ratio (ν)	0.49
Density (ρ)	1,100 kg/m^3

3.2.2 Details of the Finite Element Model

The finite element model, developed using ANSYS for the drillstring was composed of two types of elements. The first element type was beam elements BEAM188 (3D, 2-Node element) with six degrees of freedom per node (u_x, u_y, u_z, θ_x θ_y θ_z). This type of elements is one of *ANSYS* new-technology elements, in which arbitrary cross sections can be assigned. The beam elements were used to model the drill-pipe and the drill-collar. In the current case, the cross section used for both the drill-pipe and drill-colar were of an annulus with internal/external diameters of 0.095 m and 0.127 m respectively. For the drill-collar, the diameters were 0.095 m and 0.235 m respectively. The drill-pipe length was 1000 m divided into 1440 elements, while the drillcolar length was 200 m and was divided into 288 elements. The second type of elements used in the finite element model was for the periodic collars. These were modeled using shell elements SHELL281 (8-Node Structural Shell Elements) with six degrees of freedom per node (u_x, u_y, u_z, θ_x θ_y θ_z). The shell thickness used was 0.25m, which represents the periodic collar thickness. The collars were mounted in different periodic arrangements (60, 120 and 180 equi-spaced collars). Constraining functions were enforced in the finite element model to constrain the degrees of freedom of the inner collar radii nodes to the matching degrees of freedom of the beam nodes at that location. The rotation and translation of the entire drillstring were constrained at the two ends.

A pre-stressed sequential static-modal-harmonic analysis procedure was developed. During the first simulation phase (static analysis), the effect of gravitational force was included and the stress and strain matrices were retained for further modal-harmonic analysis. A Full Modal analysis was carried out to calculate the mode shapes and the natural frequencies extending to the harmonic excitation range of interest. Once complete a Mode-Superposition Harmonic analysis was carried out utilizing the mode shapes and element stress and strain results to calculate the dynamic response of the entire drillstring subject to axial, bending forces and torsional moment near the lower end. This particular modeling procedure was adopted to be able to capture accurately the dynamic response of the drillstring without skipping any modes, if a stepped-sine harmonic analysis was directly implemented.

Figures (3.1a) and (3.1b) display the finite element models of shafts with conventional periodic inserts and inserts with built-in sources of local resonance.

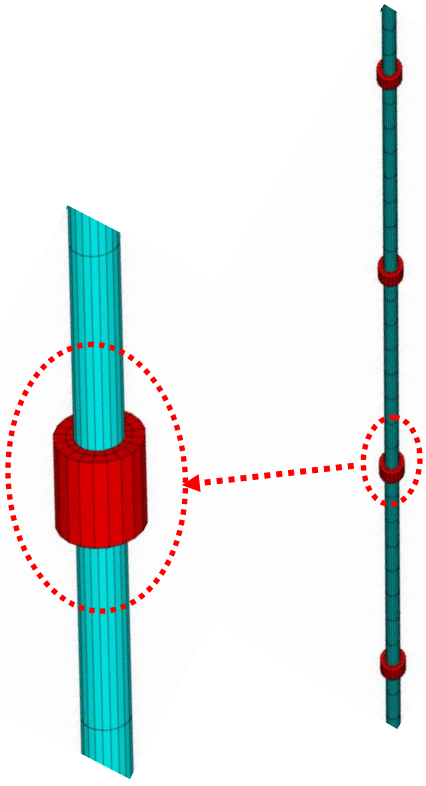

(a) – conventional periodic inserts

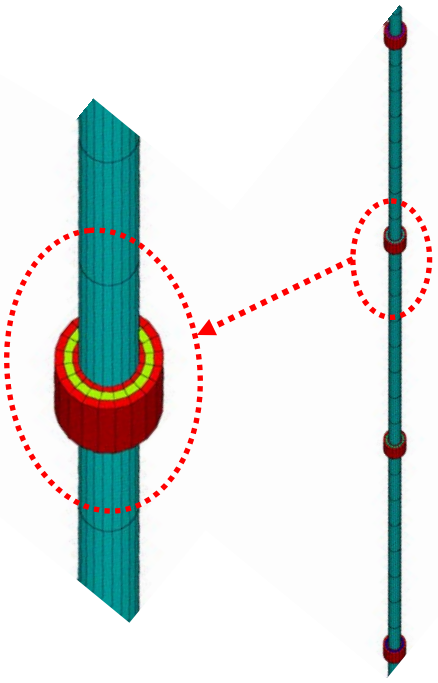

(b) – Inserts with sources of local resonance

Figure (3.1) – Finite element models of shafts with conventional periodic inserts and inserts with built-in sources of local resonance

3.2.3 Dynamic Characteristics of Uniform Shaft and Shafts with Conventional Periodic Inserts

Figure (3.2) displays a comparison between the frequency response characteristics of a conventional drillstring and a drillstring with 60 passive periodic inserts. The figure shows the simultaneous performance characteristics of the drillstrings in the torsional, axial and transverse directions.

It can be seen that the passive periodic inserts are effective in generating stop bands only in the transverse directions. These stop bands extend to frequencies as low as 5 Hz. However, the inserts are totally ineffective in mitigating the vibration in both the axial and torsional directions.

Figure (3.3) displays the corresponding comparisons between the frequency response characteristics of a conventional drillstring and a drillstring with 120 passive periodic inserts. Also, Figure (3.4) show the comparisons when the drillstring is provided with 180 passive periodic inserts.

Figures (3.3) and (3.4) suggest that increasing the number of the passive periodic inserts results in defining clearly the zones of the stop bands and in increasing the spectral width of these stop bands.

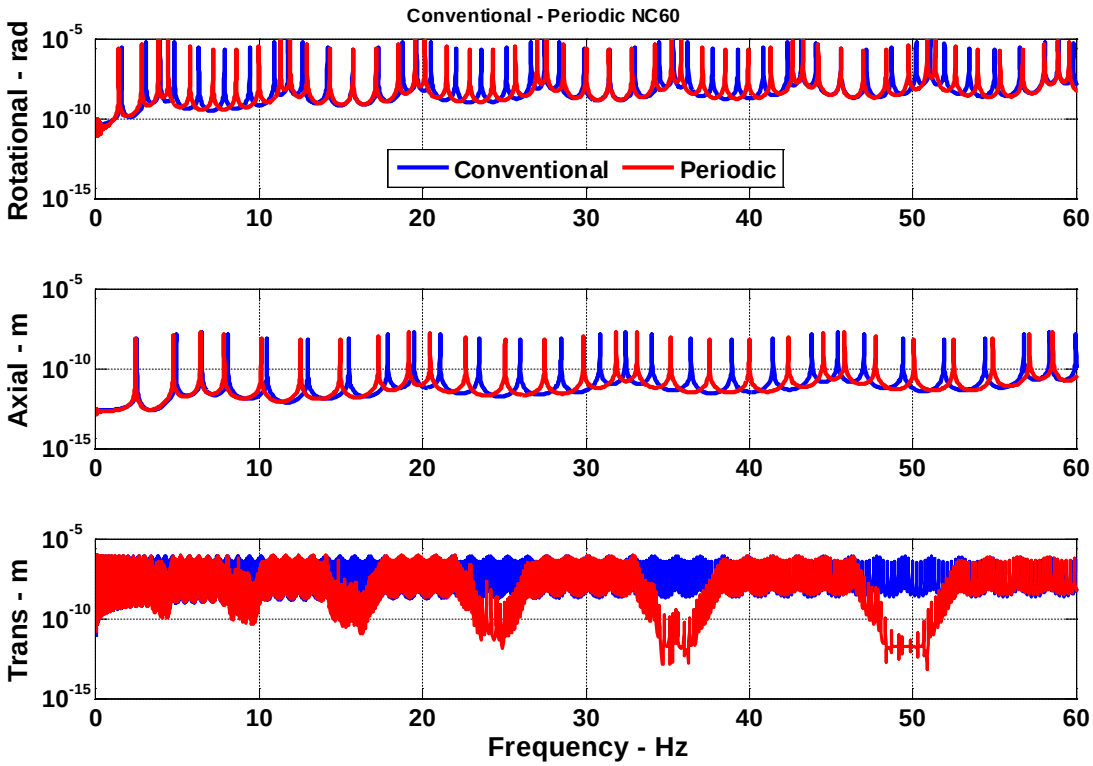

Figure (3.2) - Comparisons between the frequency response characteristics of a conventional drillstring and a drillstring with 60 passive periodic inserts

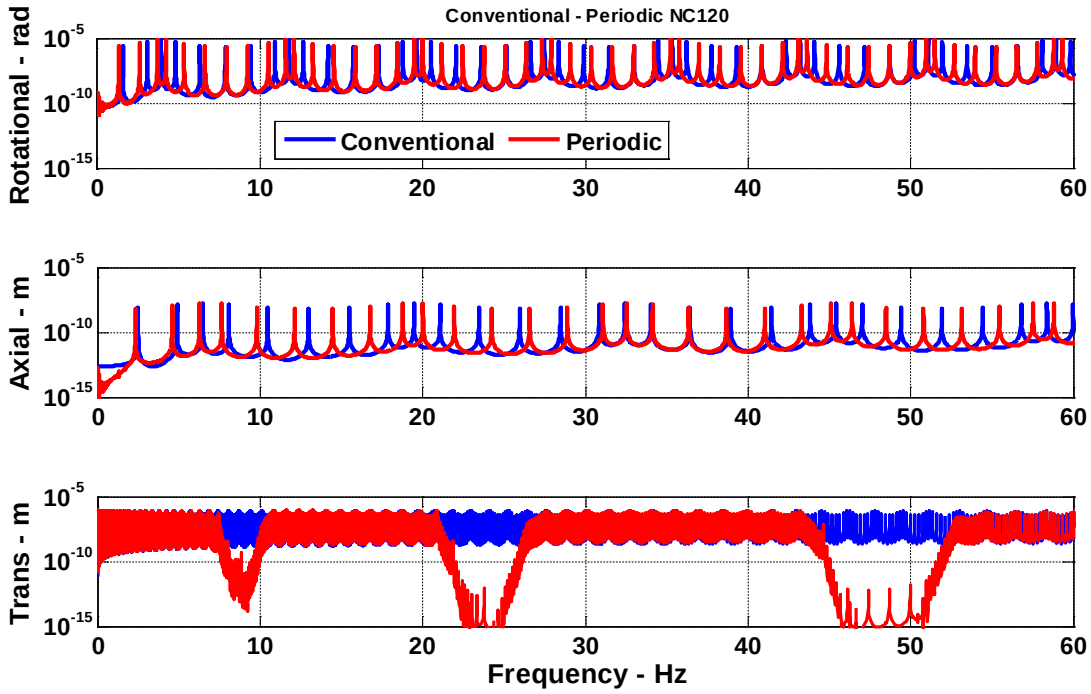

Figure (3.3) - Comparisons between the frequency response characteristics of a conventional drillstring and a drillstring with 120 passive periodic inserts

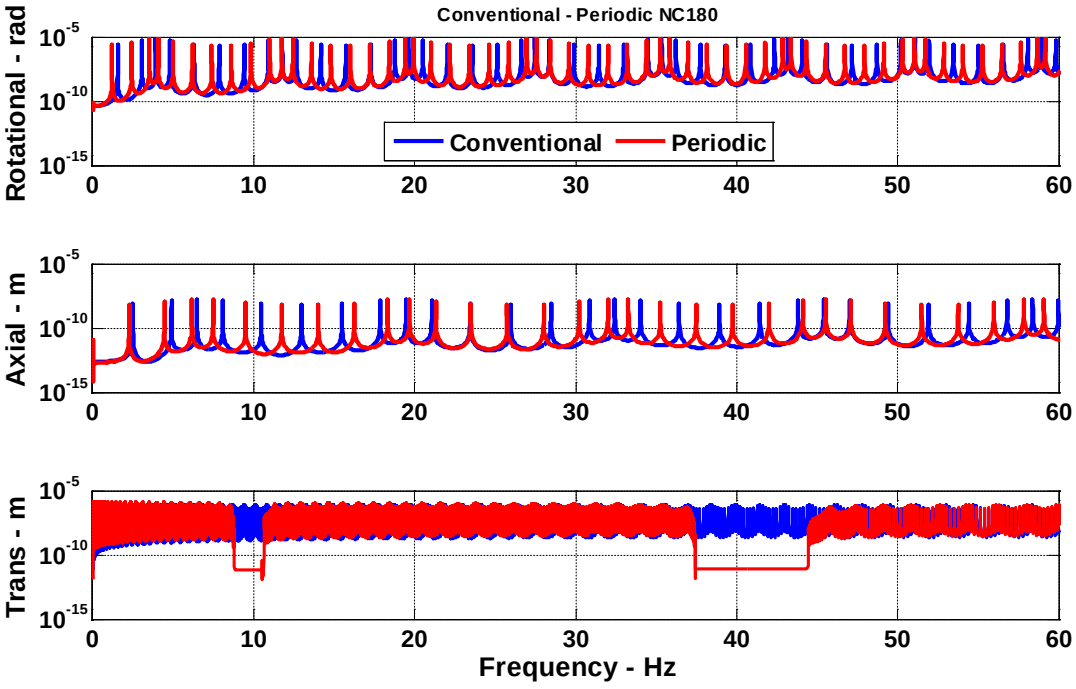

Figure (3.4) - Comparisons between the frequency response characteristics of a conventional drillstring and a drillstring with 180 passive periodic inserts

3.2.4 Dynamic Characteristics of Uniform Shaft and Shafts with Periodic Local Sources of Resonance

Figure (3.5) displays a comparison between the frequency response characteristics of a conventional drillstring and a drillstring that has 120 periodic inserts with sources of local resonance (*LR*). The figure shows the performance characteristics of the drillstrings in the torsional vibrations for different values of frequency independent (*i.e.* constant) storage modulus of the *VEM* of the inserts.

It can be seen that the periodic inserts with *LR* resonance are now effective in generating stop bands in the torsional direction. These stop bands extend to frequencies as low as 5 Hz when the storage modulus of the *VEM* is as low as 15 *KPa*. However, the stop band location and spectral width increase as the storage modulus of the *VEM* increases.

Figure (3.6) displays the corresponding comparisons between the axial frequency response characteristics of a conventional drillstring and a drillstring with 120 periodic inserts with LR sources. Also, Figure (3.7) show the comparisons when the drillstring is vibrating in the transverse direction.

Figures (3.5) through (3.7) demonstrate the effectiveness of the periodic inserts with LR in simultaneously mitigating the vibration in the torsional, axial, and transverse directions.

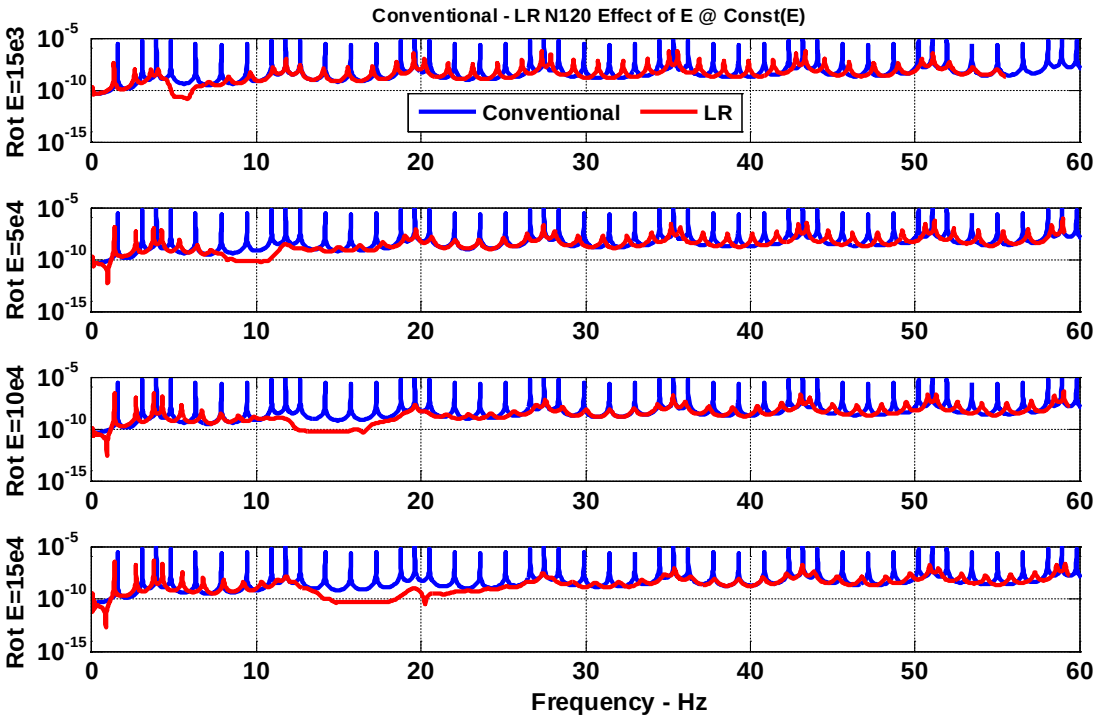

Figure (3.5) - Comparisons between the torsional frequency response characteristics of a conventional drillstring and a drillstring with 120 periodic *LR* inserts for *VEM* with constant storage moduli.

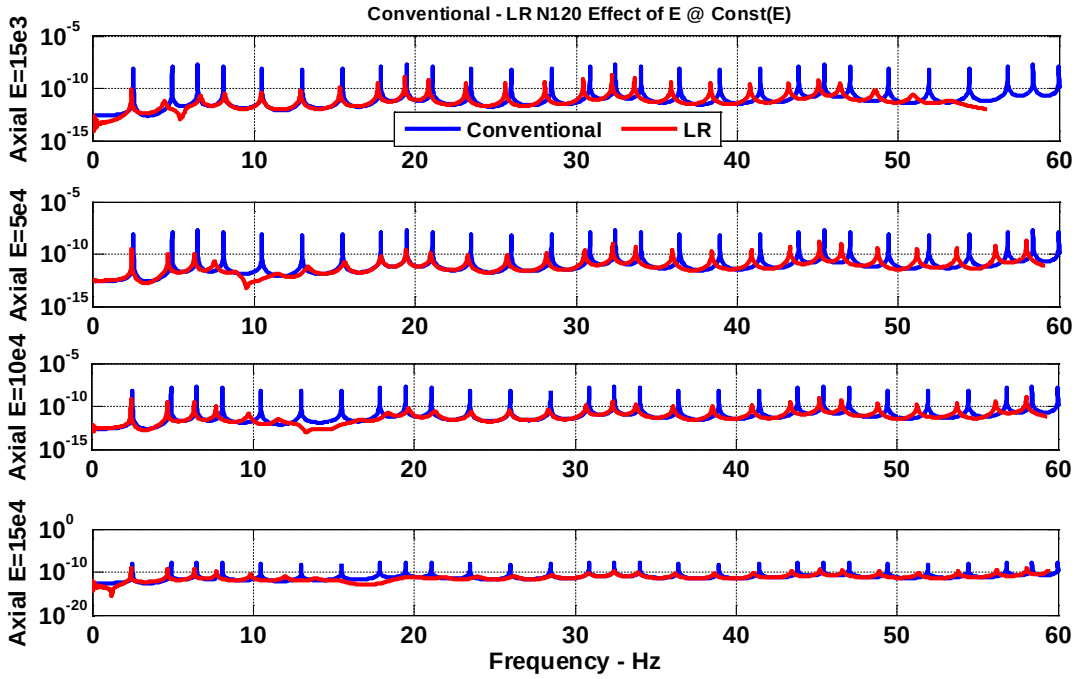

Figure (3.6) - Comparisons between the axial frequency response characteristics of a conventional drillstring and a drillstring with 120 periodic *LR* inserts for *VEM* with constant storage moduli.

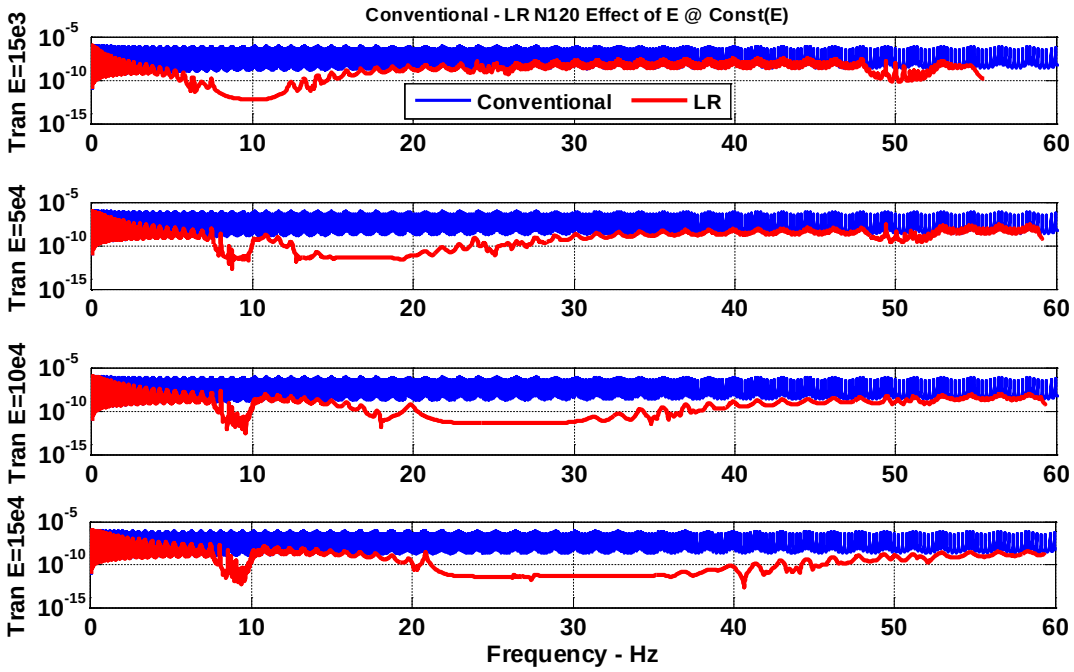

Figure (3.7) - Comparisons between the transverse frequency response characteristics of a conventional drillstring and a drillstring with 120 periodic *LR* inserts for *VEM* with constant storage moduli.

Figures (3.8) through (3.10) display comparisons between the frequency response characteristics of a conventional drillstring and a drillstring that has 120 periodic inserts with sources of local resonance (*LR*) for different values of frequency-dependent (*i.e.* variable) storage modulus of the *VEM* of the inserts. In Figure (3.8), the comparisons are established for the torsional vibrations whereas in Figure (3.9), the comparisons are presented for the axial vibrations. Figure (3.10) displays the comparisons for the transverse vibrations.

It can be seen that the periodic inserts with *LR* resonance become more effective in mitigating the vibration in all directions when the inserts are provided with frequency-dependent moduli of the *VEM* as compared to *VEM* with constant storage moduli. The developed stop bands are observed to extend over wider frequency bandwidths for all the three directions of vibration. Also, it is further observed that the stop band locations and spectral widths increase as the storage modulus of the *VEM* is increased as reported for the case of *VEM* with constant storage moduli.

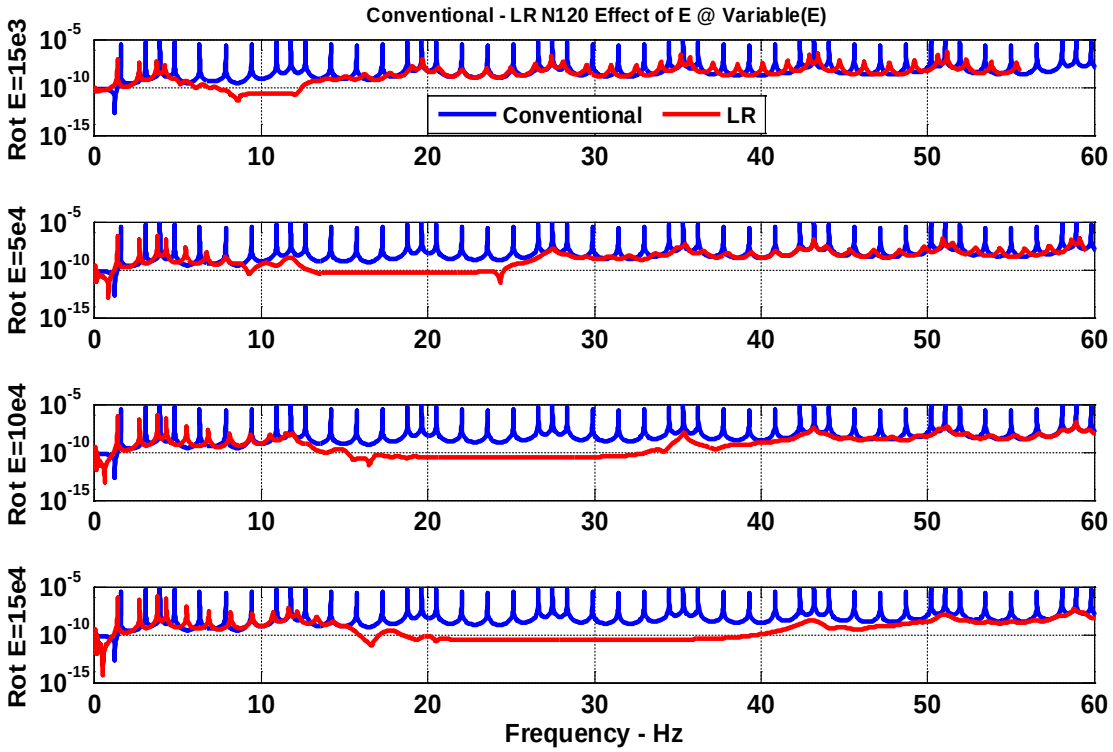

Figure (3.8) - Comparisons between the torsional frequency response characteristics of a conventional drillstring and a drillstring with 120 periodic *LR* inserts for *VEM* with variable storage moduli.

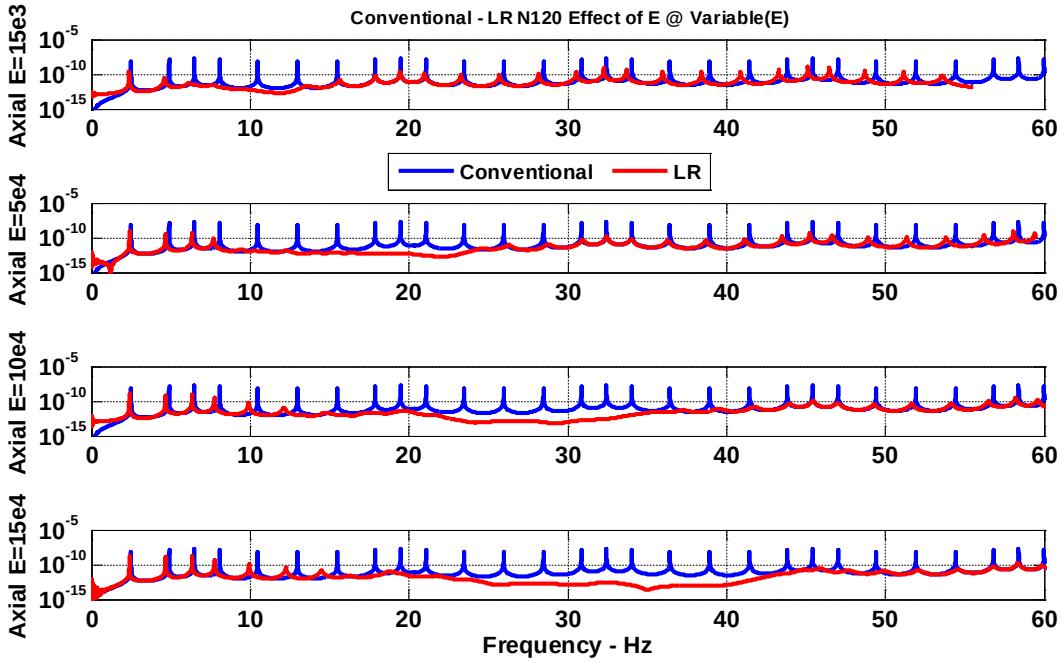

Figure (3.9) - Comparisons between the axial frequency response characteristics of a conventional drillstring and a drillstring with 120 periodic *LR* inserts for *VEM* with variable storage moduli

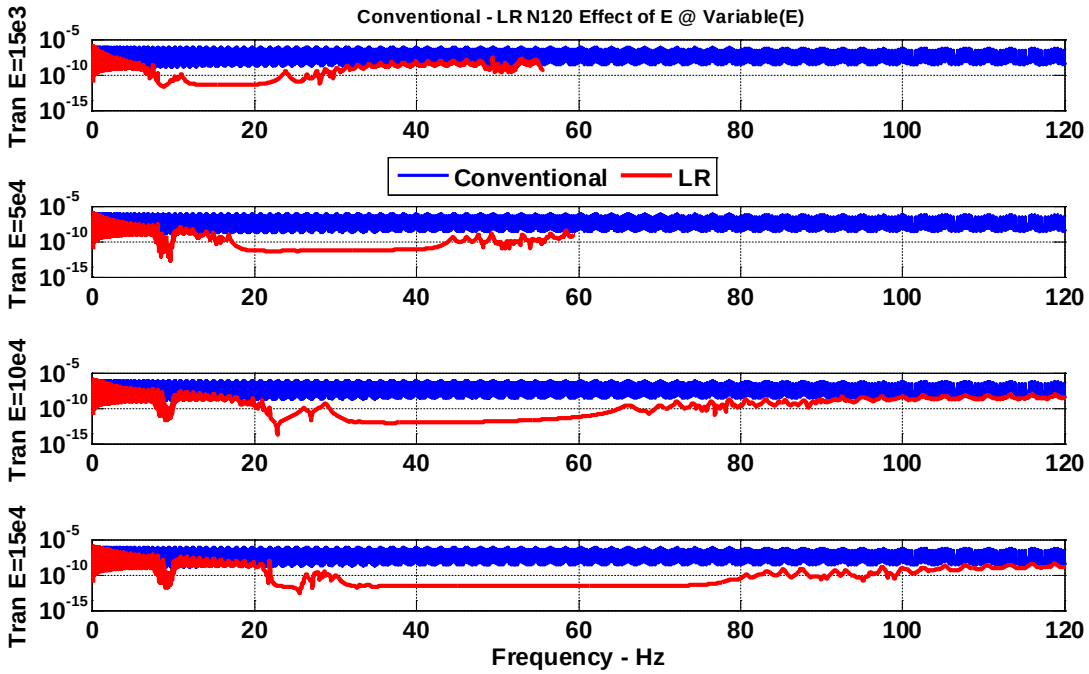

Figure (3.10) - Comparisons between the transverse frequency response characteristics of a conventional drillstring and a drillstring with 120 periodic *LR* inserts for *VEM* with variable storage moduli

Figures (3.11) through (3.13) display comparisons between the frequency response characteristics of a conventional drillstring and a drillstring that has different number of periodic inserts with sources of local resonance (*LR*) for a particular frequency independent (*i.e*. constant) storage modulus of the *VEM* of the inserts equal to 150 *KPa*. In Figure (3.11), the comparisons are established for the torsional vibrations whereas in Figure (3.12), the comparisons are presented for the axial vibrations. Figure (3.13) displays the comparisons for the transverse vibrations.

It can be seen that the periodic inserts with *LR* resonance become more effective in mitigating the vibration in all directions as the number of inserts is increased. However, small number of inserts tends to produce stop bands at low frequencies whereas large number of inserts results in higher frequency stop bands.

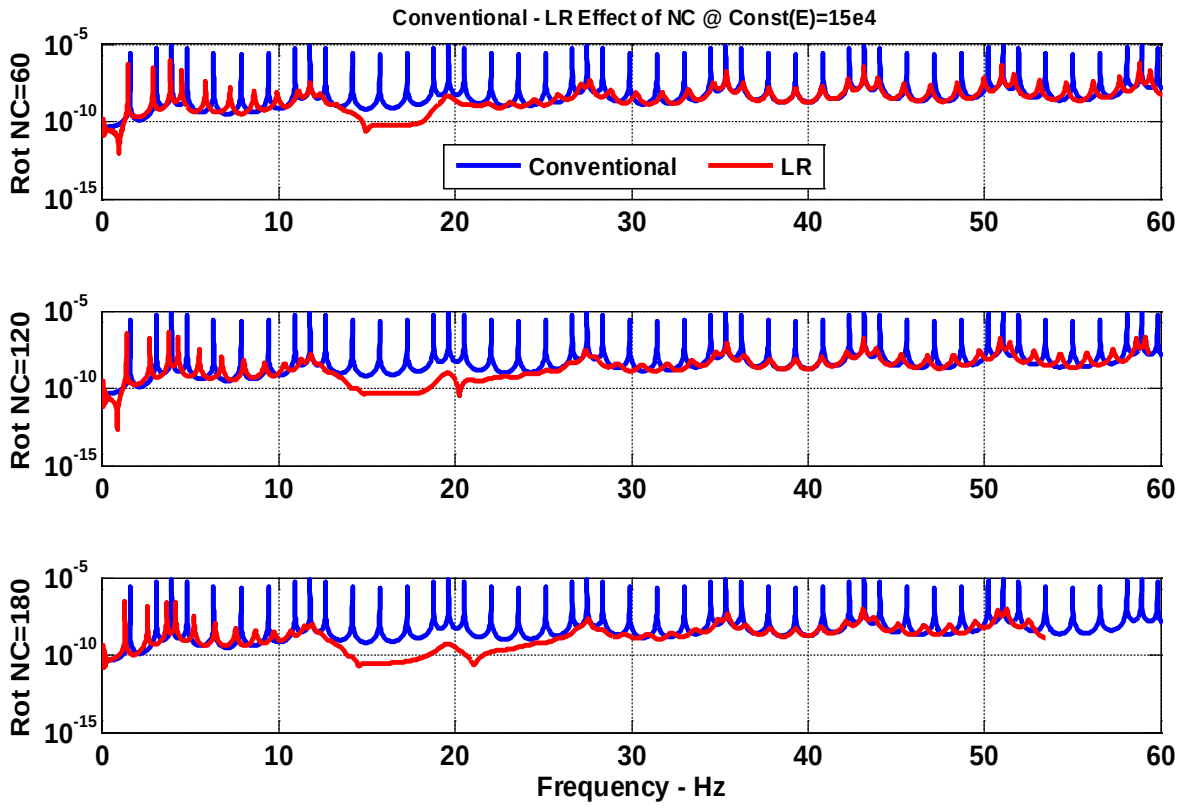

Figure (3.11) - Comparisons between the torsional frequency response characteristics of a conventional drillstring and a drillstring with periodic *LR* inserts for different number of inserts when the *VEM* has constant storage modulus

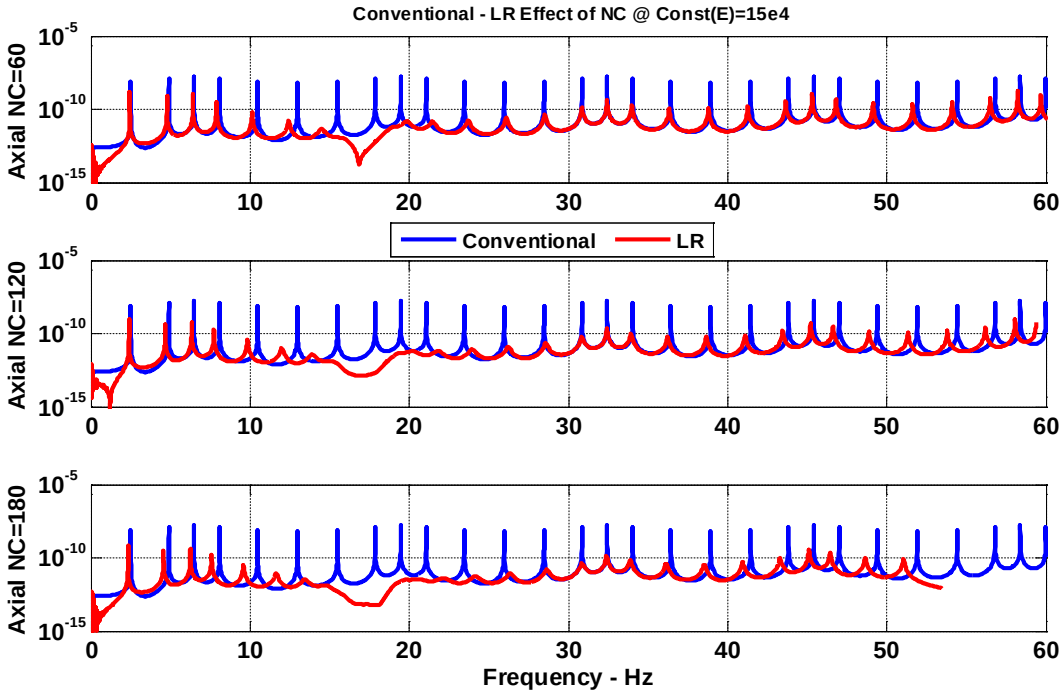

Figure (3.12) - Comparisons between the axial frequency response characteristics of a conventional drillstring and a drillstring with periodic *LR* inserts for different number of inserts when the *VEM* has constant storage modulus

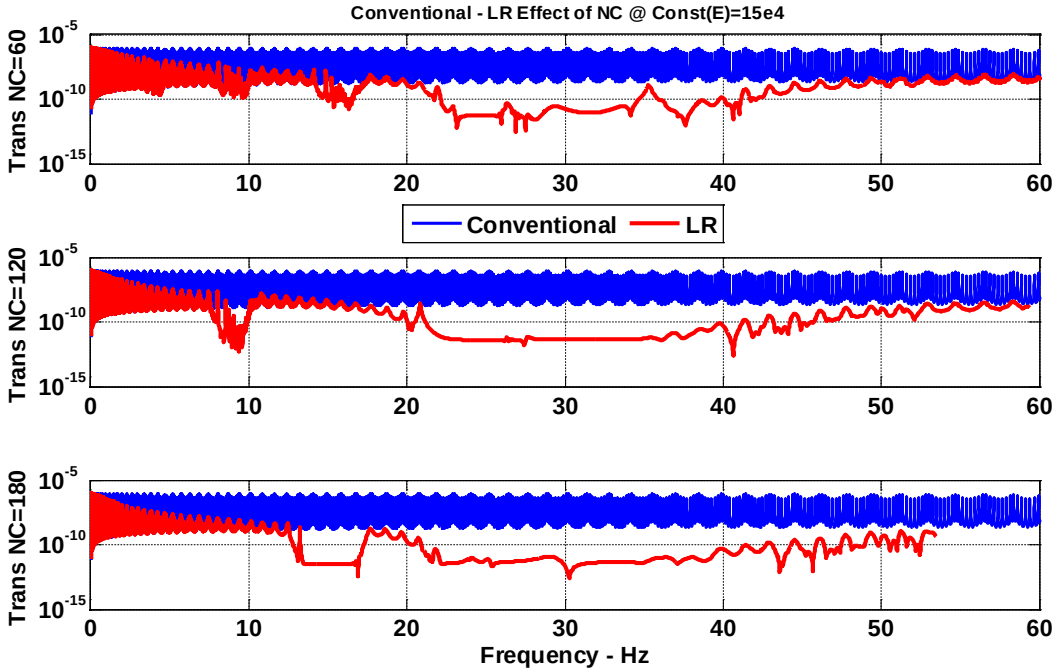

Figure (3.13) - Comparisons between the transverse frequency response characteristics of a conventional drillstring and a drillstring with periodic *LR* inserts for different number of inserts when the *VEM* has constant storage modulus

Figures (3.14) through (3.16) display comparisons between the frequency response characteristics of a conventional drillstring and a drillstring that has different number of periodic inserts with sources of local resonance (*LR*) for a particular frequency dependent (*i.e*. variable) storage modulus of the *VEM* of the inserts. In Figure (3.14), the comparisons are established for the torsional vibrations whereas in Figure (3.15), the comparisons are presented for the axial vibrations. Figure (3.16) displays the comparisons for the transverse vibrations.

It can be seen that the periodic inserts with *LR* resonance become more effective in mitigating the vibration in all directions as the number of inserts is increased. However, small number of inserts tends to produce stop bands at low frequencies whereas large number of inserts results in higher frequency stop bands.

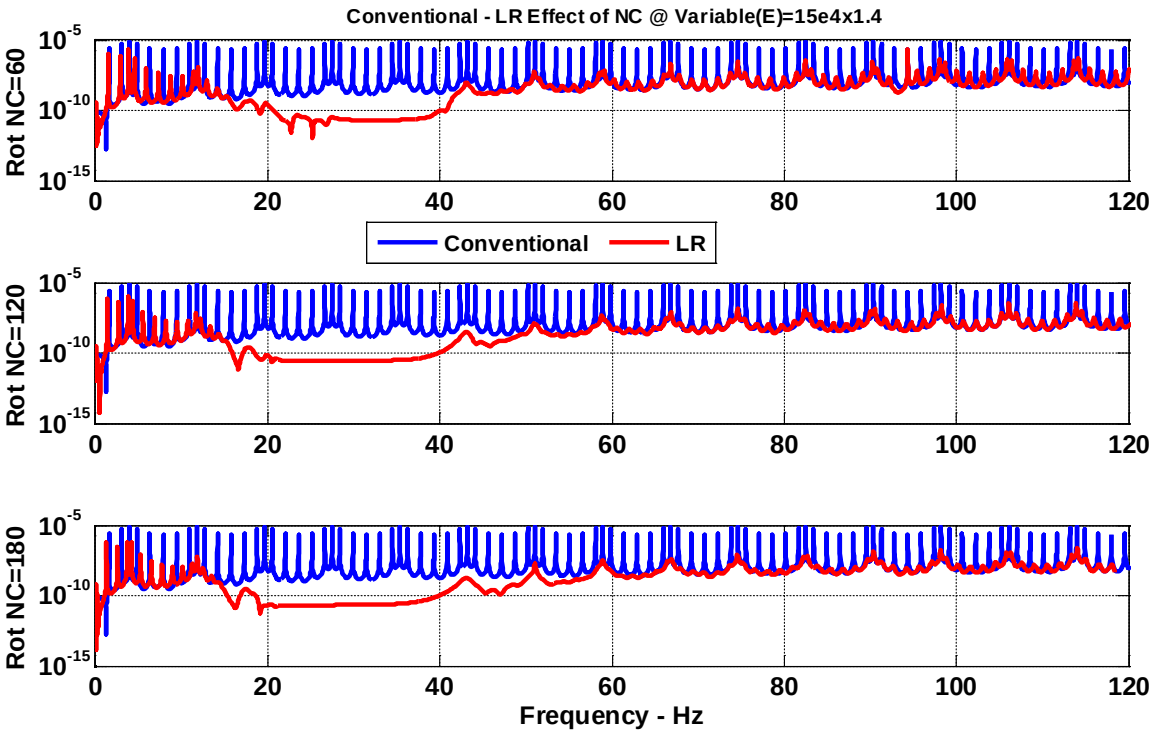

Figure (3.14) - Comparisons between the torsional frequency response characteristics of a conventional drillstring and a drillstring with periodic *LR* inserts for different number of inserts when the *VEM* has variable storage modulus

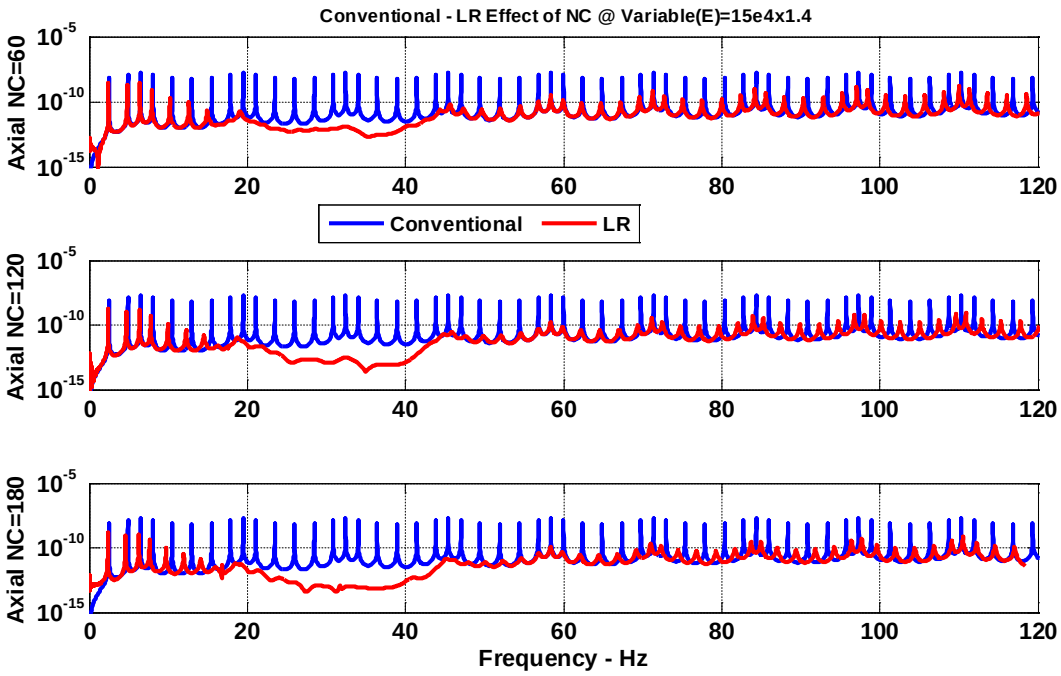

Figure (3.15) - Comparisons between the axial frequency response characteristics of a conventional drillstring and a drillstring with periodic *LR* inserts for different number of inserts when the *VEM* has variable storage modulus

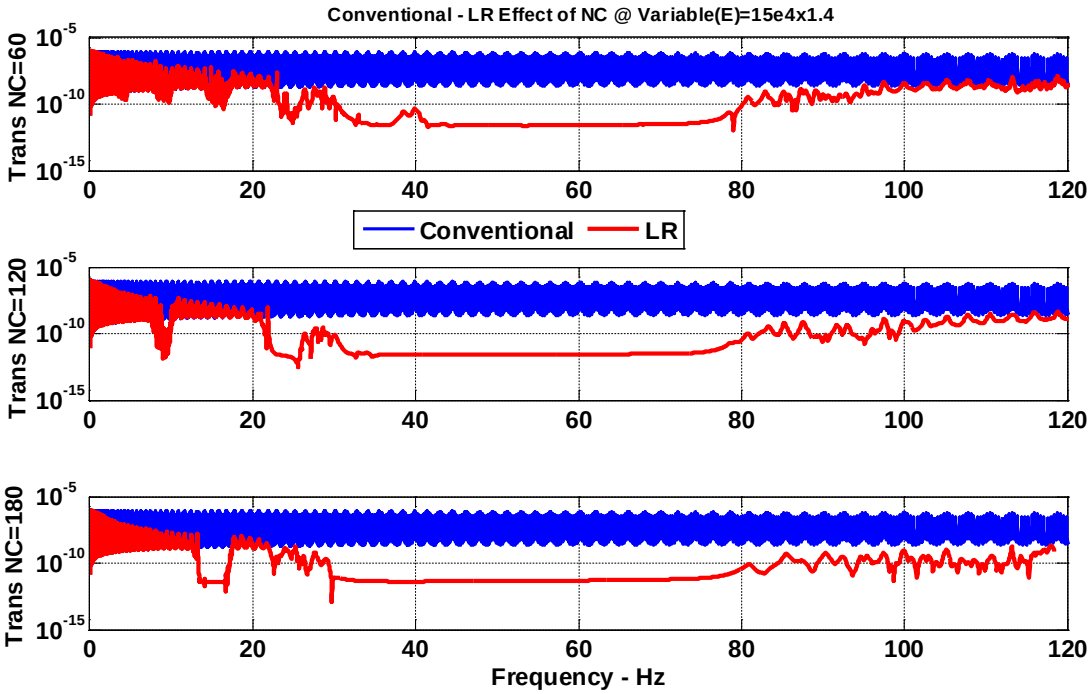

Figure (3.16) - Comparisons between the transverse frequency response characteristics of a conventional drillstring and a drillstring with periodic *LR* inserts for different number of inserts when the *VEM* has variable storage modulus

3.3. Modal Characteristics of Drillstrings and Inserts with Local Resonance

Figure (3.17) displays a sample of the orbits of the drillstring with uniform shaft for the first three modes of vibrations which are: 0.0325 *Hz*, 0.0675 *Hz*, and 0.111 *Hz* respectively.

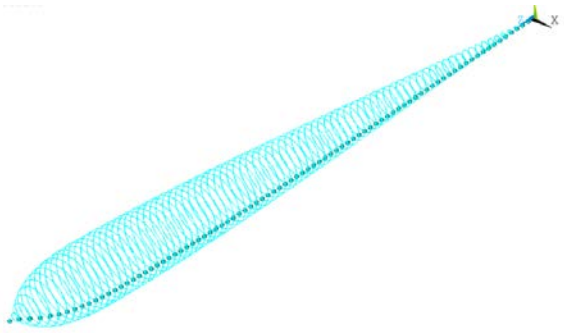

(a) – f = 0.0325 *Hz*

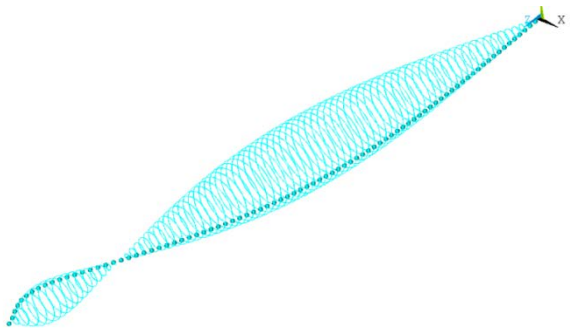

(b) – f = 0.0675 *Hz*

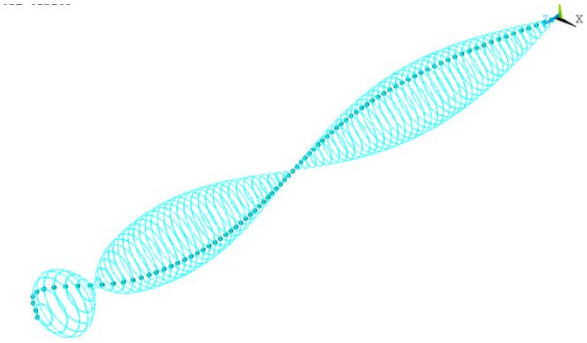

(c) f = 0.111 *Hz*

Figure (3.17) - Orbits of the drillstring at the first three modes

Figure (3.18) displays a sample of the different mode shapes of the inserts with LR . Note that these modes are much higher than those of the uniform shaft. This indicates that the local resonance of the inserts become effective in mitigating the vibration of the drillstring when the modes of the inserts coincide with those of the shaft. Under these conditions, the inserts act as local vibration absorbers.

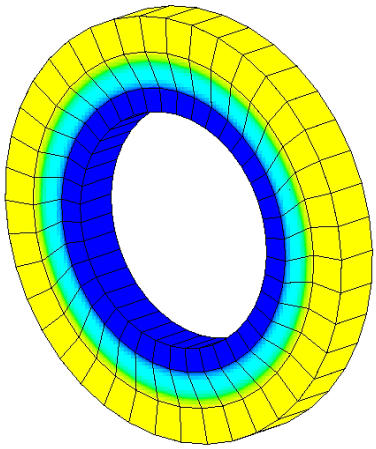

(a) - first torsional mode: 18.52 *Hz*

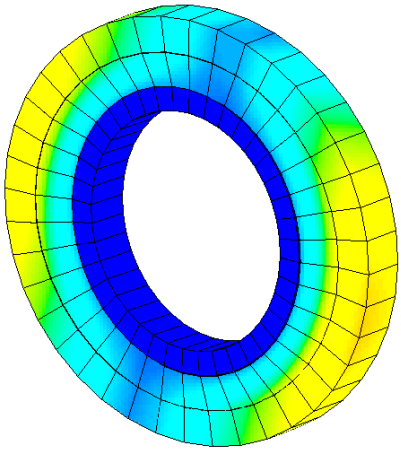

(b) - first bending mode: 22.75 *Hz*

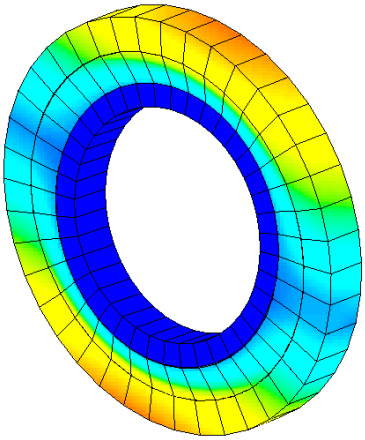

(c) - second bending mode: 22.75 *Hz*

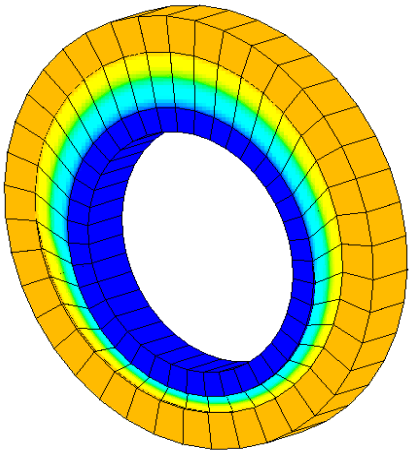

(d) - first axial mode: 30.55 *Hz*

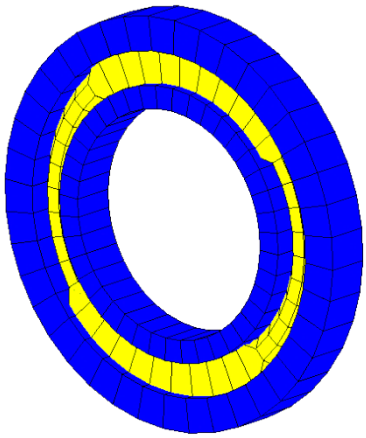

(e) - first rubber mode: 180.17 *Hz*

Figure (3.18) - Modes of vibration of the inserts with local resonance

3.4. Campbell Diagrams of the Drillstrings

The Campbell diagram represents the natural frequency versus the rotation speed of the drillstring characteristics. The diagram displays the evolution of the natural frequencies corresponding to the different mode of vibration as a function of the rotation speed of the shaft. The diagram is named after Wilfred Campbell who introduced the concept in 1924.

Figure (3.19) shows the Campbell diagrams for the drillstring with uniform shaft at axial loads of 0 and 0.15*MN*.

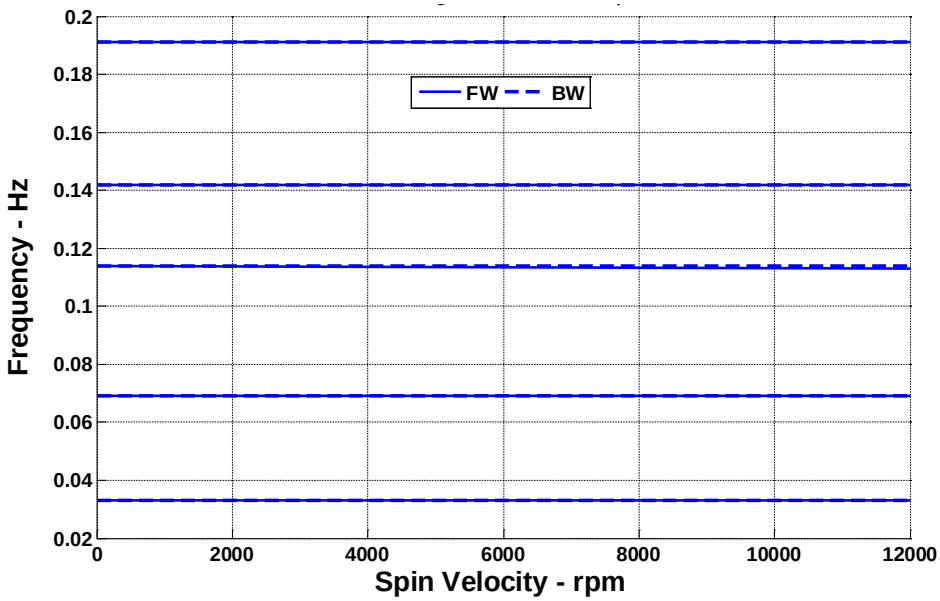

(a) - $F_{axial} = 0\ N$

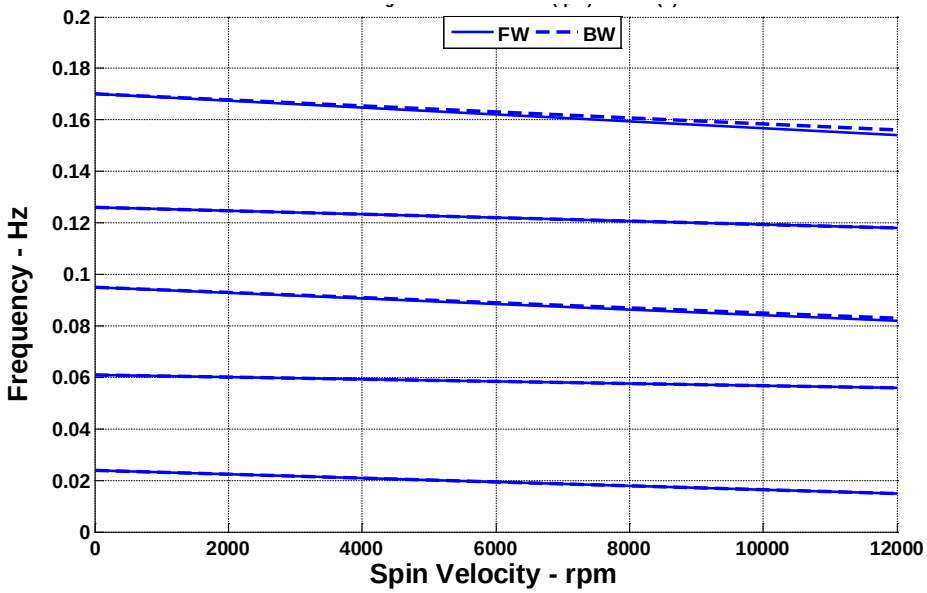

(b) - $F_{axial} = 0.15\ MN$

Figure (3.19) – Campbell diagrams for drillstrings with uniform shaft

Figure (3.20) shows the Campbell diagrams for the drillstring with 120 plain periodic inserts at axial loads of 0 and 0.15*MN*.

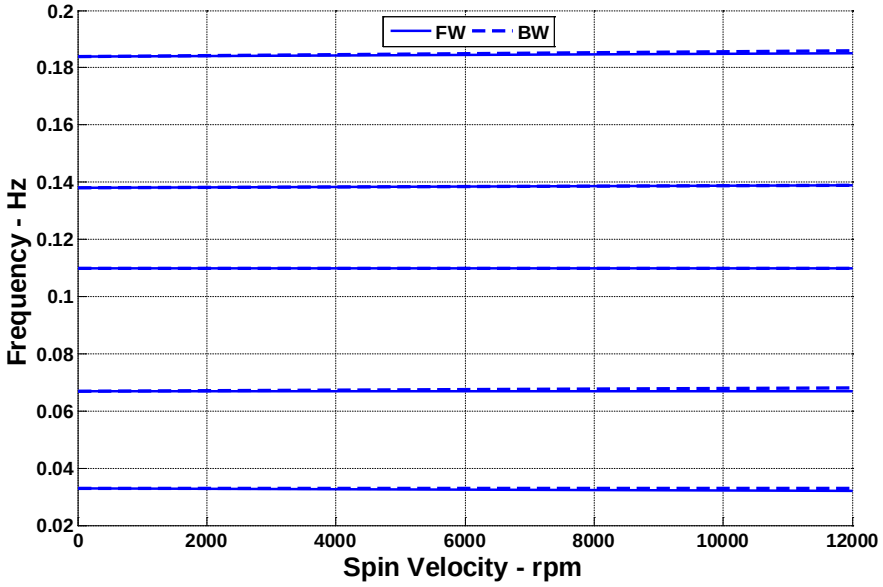

(a) - $F_{axial} = 0\ N$

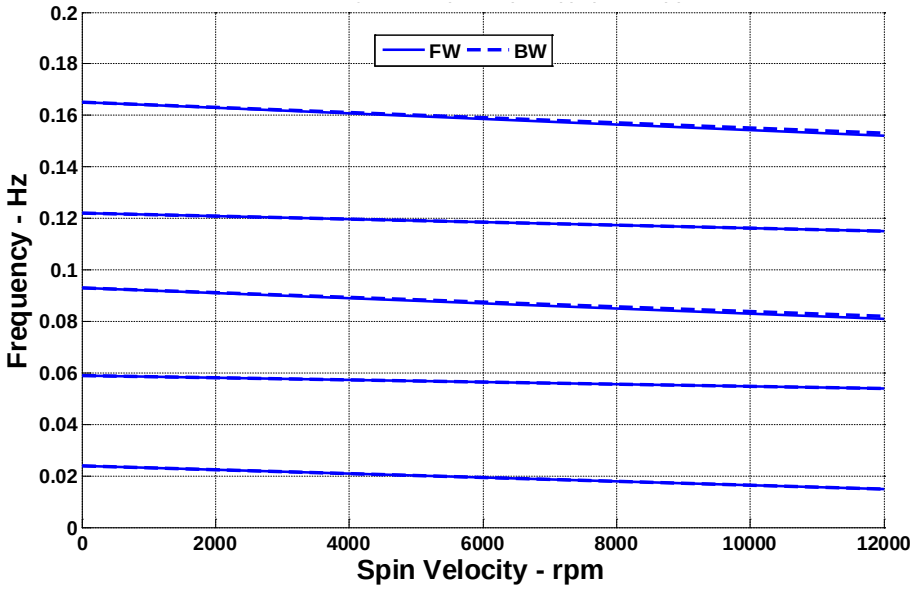

(b) - $F_{axial} = 0.15\ MN$

Figure (3.20) – Campbell diagrams for drillstrings with 120 periodic plain inserts

Figure (3.21) shows the Campbell diagrams for the drillstring with 120 periodic inserts with *LR* at axial loads of 0 and 0.15*MN*.

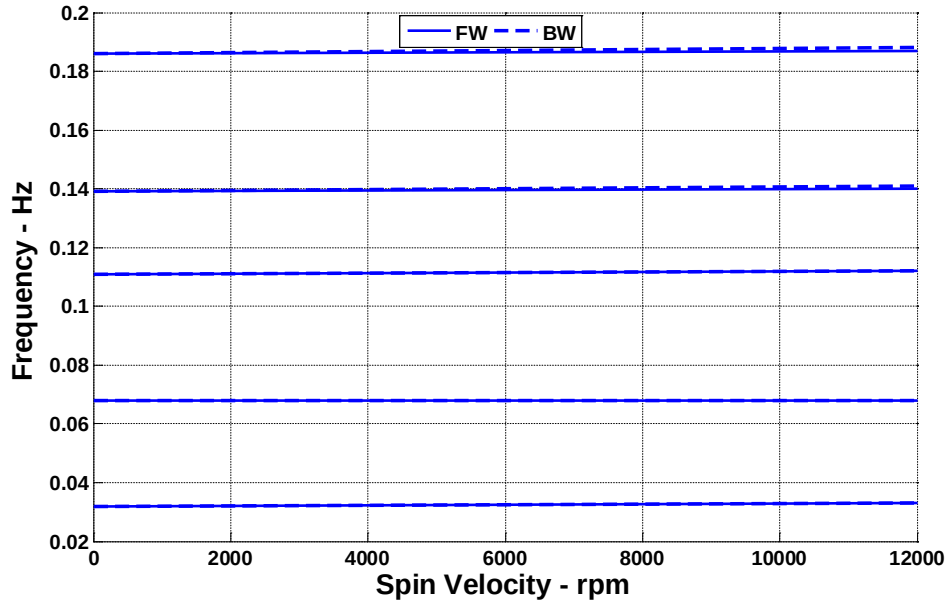

(a) $F_{axial} = 0\ N$

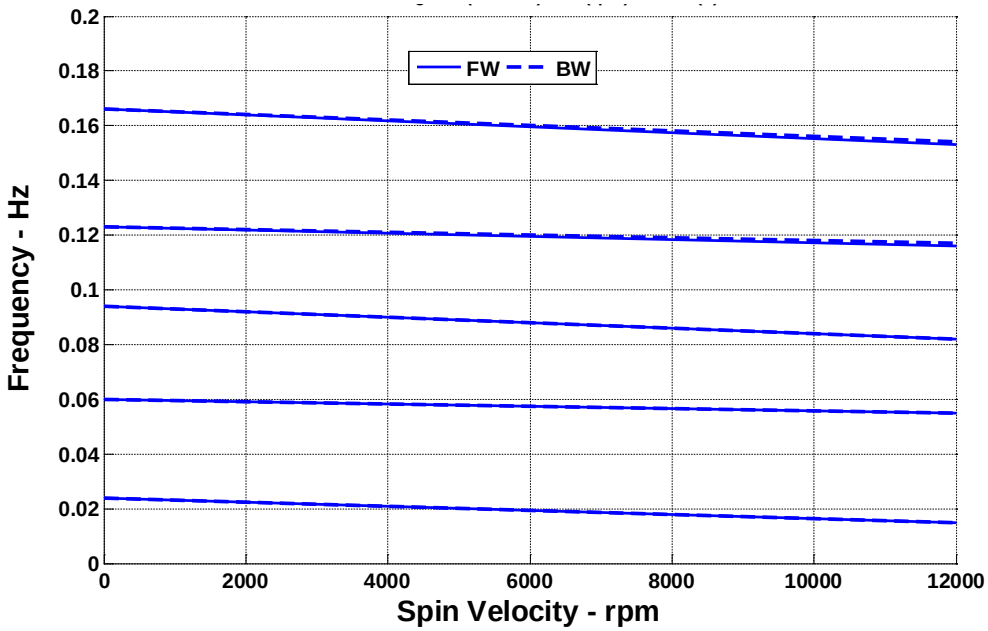

(b) $F_{axial} = 0.15\ MN$

Figure (3.21) – Campbell diagrams for drillstrings with 120 periodic inserts with *LR*

Figures (3.19), (3.20), and (3.21) indicate that the addition of the inserts did alter significantly the natural frequencies of the drillstrings and the natural frequencies remain essentially constant for the considered range of spinning speeds. Furthermore, the difference between the forward and backward frequencies of all the three configurations of the drillstrings is rather insignificant.

However, when an axial load is applied to the drillstrings, the natural frequencies drop considerably as the spinning speed is increased.

3.5. Summary

This chapter has presented a finite element modeling of conventional drillstrings and drillstrings with periodic inserts that have built-in sources of local resonance (*LR*). The developed models aim at demonstrating the effectiveness of the drillstrings with periodic *LR* inserts in simultaneously controlling the axial, bending, and torsional modes of vibration of practical drillstrings particularly at low excitation frequencies. Such effectiveness stems from the ability of the periodic local sources of resonance in shifting the zones of the stop bands to low frequencies which are compatible to the frequencies experienced by practical drillstrings.

The favorable filtering characteristics of the drillstrings with periodic *LR* inserts are achieved when the *VEM* are tuned to have storage moduli that can coincide with the frequencies of the drillstrings. Stop bands are obtained at frequencies as low as 5 Hz which makes the application of the proposed concept practical for many of the existing drillstrings.

Chapter 4: Band Gap Characteristics of a Drillstrings with Periodic Local Sources of Resonance

4.1. Overview

Periodic structures, whether passive or active, are structures that consist of identical substructures, or cells, connected in an identical manner as shown in Figs. 1 and 2. Because of their periodic nature, these structures exhibit unique dynamic characteristics that make them act as mechanical filters for wave propagation. As a result, waves can propagate along the periodic structures only within specific frequency bands called the ‘‘*Pass Bands*’’ and wave propagation can be completely blocked within other frequency bands called the ‘‘*Stop Bands*.’’ The spectral width and location of these bands are fixed for passive periodic structures, and tunable in response to the structural vibration for active periodic structures.

The theory of periodic structures was originally developed for solid state applications (Brillouin, 1946) and extended, in the early seventies, to the design of mechanical structures (Mead, 1970 and Cremer *et al.*, 1973). Since then, the theory has been extensively applied to a wide variety of structures such as spring-mass systems (Faulkner and Hong, 1985), periodic beams (Mead, 1971 and 1975), stiffened plates (Sen Gupta, 1970), ribbed shells (Mead and Bardell, 1987) and space structures. Apart from their unique filtering characteristics, the ability of periodic structures to transmit waves, from one location to another, within the pass bands can be greatly reduced when the ideal periodicity.

In this chapter, the theory of periodic structures will be applied to structures with periodic inserts that have built-in local sources of resonance in an attempt to shift the zones of stop bands to lower frequencies. In this regards, the wealth of the new literature will be capitalized on. Examples of such recent publications include the work of Nouh *et al.* (2014 and 2015).

4.2. Analysis of Periodic Drillstrings using Transfer Matrix Method

The equation of motion of the element can be written accordingly as:

$$[M_T^e]\{\ddot{\Delta}^e\} + [K_T^e]\{\Delta^e\} = \{F\} \tag{4.1}$$

where $\{F\}$ is the force vector that includes the effect of interactions with the well walls and rock formation. Equation (4.1) can be written as:

$$\begin{bmatrix} M^e_{LL} & M^e_{LR} \\ M^e_{RL} & M^e_{RR} \end{bmatrix} \begin{Bmatrix} \{\ddot{\Delta}^e\}_{L_e} \\ \{\ddot{\Delta}^e\}_{R_e} \end{Bmatrix} + \begin{bmatrix} K^e_{LL} & K^e_{LR} \\ K^e_{RL} & K^e_{RR} \end{bmatrix} \begin{Bmatrix} \{\Delta^e\}_{L_e} \\ \{\Delta^e\}_{R_e} \end{Bmatrix} = \begin{Bmatrix} F_{L_e} \\ F_{R_e} \end{Bmatrix} \tag{4.2}$$

where M_{ij} and K_{ij} are appropriately partitioned matrices of the mass and stiffness matrices. Also, $\{\Delta^e\}$ and $\{F\}$ define the deflection and force vectors with subscripts L_e and R_e denoting the left and right sides of the eth element.

For a sinusoidal excitation at a frequency ω, equation (4.2) can be rearranged to assume the following form:

$$\begin{Bmatrix} \{\Delta^e\}_{L_{e+1}} \\ \{F\}_{L_{e+1}} \end{Bmatrix} = \begin{bmatrix} -K_{d_{LR}}^{-1}K_{d_{LL}} & K_{d_{LR}}^{-1} \\ K_{d_{RR}}K_{d_{LR}}^{-1}K_{d_{LL}} - K_{d_{RL}} & -K_{d_{RR}}K_{d_{LR}}^{-1} \end{bmatrix} \begin{Bmatrix} \{\Delta^e\}_{L_e} \\ \{F\}_{L_e} \end{Bmatrix} \qquad (4.3)$$

where $K_{d_{ij}}$ are the elements of the partitioned dynamic matrix $[K_d^e] = [K_T^e] - \omega^2[M_T^e]$.

Graphically, equation (4.3) can be represented as shown in Figure (4.1).

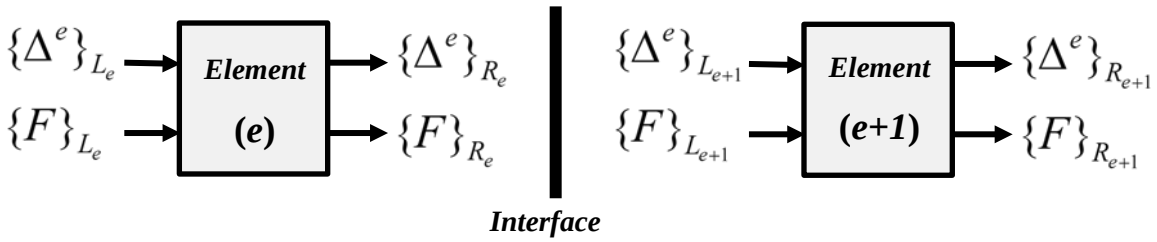

Figure (4.1) – Interaction between two neighboring periodic shaft elements

In a more compact form, equation (4.3) can be written as:

$$S_{e+1} = [T_e]S_e \qquad (4.4)$$

where S_e and $[T_e]$ denote the transfer matrix of the drillstring and the state vector $S_e = \left\{\{\Delta^e\}_{L_e} \ \{F\}_{L_e}\right\}^T$.

The transfer matrix can be used, as described in section 3.1, to determine the pass and stop band characteristics of the drillstring.

i. Passive Periodic drillstring:

Considering a unit cell of the periodic drillstring as shown in Figure (4.2), then the dynamic characteristics of the individual substructure (*a* or *b*) can be described by the transfer matrices $[S_a]$ and $[S_b]$, which can be obtained from equation (4.4).

Combining the transfer matrices of the substructures *a* and *b*, yields the transfer matrix [*T*] for the unit cell as follows:

$$[T] = [T_b]\,[T_a] \tag{4.5}$$

The pass and stop bands characteristics of the periodic drillstring can then be determined by investigating the eigenvalues of the transfer matrix [*T*] for different combinations of the longitudinal rigidities and physical properties of the segments *a* and *b*.

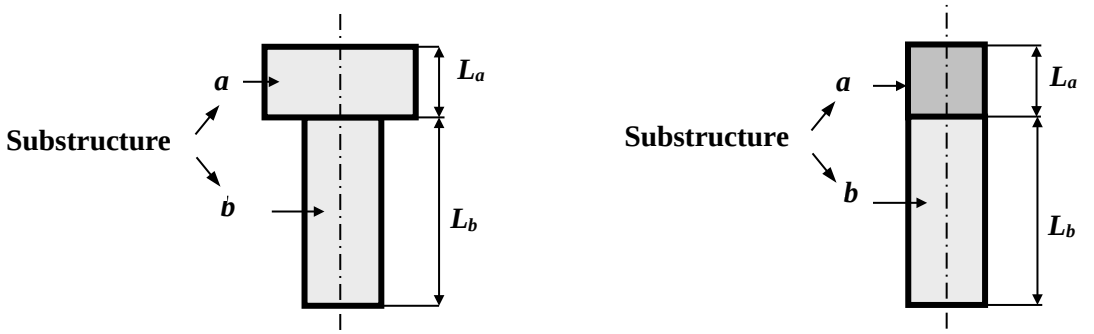

(a) - Geometrical discontinuity (b) – material discontinuity

Figure (4.2) –Unit cell of passive periodic shaft

From equation (4.4), the transfer matrix relates the state vector at the left end of $e+1^{th}$ cell to that at the left end of the e^{th} cell. Also, note that u_L and F_L define the deflection and force vectors.

Equation (4.4) can also be written as (Asiri *et al.,* 2005-2006; Baz, 2001):

$$S_{e+1} = \lambda\, S_e \tag{4.6}$$

indicating that the eigenvalue λ of the matrix [*T*] is the ratio between the state vectors at two consecutive cells.

Therefore, one can draw the following conclusions:

i. If $|\lambda| = 1$, then $S_{e+1} = S_e$ and the state vector propagates along the structure as is. This condition defines a "***Pass Band***" condition.

and ii. If $|\lambda| < 1$, then $S_{e+1} < S_e$ and the state vector is attenuated as it propagates along the structure. This condition defines a "***Stop Band***" condition.

A further explanation of the physical meaning of the eigenvalue λ can be extracted by rewriting it as:

$$\lambda = e^{\mu} = e^{\alpha + i\beta} \tag{4.7}$$

where μ is defined as the "*Propagation Constant*" which has a real part (α) = the logarithmic decay and imaginary part (β) = the phase difference between the adjacent cells.

ii. Stop and Pass Bands of a Passive Periodic Drillstring:

Considering a drillstring that has the main geometrical and physical characteristics listed in Table (4.1).

Table (4.1) - The main geometrical and physical characteristics of a drillstring

Parameter	**Value**
Total length	500 *m*
Outer diameter (d_o)	0.0635 *m*
Inner diameter (d_i)	0.0543 *m*
Cell length (l_b)	4 *m*
Collar outer diameter (d_c)	0.2 *m*
Collar length (l_a)	1 *m*
Material	Steel
Young's modulus	207 *GPa*
Density	8,010 kg/m^3
Poisson's ratio	0.3
Number of cells	20

Figure (4.3a) shows the pass and stop bands of the passive drillstings experiencing axial and torsional vibrations. It is evident that the torsional mode experiences a pass band between 0-8Hz while the axial mode has a wider pass band between 0-25Hz.

The effects of these pass and stop bands on the drillstring's frequency response, due to uniform sinusoidal excitation at its free end, are exhibited in Figures (4.3b) and (4.3c) for the axial and torsional vibrations respectively.

The figures display comparisons between the frequency response of the uniform and periodic drillstrings to emphasize the importance of using the periodic design in blocking multi-modes of vibration in the axial and torsional directions. Such vibration blocking occurs over broad frequency bands.

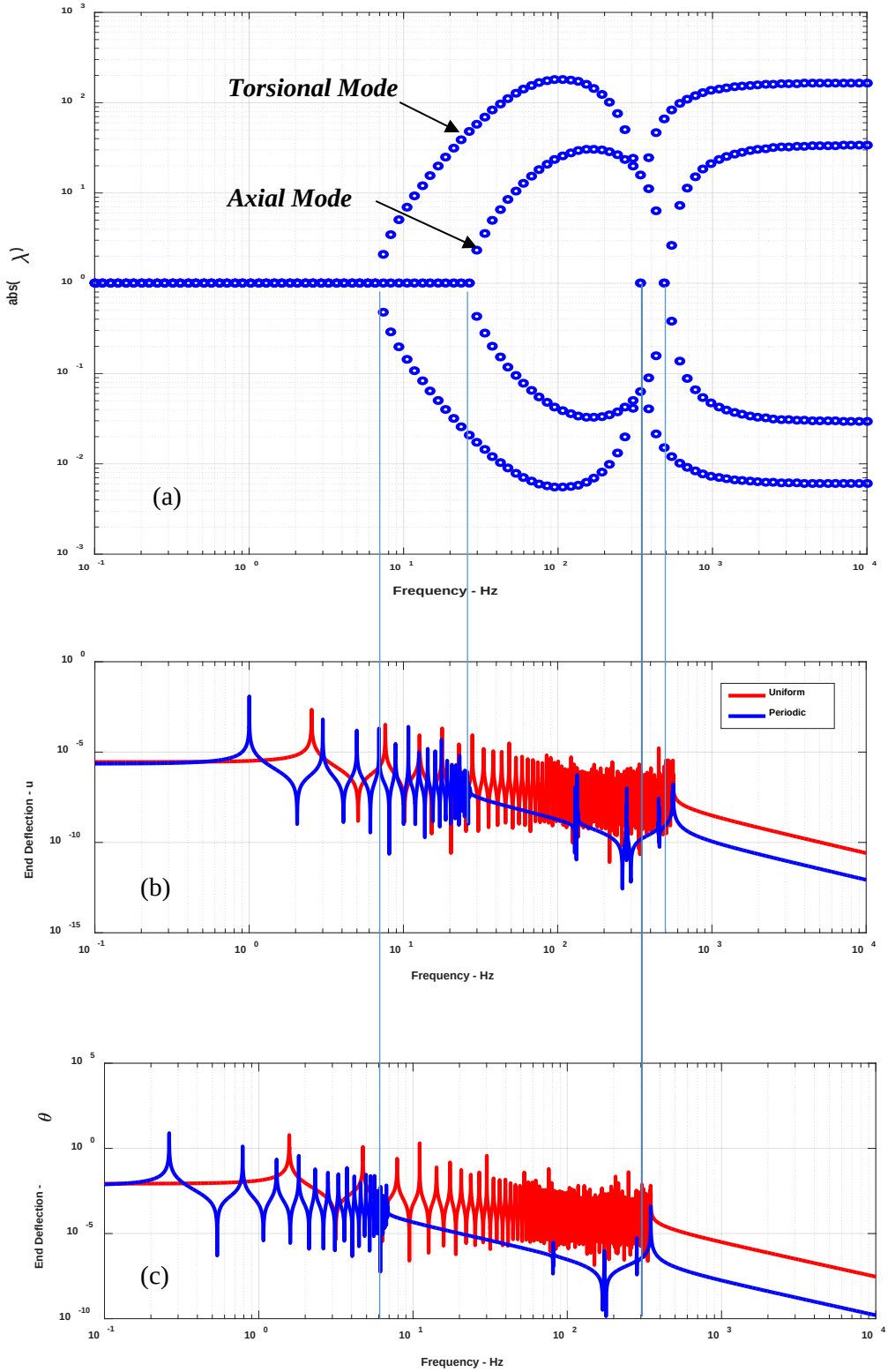

Figure (4.3) –Stop and pass bands of a unit cell of a passive periodic shaft

iii. Effect of Stick-Slip Characteristics of a Passive Periodic Drillstring:

The effect of the stick-slip conditions is simulated by the nonlinear characteristics of the friction coefficient which represents the interaction between the drillstring and the rocks. Such a characteristics is shown in Figure (4.4) and has its basis in the work of Yigit and Christoforou (2006). In their work, the friction coefficient μ is assumed to be given by:

$$\mu = \mu_o \left(\tanh \dot{\phi} + \frac{\alpha \dot{\phi}}{1 + \beta \dot{\phi}^{2\gamma}} + \nu \dot{\phi} \right) \tag{4.8}$$

where the parameters $\mu_o, \alpha, \beta, \gamma,$ and ν are determined experimentally.

In Figure (4.4), $\mu_o, \alpha, \beta, \gamma,$ and ν are assumed to be 0.04, 1, 1, 1, and 0.

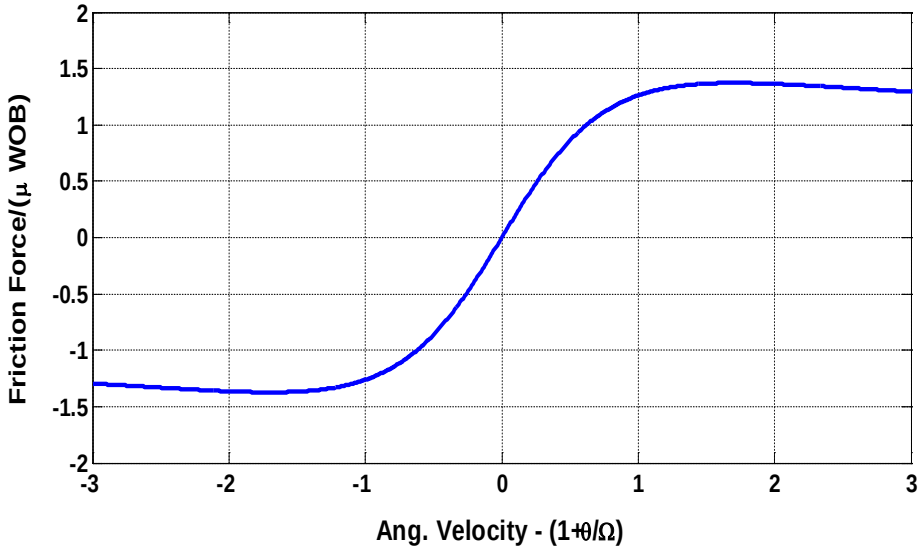

Figure (4.4) –Dimensionless coefficient of friction of the drillstring

The effect of the nonlinear stick-slip characteristics of the drillstring on its time response is shown in Figure (4.5). The figure displays comparisons between the responses of the uniform and periodic drillstrings to demonstrate the effectiveness of using the periodic design in attenuating multi-modes of vibration in the axial and torsional directions.

The figure indicates clearly that the use of the periodic drillstring has resulted in lowering the peak amplitudes of vibration and the dominant frequency content of the response as compared to the uniform drillstring. The effect is more significant in the torsional direction as evident in Figure (4.5b).

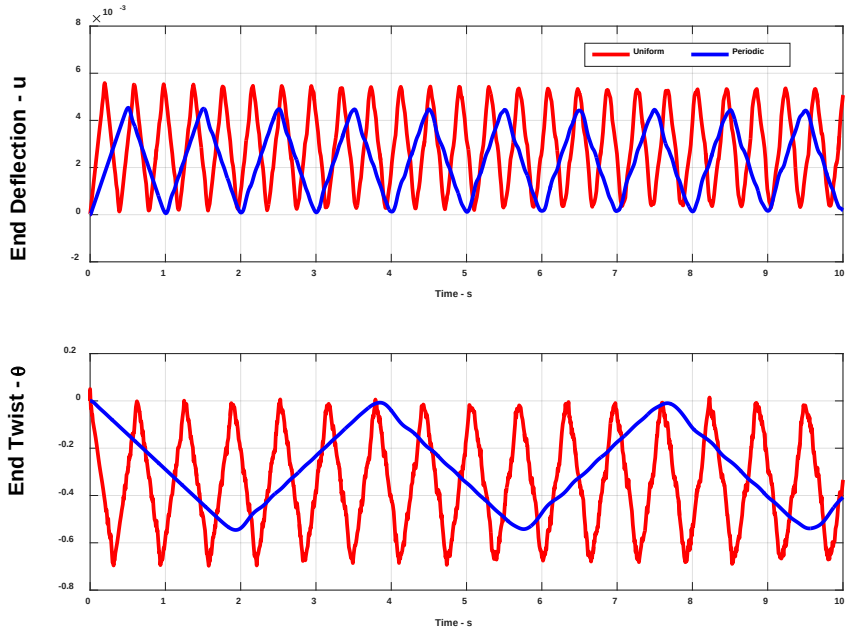

(a)

(b)

Figure (4.5) –Comparison between the time response of the periodic and uniform drillstrings due to stick-slip conditions

4.3. The Stop and Pass Bands of Drillstrings with Periodic LR inserts

In this section, the stop and pass bands of damped drillstrings with periodic LR inserts are determined using an approach which is compatible with damped-gyroscopic systems while maintaining the concept of Bloch wave propagation in periodic structures. In this approach, the dispersion curves of damped periodic materials are determined based on real wavenumbers versus complex frequencies. The obtained characteristics would relate to wave propagation admitting attenuation due to energy dissipation.

Such an approach has not been considered before in the literature particularly for gyroscopic systems.

Furthermore, this section will present also a novel approach to the analysis of Bloch waves in periodic systems with viscoelastic damping which has not been considered at all in the literature. Specifically, the viscoelastic damping is described in the time domain in a manner which is compatible with the finite element formulation.

In order to develop the proposed approach, two cases will be considered whereby the viscoelastic damping is described in the frequency domain by the complex modulus and in the time domain by the Golla-Hughes-McTavish model.

i. <u>Using the Complex Modulus</u>:

In this case, the finite element model of a unit cell of the drillstring with periodic *LR* inserts can be written as follows:

$$M\ddot{u} + C\dot{u} + (K_R + iK_I)u = f \tag{4.9}$$

where M, C, K_R, and K_I denote the mass, gyroscopic, real stiffness, and imaginary stiffness respectively. Also f and u define the forcing function acting on the drillstring and the resulting nodal deflection vector, respectively. The two components K_R, and K_I arise from the complex modulus description of the viscoelastic damping treatment,

The nodal deflection vector of a unit cell u is defined as:

$$u = \{u_b \quad u_i \quad u_L\}^T \tag{4.10}$$

where u_b, u_i, and u_L denote the boundary, internal, and lower deflection vectors as shown in Figure (4.6).

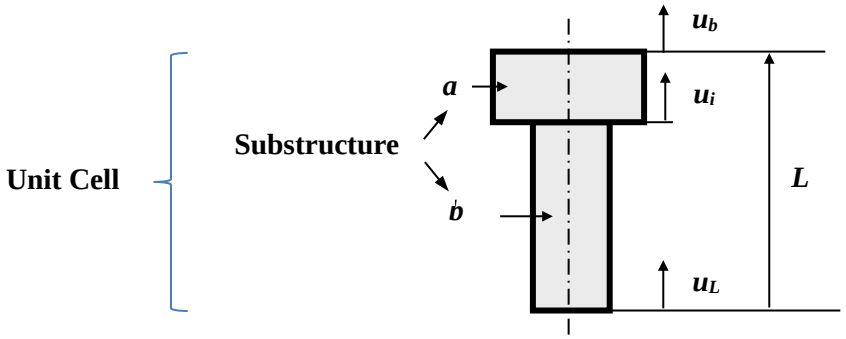

Figure (4.6) –Degrees of freedom of a unit cell of passive periodic shaft

This vector is condensed to support Bloch wave propagation. Hence, the displacements at the boundaries are related as follows:

$$u_L = e^{-ikL} u_b \tag{4.11}$$

where k and L denote the wave number and the length of the unit cell, respectively.

Hence, define an independent nodal deflection vector $\bar{u}$ such that:

$$\bar{u} = \{u_b \quad u_i\}^T \tag{4.13}$$

The deflection vectors u and $\bar{u}$ are related as follows:

$$u = T\,\bar{u} \tag{4.14}$$

where T is a transformation matrix such as:

$$T = \begin{bmatrix} I & 0 & e^{-ikL} I \\ 0 & I & 0 \end{bmatrix}^T \tag{4.15}$$

Substituting Eqs. (4.14) and (4.15) into Eq. (4.9), it reduces to:

$$\bar{M}\,\ddot{\bar{u}} + \bar{C}\,\dot{\bar{u}} + (\bar{K}_R + i\bar{K}_I)\,\bar{u} = \bar{f} \tag{4.16}$$

where $\bar{M} = T^* M T$, $\bar{C} = T^* C T$, $\bar{K}_R = T^* K_R T$, $\bar{K}_I = T^* K_I T$ and $\bar{f} = T^* f$.

Eqn. (4.16) is now cast in the following state-space form (Meirovitch 2010; Hussein 2009; and Hussein and Fraizer 2010):

$$\begin{bmatrix} 0 & \bar{M} \\ \bar{M} & \bar{C} \end{bmatrix} \dot{\bar{y}} + \begin{bmatrix} -\bar{M} & 0 \\ 0 & \bar{K} \end{bmatrix} \bar{y} = \begin{Bmatrix} 0 \\ \bar{f} \end{Bmatrix} \tag{4.17}$$

where $\bar{y} = \left\{ \dot{\bar{u}} \quad \bar{u} \right\}^T$ and $\bar{K} = \bar{K}_R + i\bar{K}_I$. Assuming the state-space solution:

$$\bar{y} = e^{\lambda t} \hat{y} \tag{4.18}$$

This solution leads to the following eigenvalue problem:

$$\left(\begin{bmatrix} 0 & \bar{M} \\ \bar{M} & \bar{C} \end{bmatrix} \lambda + \begin{bmatrix} -\bar{M} & 0 \\ 0 & \bar{K} \end{bmatrix} \right) \hat{y} = 0 \tag{4.19}$$

which can be rewritten in the following compact and standard form:

$$A\hat{y} = \lambda \hat{y} \tag{4.20}$$

With the matrix A given by:

$$A = -\begin{bmatrix} 0 & \bar{M} \\ \bar{M} & \bar{C} \end{bmatrix}^{-1} \begin{bmatrix} -\bar{M} & 0 \\ 0 & \bar{K} \end{bmatrix} \tag{4.21}$$

Note that all the entries of the matrix *A* are function of the dimensionless wave number *kL*. Then, the eigenvalues of the matrix *A* can be determined for different values of the wave number *kL*. The eigenvalues λ_s are complex and generally assume the following form:

$$\lambda_s(kL) = -\zeta_s \omega_{rs} \pm i\omega_{ds} \qquad s = 1,.., n \tag{4.22}$$

With ζ_s, ω_{rs}, and ω_{ds} denote the damping ratio, undamped resonant frequency, and damped resonant frequency, respectively.

Hence, damped resonant frequency and the damping ratio can be extracted as follows:

$$\omega_{ds} = imag\left(\lambda_s(kL)\right) \tag{4.23}$$

and

$$\zeta_s = -\frac{real\left(\lambda_s(kL)\right)}{\left|\lambda_s(kL)\right|} \tag{4.24}$$

Plotting the resonant frequency ω_{ds} against the wave number kL, gives the dispersion characteristics of the unit cell of the drillstring with *LR* inserts. It further defines the zones of stop and pass bands as will be illustrated.

Numerical Example:

For the drillstring described in Table 4.1, consider that the viscoelastic material used in the *LR* inserts has a complex modulus given by: $G_v = 40E6(1+1i)$ indicating a storage modulus of 40E6 *Pa* and loss factor η=1 as shown in Figure (4.7). Note that the experimental data of the viscoelastic material are corresponding to DYAD606 (Soundcoat, Inc., NY).

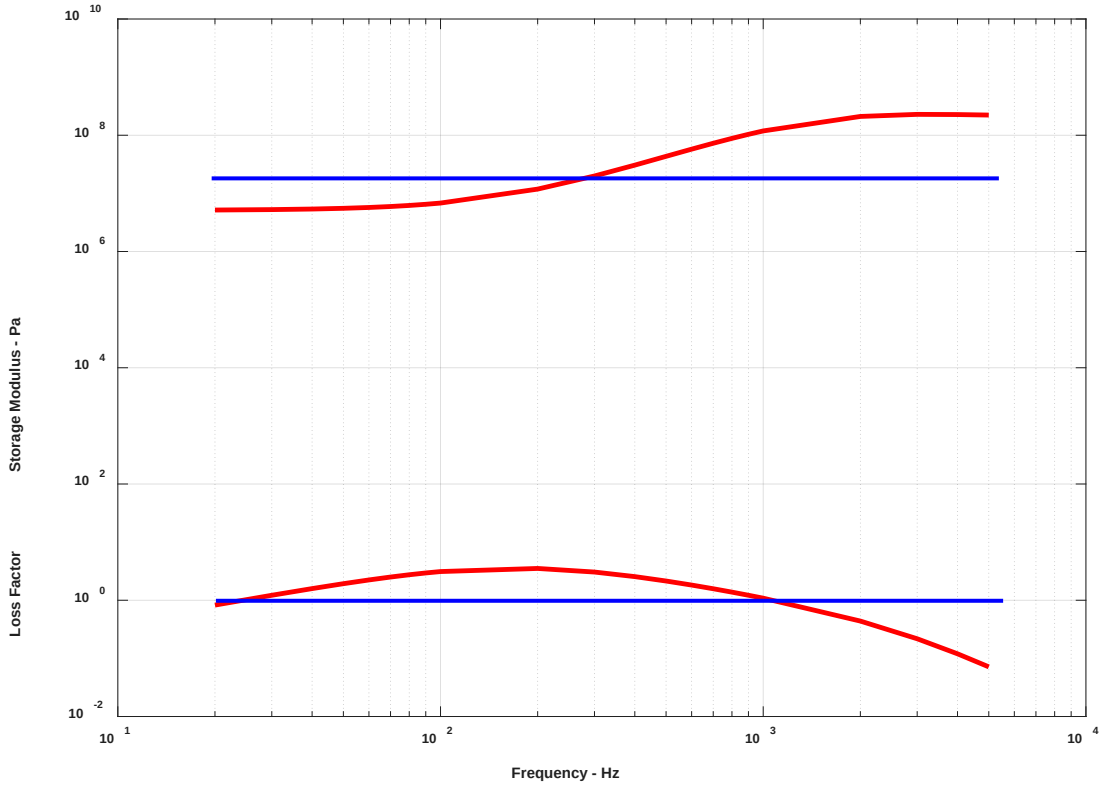

Figure (4.7) - Complex Modulus Model
(Experimental Complex Modulus Model)

Then, the dispersion characteristics of the system are as shown in Figures (4.8) and (4.9) for loss factor η=0 and 1, respectively.

$$G_v = 40E6(1+0i)$$

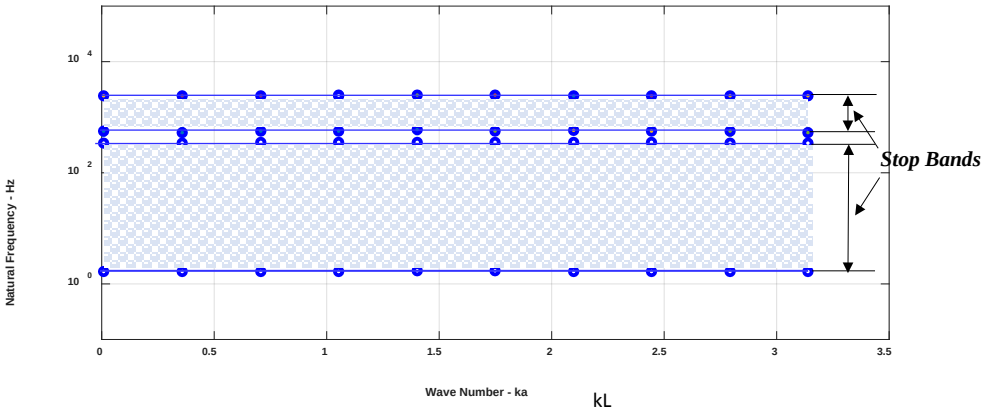

Figure (4.8) –Dispersion characteristics of a unit cell of passive periodic shaft with periodic *LR* insert (η=0)

$$G_v = 40E6(1+1i)$$

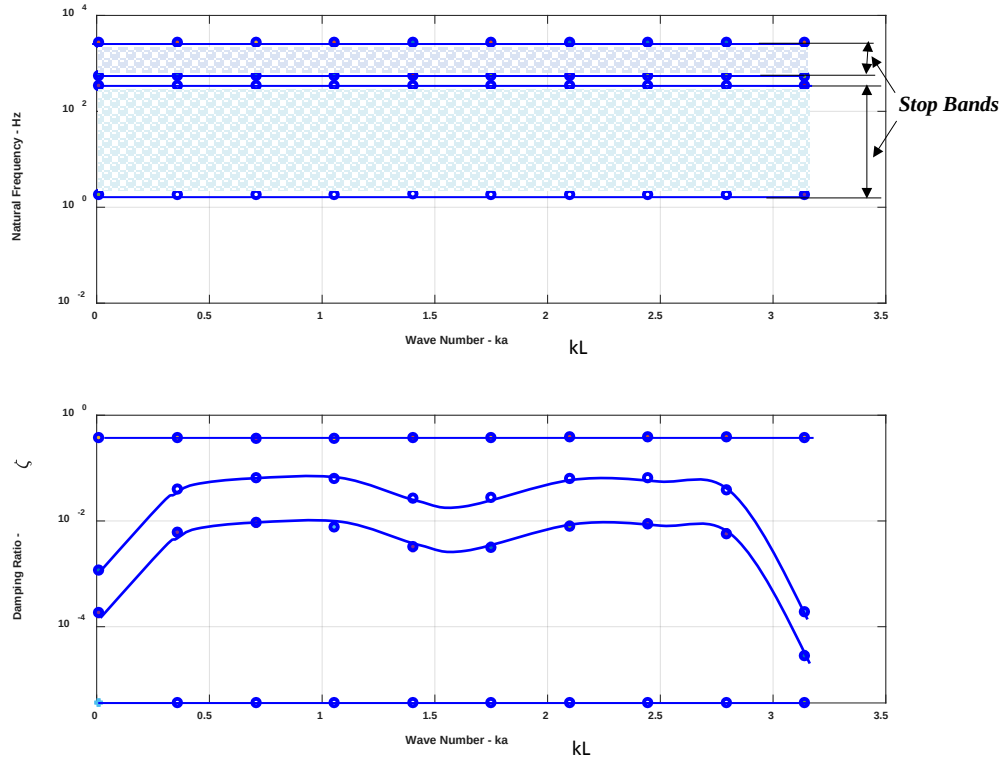

Figure (4.9) –Dispersion characteristics of a unit cell of passive periodic shaft with periodic *LR* insert (η=1)

Figure (4.8) emphasizes that the stop and pass bands are in agreement with those generated by the transfer matrix approach as displayed in Figure (4.3a).

It is also important to note that the dispersion characteristics give the interaction between the spatial and spectral parameters on the width of the stop and pass bands,

ii. Using the Golla-Hughes-McTavish model

The Golla-Hughes-MacTavish (*GHM*) model is developed by Golla and Hughes in 1985. The model describes the shear modulus of viscoelastic materials with a second order differential equation unlike the first order differential equations used to describe the Maxwell, Kelvin-Voigt, Poynting-Thomas, and Zener models. Such a distinction makes it easy to incorporate the dynamics of the viscoelastic materials into finite element models of vibrating structures.

According to the *GHM* formulation, the shear modulus *G* of viscoelastic materials can be written in Laplace domain as

$$G(s) = G_0\left(1 + \sum_{n=1}^{N} \alpha_n \frac{s^2 + 2\zeta_n \omega_n s}{s^2 + 2\zeta_n \omega_n s + \omega_n^2}\right) \tag{4.25}$$

where G_0 is the equilibrium value of the modulus, *i.e.*, the initial value of $G(\omega = 0)$, and s is the Laplace domain variable. The parameters α_n, ζ_n and ω_n are obtained from curve fitting the complex modulus data for a particular viscoelastic material at a given temperature. The summation may be thought of as representing the material modulus as a series of mini-oscillators (second order equations) as suggested by Golla and Hughes (1985). These terms are a representation of the internal variables necessary to describe the characteristics of the viscoelastic materials. The number of terms kept in the expansion is determined by accuracy needed to replicate the real behavior of the material. In many cases only two to four terms are necessary.

Note that the viscoelastic material is represented by a spring-mass-damper assembly which is connected in parallel with another spring K as shown in Figure (4.10). Note that K represents the stiffness of the viscoelastic material under static conditions (*i.e.* at zero frequency ω).

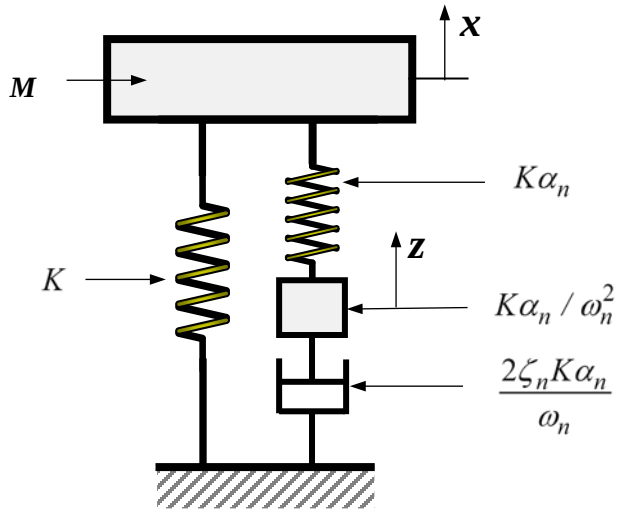

Figure (4.10) – Equivalent system of the *GHM* model

The finite element equation of the unit cell after introducing the Bloch wave assumption is as given by Eqn. (4.16) as follows:

$$\bar{M}\,\ddot{\bar{u}} + \bar{C}\,\dot{\bar{u}} + \bar{K}\,\bar{u} = \bar{f} \tag{4.26}$$

Let $\quad z_1 = \dfrac{{\omega_1}^2}{s^2 + 2\zeta_1\omega_1 s + {\omega_1}^2}\,\bar{u},\; z_2 = \dfrac{{\omega_2}^2}{s^2 + 2\zeta_2\omega_2 s + {\omega_2}^2}\bar{u},\; \ldots\ldots$

Note that z_i defines an "***internal degree of freedom***" (*IDOF*) which describes the motion of a *VEM* modeled by a single mini-oscillator. More *IDOF*s would be added when the *VEM* is modeled by *N* mini-oscillators. The addition of these damping *IDOF*s increases the size of the equations of motion of the structure considerably. Application of classical model reduction techniques, such as Guyan reduction, is essential to reduce the size of the structure/*VEM* model to include only the structural degrees of freedom in order to enhance the computational efficiency.

Then,

$$\left[\begin{array}{c|cccc} \bar{M} & 0 & 0 & .... & 0 \\ \hline 0 & \frac{\bar{K}\alpha_1}{\omega_1^{\,2}} & 0 & .... & 0 \\ 0 & 0 & \frac{\bar{K}\alpha_2}{\omega_2^{\,2}} & .... & 0 \\ .... & .... & .... & .... & .... \\ 0 & 0 & 0 & .... & \frac{\bar{K}\alpha_N}{\omega_N^{\,2}} \end{array}\right]\left\{\begin{array}{c} \ddot{\bar{u}} \\ \ddot{z}_1 \\ \ddot{z}_2 \\ .... \\ \ddot{z}_N \end{array}\right\}+\left[\begin{array}{c|cccc} \bar{C} & 0 & 0 & .... & 0 \\ \hline 0 & \frac{2\zeta_1\alpha_1\bar{K}}{\omega_1} & 0 & .... & 0 \\ 0 & 0 & \frac{2\zeta_2\alpha_2\bar{K}}{\omega_2} & .... & 0 \\ .... & .... & .... & .... & .... \\ 0 & 0 & 0 & .... & \frac{2\zeta_N\alpha_N\bar{K}}{\omega_N} \end{array}\right]\left\{\begin{array}{c} \dot{\bar{u}} \\ \dot{z}_1 \\ \dot{z}_2 \\ .... \\ \dot{z}_N \end{array}\right\}+$$

$$\left[\begin{array}{c|cccc} \bar{K}(1+\alpha_1+\alpha_2+....) & -\bar{K}\alpha_1 & -\bar{K}\alpha_2 & .... & -\bar{K}\alpha_N \\ \hline -\bar{K}\alpha_1 & \bar{K}\alpha_1 & & .... & 0 \\ -\bar{K}\alpha_2 & 0 & \bar{K}\alpha_2 & .... & 0 \\ .... & .... & ..... & ..... & 0 \\ -\bar{K}\alpha_N & 0 & 0 & 0 & \bar{K}\alpha_N \end{array}\right]\left\{\begin{array}{c} \bar{u} \\ z_1 \\ z_2 \\ .... \\ z_N \end{array}\right\}=\left\{\begin{array}{c} f \\ 0 \\ 0 \\ .. \\ 0 \end{array}\right\} \qquad (4.27)$$

In a compact form, Eqn. (4.27) can be rewritten as:

$$\left[\begin{array}{cc} \bar{M} & 0 \\ 0 & M_v \end{array}\right]\left\{\begin{array}{c} \ddot{\bar{u}} \\ \ddot{z} \end{array}\right\}+\left[\begin{array}{cc} \bar{C} & 0 \\ 0 & C_v \end{array}\right]\left\{\begin{array}{c} \dot{\bar{u}} \\ \dot{z} \end{array}\right\}+\left[\begin{array}{cc} \bar{K}(1+\alpha_1+\alpha_2+....) & -\bar{K}_{\bar{u}z} \\ -\bar{K}_{\bar{u}z}^T & \bar{K}_{zz} \end{array}\right]\left\{\begin{array}{c} \bar{u} \\ z \end{array}\right\}=\left\{\begin{array}{c} f \\ 0 \end{array}\right\}$$

$$where\ M_v=\left[\begin{array}{cccc} \frac{\bar{K}\alpha_1}{\omega_1^{\,2}} & 0 & .... & 0 \\ 0 & \frac{\bar{K}\alpha_2}{\omega_2^{\,2}} & .... & 0 \\ .... & .... & .... & .... \\ 0 & 0 & .... & \frac{\bar{K}\alpha_N}{\omega_N^{\,2}} \end{array}\right], C_v=\left[\begin{array}{cccc} \frac{2\zeta_1\alpha_1\bar{K}}{\omega_1} & 0 & .... & 0 \\ 0 & \frac{2\zeta_2\alpha_2\bar{K}}{\omega_2} & .... & 0 \\ .... & .... & .... & .... \\ 0 & 0 & .... & \frac{2\zeta_N\alpha_N\bar{K}}{\omega_N} \end{array}\right],$$

$$\bar{K}_{\bar{u}z}=\left[\begin{array}{cccc} \bar{K}\alpha_1 & \bar{K}\alpha_2 & ..... & \bar{K}\alpha_N \end{array}\right]\ and \qquad (4.28)$$

$$\bar{K}_{zz}=\left[\begin{array}{ccccc} \bar{K}\alpha_1 & 0 & 0 & ..... & 0 \\ 0 & \bar{K}\alpha_2 & 0 & ..... & 0 \\ ..... & ..... & ..... & ..... & ..... \\ 0 & 0 & 0 & ..... & \bar{K}\alpha_N \end{array}\right]\ with\ z=\left\{\begin{array}{cccc} z_1 & z_2 & .... & z_N \end{array}\right\}$$

The internal degrees of freedom of the viscoelastic material *z* are condensed using the "*Static Condensation Method*". This leads to:

$$\bar{K}_{\bar{u}z}\,\bar{u} = \bar{K}_{zz}\,z \quad or \quad z = \bar{K}_{zz}^{-1}\,\bar{K}_{\bar{u}z}\,\bar{u} = R\,\bar{u} \tag{4.29}$$

Hence, the full order state vector $\{X\}$ can be written, in terms of $\{\bar{u}\}$ as

$$\{X\} = \begin{Bmatrix} \bar{u} \\ z \end{Bmatrix} = \begin{Bmatrix} I \\ R \end{Bmatrix} \bar{u} = T_R \bar{u} \tag{4.30}$$

The system equation of motion (4.28) can be cast in the following compact form:

$$M_T \left\{ \ddot{X} \right\} + C_T \left\{ \dot{X} \right\} + K_T \left\{ X \right\} = \left\{ F \right\} \tag{4.31}$$

where:

$$M_T = \begin{bmatrix} \bar{M} & 0 \\ 0 & M_v \end{bmatrix},\ C_T = \begin{bmatrix} \bar{C} & 0 \\ 0 & C_v \end{bmatrix},$$

$$K_T = \begin{bmatrix} \bar{K}(1+\alpha_1+\alpha_2+....) & -\bar{K}_{\bar{u}z} \\ -\bar{K}_{\bar{u}z}^T & \bar{K}_{zz} \end{bmatrix},\ and\ \{F\} = \begin{Bmatrix} f \\ 0 \end{Bmatrix}$$

Using the transformation equation (4.30) reduces the compact system equation of motion (4.31) to:

$$M_R \left\{ \ddot{\bar{u}} \right\} + C_R \left\{ \dot{\bar{u}} \right\} + K_R \left\{ \bar{u} \right\} = \left\{ F_R \right\} \tag{4.32}$$

where:

$$M_R = T_R^T M_T T_R,\ C_R = T_R^T C_T T_R,\ K_R = T_R^T K_T T_R,\ and\ \{F_R\} = T_R^T \begin{Bmatrix} f \\ 0 \end{Bmatrix}$$

Eqn. (4.32) is now cast in the following state-space form:

$$\begin{bmatrix} 0 & M_R \\ M_R & C_R \end{bmatrix} \dot{\bar{y}} + \begin{bmatrix} -M_R & 0 \\ 0 & K_R \end{bmatrix} \bar{y} = \begin{Bmatrix} 0 \\ F_R \end{Bmatrix} \tag{4.33}$$

where $\bar{y} = \left\{ \dot{\bar{u}} \quad \bar{u} \right\}^T$. Assuming the state-space solution:

$$\bar{y} = e^{\lambda t} \hat{y} \tag{4.34}$$

This solution leads to the following eigenvalue problem:

$$\left(\begin{bmatrix} 0 & M_R \\ M_R & C_R \end{bmatrix}\lambda + \begin{bmatrix} -M_R & 0 \\ 0 & K_R \end{bmatrix}\right)\hat{y} = 0 \tag{4.35}$$

which can be rewritten in the following compact and standard form:

$$A\hat{y} = \lambda\hat{y} \tag{4.36}$$

With the matrix *A* given by:

$$A = -\begin{bmatrix} 0 & M_R \\ M_R & C_R \end{bmatrix}^{-1}\begin{bmatrix} -M_R & 0 \\ 0 & K_R \end{bmatrix} \tag{4.37}$$

Note that all the entries of the matrix *A* are function of the dimensionless wave number *kL*. Then, the eigenvalues of the matrix *A* can be determined for different values of the wave number *kL*. The eigenvalues λ_s are complex and generally assume the following form:

$$\lambda_s(kL) = -\zeta_s\omega_{rs} \pm i\omega_{ds} \qquad s=1,..,n \tag{4.38}$$

With ζ_s, ω_{rs}, and ω_{ds} denote the damping ratio, undamped resonant frequency, and damped resonant frequency, respectively.

Hence, damped resonant frequency and the damping ratio can be extracted as follows:

$$\omega_{ds} = imag\left(\lambda_s(kL)\right) \tag{4.39}$$

and

$$\zeta_s = -\frac{real\left(\lambda_s(kL)\right)}{\left|\lambda_s(kL)\right|} \tag{4.40}$$

Plotting the resonant frequency ω_{ds} against the wave number *kL*, gives the dispersion characteristics of the unit cell of the drillstring with *LR* inserts. It further defines the zones of stop and pass bands as will be illustrated.

Numerical Example:

For the drillstring described in Table 4.1, consider that the viscoelastic material used in the *LR* inserts has a single mini-oscillator *GHM* model given by:

$$G_v = 5E6\left(1 + \alpha\frac{s^2 + 2\omega s}{s^2 + 2\omega s + \omega^2}\right)$$

where $\alpha = 39, \omega = 11{,}875\, rad/s,$ and s is the Laplace complex number. Note that the experimental data of the viscoelastic material are corresponding to DYAD606 (Soundcoat, Inc., NY). The model is shown in Figure (4.11).

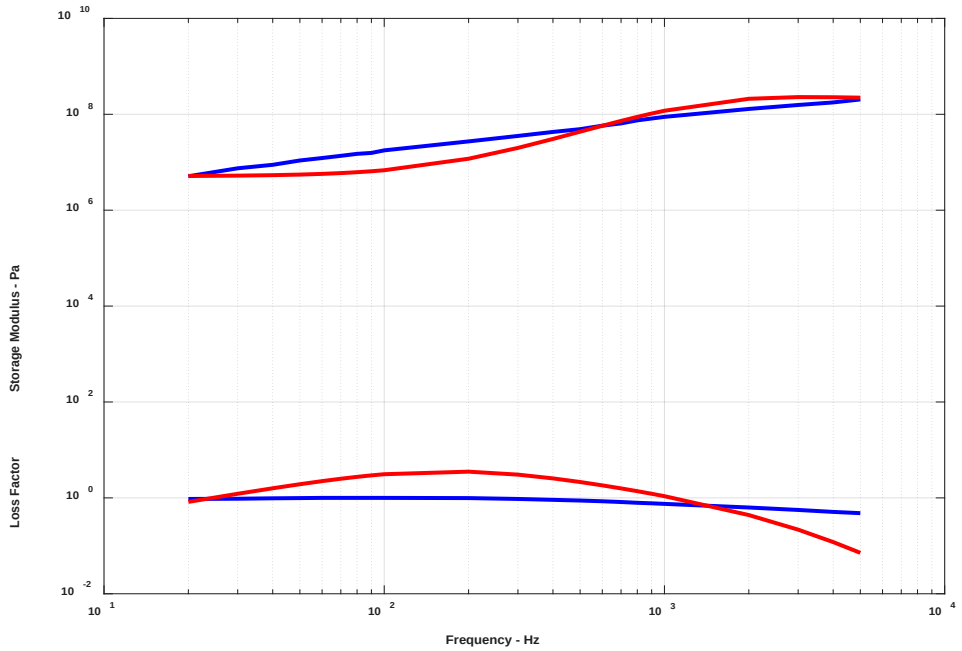

Figure (4.11) – *GHM* Model of the damping treatment with One mini-oscillator (Experimental *GHM* Model)

Then, the dispersion characteristics of the system are as shown in Figures (4.12) and (4.13) for α=0 and 39, respectively.

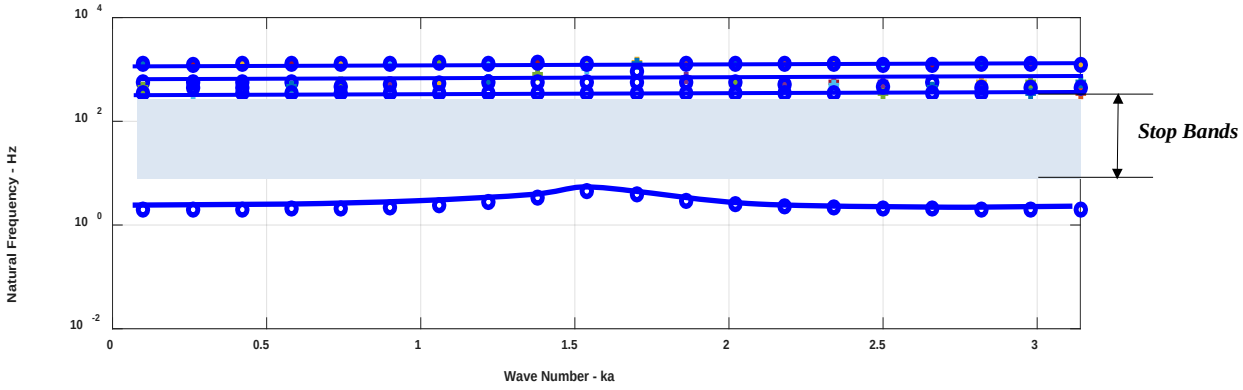

Figure (4.12) –Dispersion characteristics of a unit cell of passive periodic shaft with periodic *LR* insert (*GHM* model with α=0)

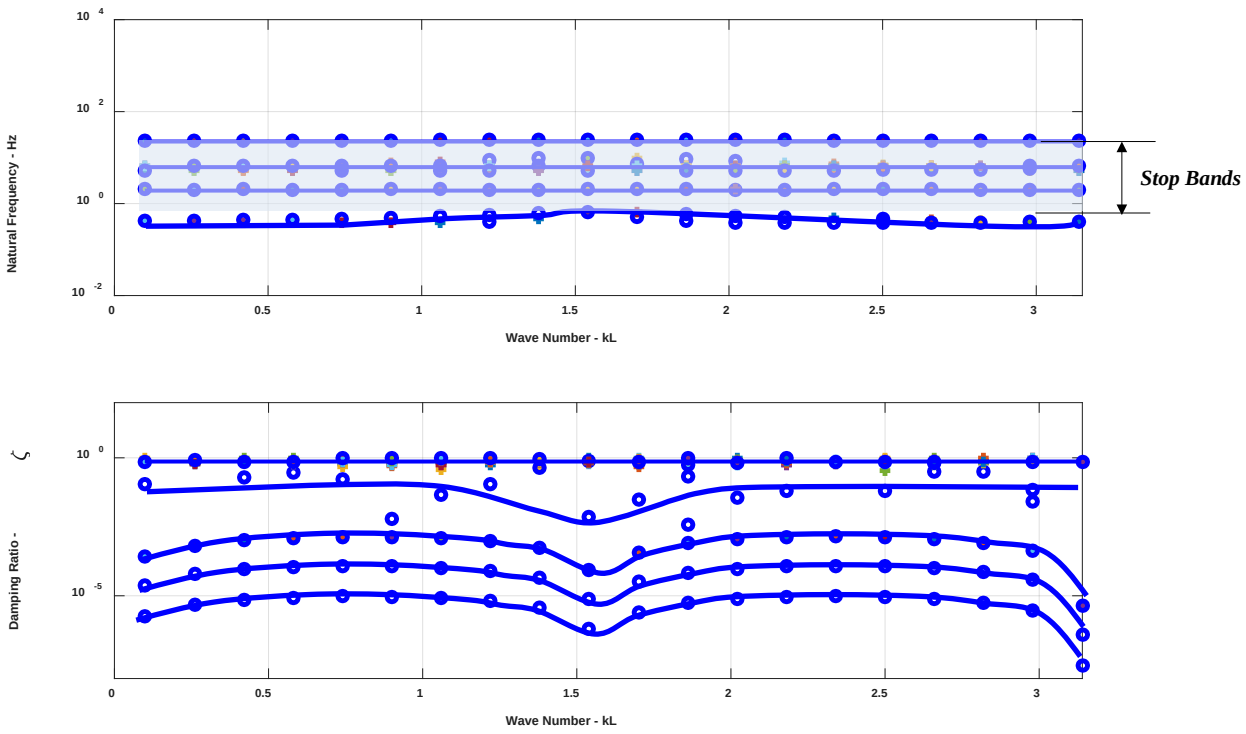

Figure (4.13) –Dispersion characteristics of a unit cell of passive periodic shaft with periodic *LR* insert (*GHM* model with α=39)

iii. Effect of Slip and Stick Conditions

The effect of the nonlinear stick-slip characteristics of the drillstring on its time response is shown in Figure (4.14). The figure displays comparisons between the responses of the drillstring with periodic *LR* inserts when α=0 and 39 to demonstrate the effectiveness of using the periodic design in attenuating multi-modes of vibration in the axial and torsional directions.

The figure indicates clearly that the use of the periodic drillstring has resulted in lowering the peak amplitudes of vibration and the dominant frequency content of the response as compared to the uniform drillstring. The effect is more significant in the torsional direction as evident in Figure (4.14b).

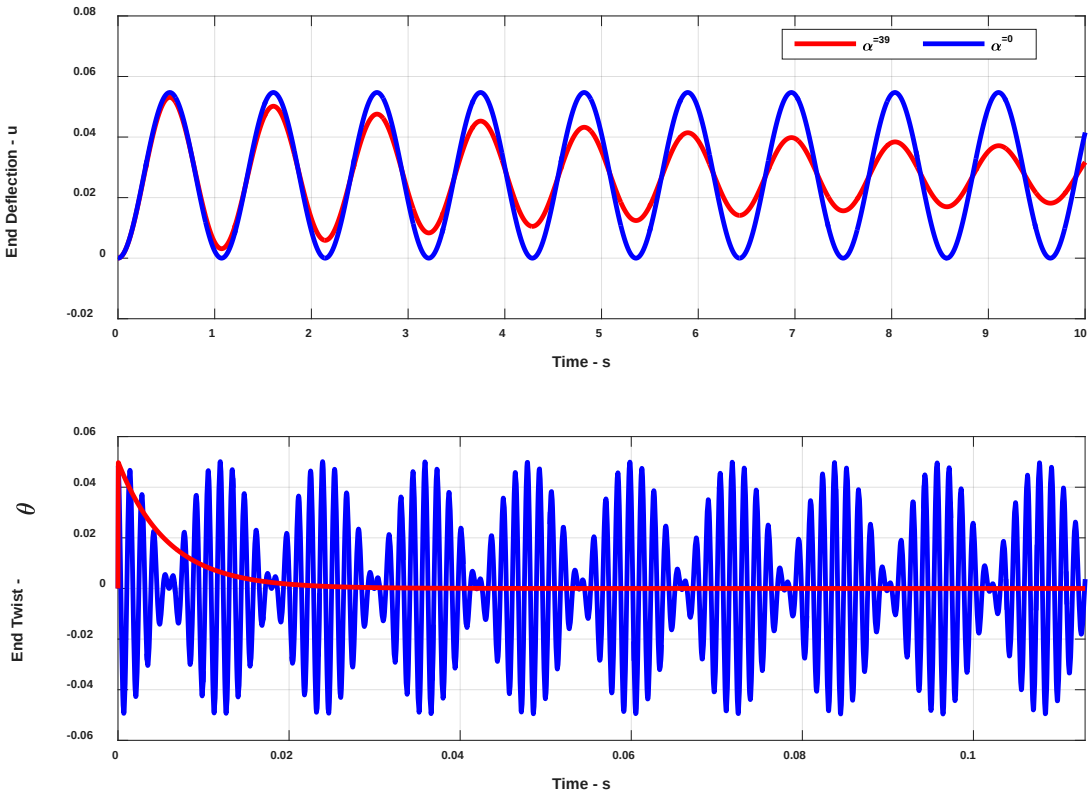

Figure (4.14) –Comparison between the time response of drillstrings with periodic LR Inserts (α=0 and 39) due to stick-slip conditions

4.4 Summary

This chapter has presented the theory of periodic structures in an attempt to determine the pass and stop band characteristics of these structures using the transfer matrix approach and the Bloch wave propagation theory. The transfer matrix method is applied to undamped periodic drillstrings whereas the Bloch wave theory is employed for drillstrings with damped *LR* inserts.

Chapter 5: Experimental Characteristics of a Drillstrings with Periodic Local Sources of Resonance

5.1 Overview:

This chapter presents an experimental realization of the proposed concept of rotating shaft with periodic local sources of resonance.

The experimental performance characteristics of a prototype of the rotating shaft with periodic local sources of resonance are determined under different operating conditions. These characteristics are utilized to validate the predictions of the theoretical finite element model of the shaft assembly.

Furthermore, the experimental results are determined also for uniform shafts in order to provide basis for establishing the merits and effectiveness of the shaft with periodic local sources of resonance in attenuating the structural vibration.

5.2 Experimental Setup

The experimental setup of rotating shaft with periodic local sources of resonance is shown schematically in Figure (5.1) and photographically in Figure (5.2).

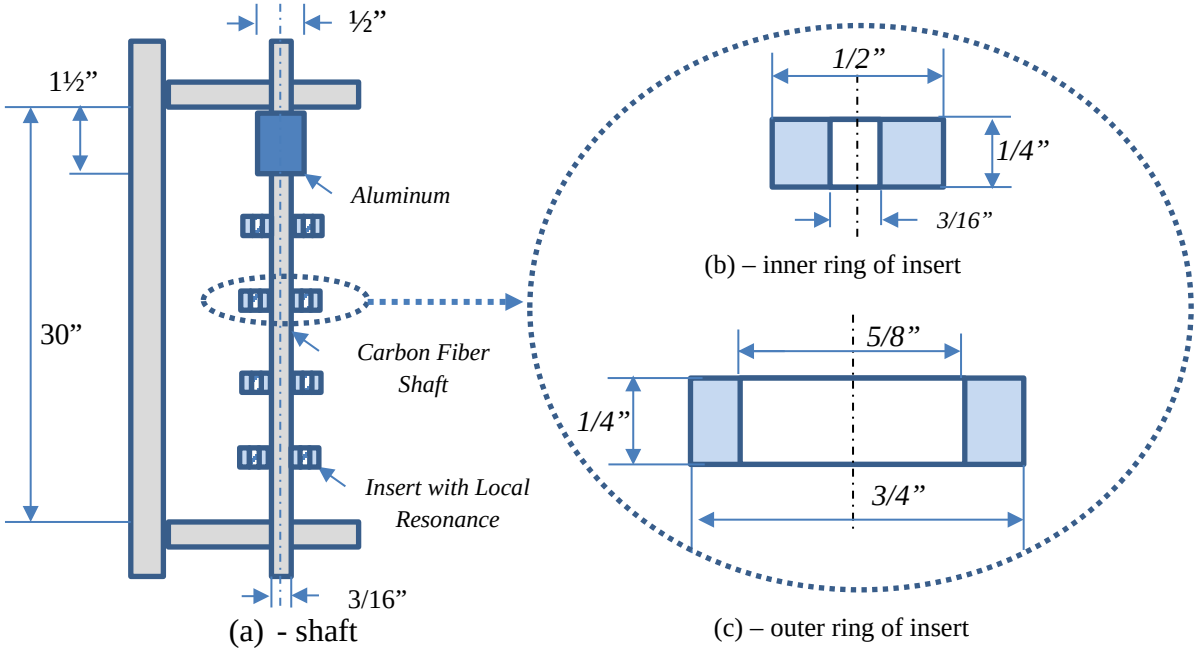

Figure (5.1) – Schematic drawing and geometrical parameters of the experimental shaft and the inserts with local sources of resonance

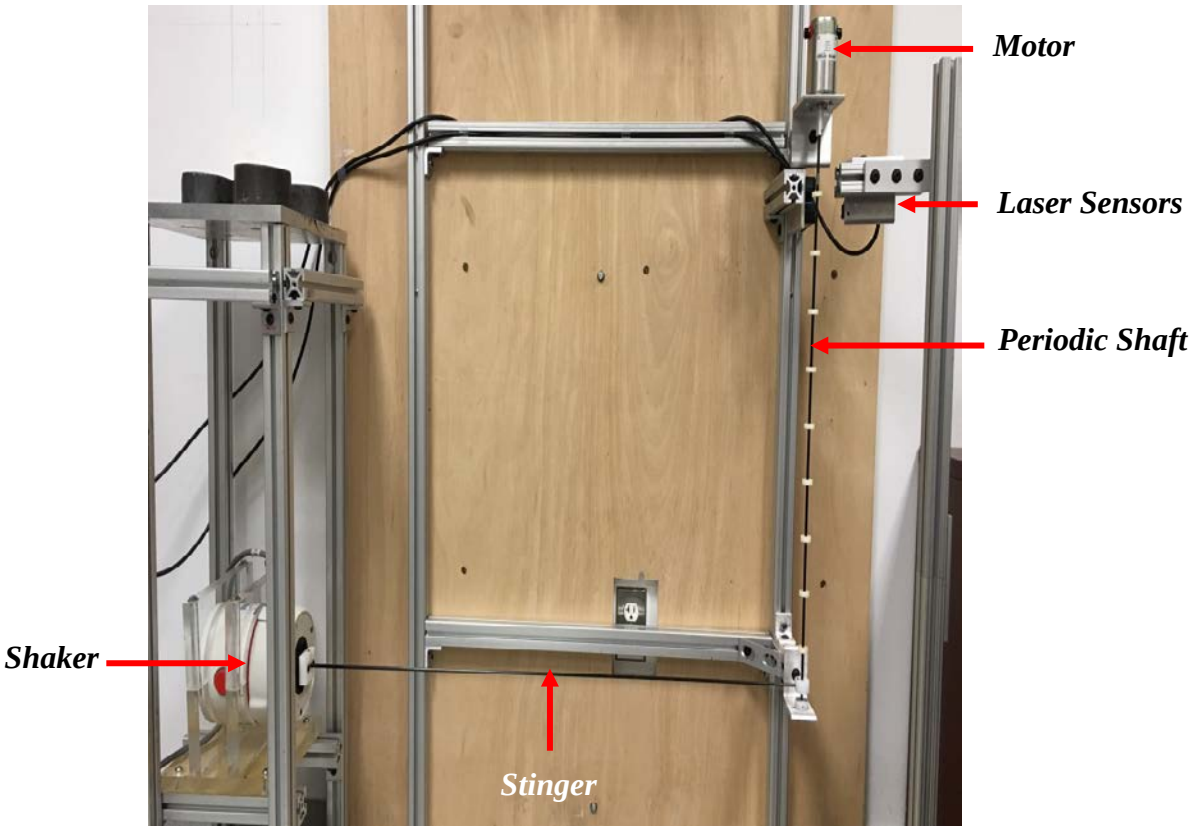

Figure (5.2) – Photograph of the experimental shaft setup

The spacing between the inner and outer rings of the periodic inserts with local sources of resonance is filled with 0.0625" thick *VEM* which is made from *DYAD* 606, (from Soundcoat Deer Park, NY 11729). The damping characteristics of *DYAD* 606 are displayed in Figure (5.3). The VEM has thermal shift factor α_T given by:

$$log_{10}(\alpha_T) = -\frac{12(T - T_0)}{291.67 + (T - T_0)}$$

where T denotes the operating temperature and T_0 defines the reference temperature (taken as T_0=80^oC).

The periodic inserts are manufactured by 3D stereolithography and a sample of these inserts is shown in Figure (5.4) from ABSplus-P430 (Stratasys.com, Eden Prairie, MN). The material has Young's modulus of 2.2 *GPa*, density of 1,040 kg/m^3, loss factor of 0.0046-0.0053, and glass transition temperature of 108^oC.

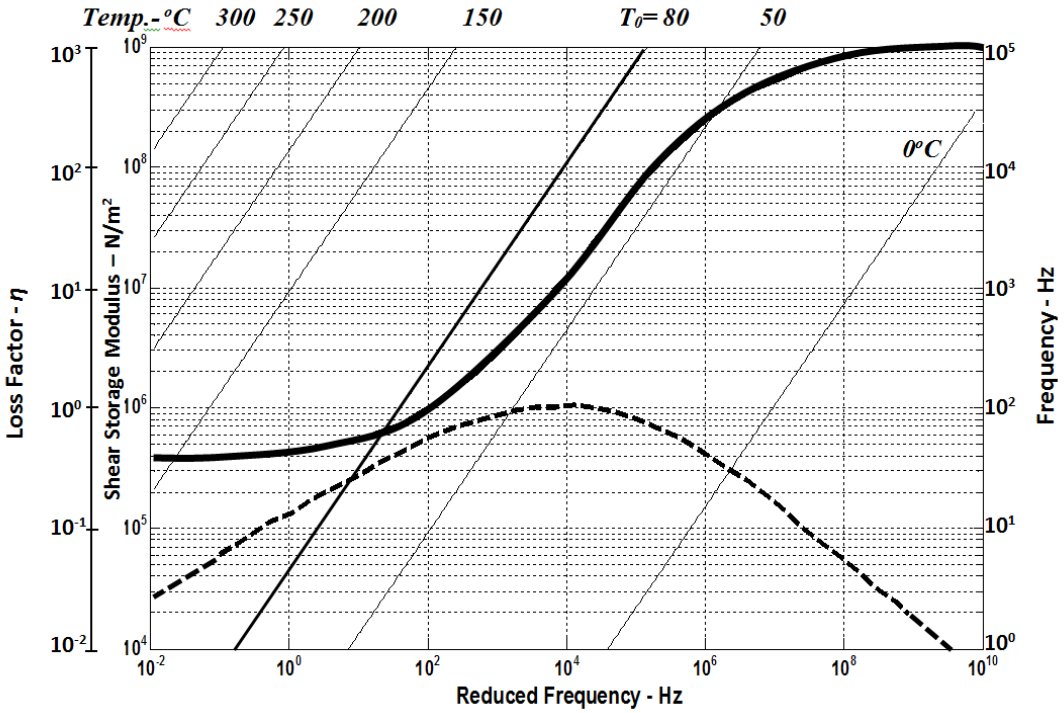

Figure (5.3) – Damping characteristics of the *VEM* core of the periodic inserts

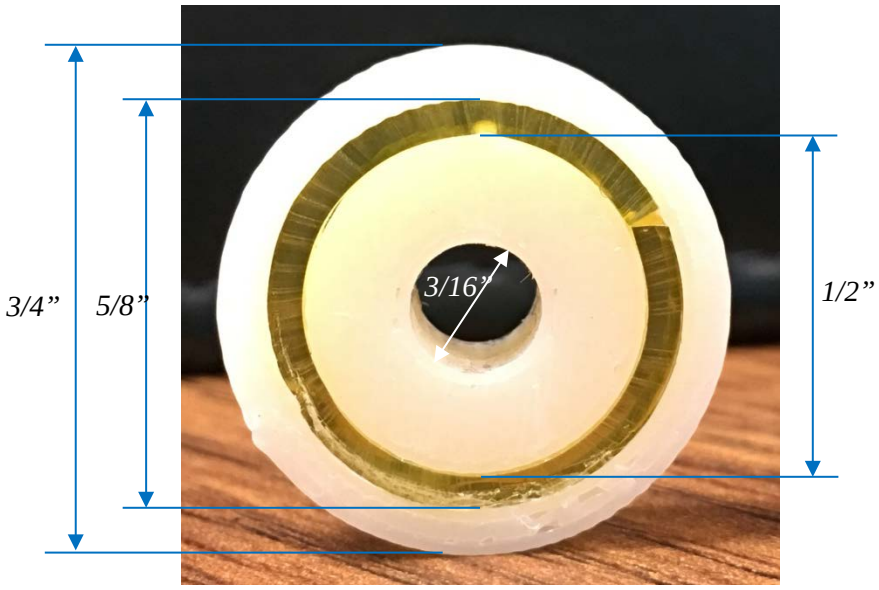

Figure (5.4) – Prototype of the periodic insert with local source of resonance as manufactured by stereolithography.

Figure (5.5) shows a photograph of the shaft with the periodic inserts and Figure (5.6) displays a photograph of the motor drive system and the position laser sensor respectively**.**

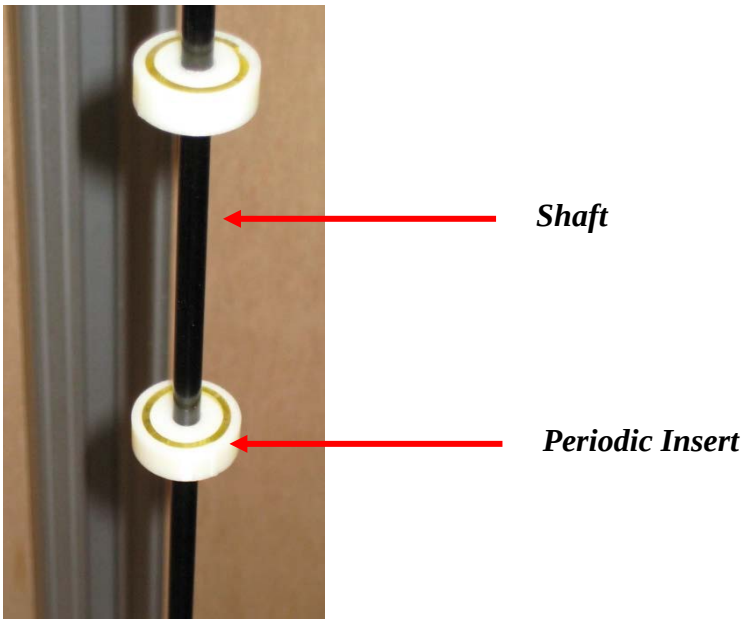

Figure (5.5) – Photograph of the periodic insert with local source of resonance as manufactured by stereolithography.

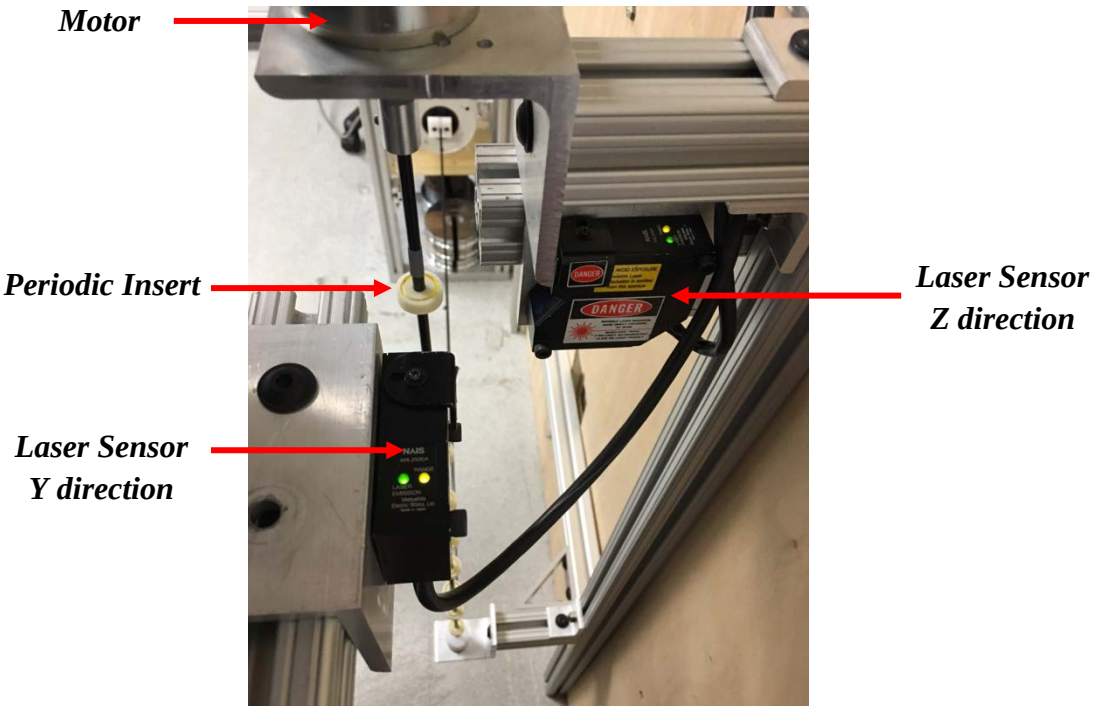

Figure (5.6) – Photograph of the motor drive system and the laser sensor

The specifications of the laser sensor, LM 200 (ANL2535REC), are listed in Figure (5.7). The sensor is manufactured by RAMCO, West Des Moines, Iowa 50265.

LM200

* Original NAIS Sensor

LM200 Series

Part No.	Measurable range (mm)	Resolution (μm)	Response time
ANL2335REC	30 (27 33)	1.5 5 15	30kHz 300kz 3kHz
ANL2535REC	50 (44 56)	4.5 15 45	30kHz 300Hz 3kHz

LM 200 Series

			ANL2335REC			ANL2535REC		
Center point distance			30mm			50mm		
Measurable range			±3mm			±6mm		
Light source			Laser diode, wavelength 670nm (pulse duration 8.3μs, 50% duty ratio)					
Laser protection class			Class 2 (Max. output 1.9mW)					
Analog displacement output	Output voltage		±3V/F.S. (0 to 6V/F.S. SW selectable) Max. 2mA					
	Output impedance		50Ω					
	Resolution (2σ)	White ceramic	1.5μm (30Hz)	5μm (300Hz)	15μm (3kHz)	4.5μm (30Hz)	15μm (300Hz)	45μm (3kHz)
		Gray ceramic						
	Linearity error *		Max. ±0.2% of F.S.					
	Material error **		Max. ±0.5% of F.S.					
	Zero-point adjustment range		10% of F.S.					
	Temperature drift		Sensor section: Max. ±(0.02% of F.S.)/°C Controller section: Max. ±(0.01% of F.S.)/°C					
	Response frequency (–3dB) Response time (10 to 90%)		3kHz 0.15ms	300Hz 1.5ms	30Hz 15ms	(SW selectable)		
Alarm output			Transistor output (NPN): 100mA, 30V DC (Open collector)					
Intensity output			0 to 4.5V					
Protective construction (sensor)			IP67					
Vibration resistance (when mounted with screws)			10 to 55Hz (1 cycle/min.), double amplitude		0.75mm (controller section) 1.5mm (sensor section)		2h on 3 axes	
Shock resistance (when mounted with screws)			Min. 20G, 3 times on 3 axes					
Ambient light level			Incandescent lamp: Max. 3,000 lux					
Ambient temperature			0°C to 50°C					
Storage temperature			–20°C to 70°C					
Ambient humidity			35% to 85%RH (without dew condensation)					
Rated operating voltage			100/110 to 120V AC, 200/220 to 240V AC (-15 to +10%)					
Rated power consumption			Max. 15VA					
Weight (including cable)			Sensor section: Approx. 320g			Controller section: Approx. 830g		

Notes

1. Unless otherwise specified, the measurement conditions are the rated operation voltage, 20°C ambient temperature, G in LOW, response 10Hz (LM100), 30Hz (LM200) and white ceramic as a target.
2. Center point distance:
   The distance from the front of laser emitting face to the center of measurable range

   F.S.: measurable range (ex. ANL1451REC: 20mm)

   Resolution:
   The standard devitation σ in the variation of the values measured at the center point distance should be doubled, and the result is converted into the distance.

Standard targets

	Diffuse reflection factor	Glossiness
White ceramic	95%	3%
Gray ceramic	17%	2%
Rolled steel plate	29%	69%
Copper	43%	15%
Aluminium	56%	37%
Black rubber	5%	8%

* The value when a target is measured in the range of ± 2mm for ANL2335REC and ± 4mm for ANL2535REC. The linearity error characteristics outside this range correspond to those of the material error. And when the value is represented by the displacement from the center point (CP), the formula of the linearity error is ± 6μm plus ± 0.2% x Distance from CP (ANL2335REC), ±12μm plus ±0.2% x Distance from CP (ANL2535REC).

** The value is based on standard targets. And when the value is represented by the displacement from the center point (CP), the formula of the material error is ± 15μm plus ± 0.5% x Distance from CP (ANL2335REC), ±30μm plus ±0.5% x Distance from CP (ANL2535REC).

Figure (5.7) - Specifications of the shaft deflection laser sensor, LM 200 (ANL2535REC)

5.3 Experimental Results

The frequency response of the shaft with periodic insert with local source of resonance generated using an electromechanical shaker (*LDS* – V4-08, Burel and Kjaer) which excites the shaft through a sleeve located near the lower fixed end of the shaft as shown in Figure (5.8). The response of the shaft is monitored using the laser sensor (LM 200 - ANL2535REC), which is located near the upper end of the shaft as indicated in Figure (5.8).

The shaft used in this study is manufactured from carbon fibers with density 1,400 kg/m^3 and Yong's modulus 80 *GPa* (*ACP* Composites, Livermore, CA)

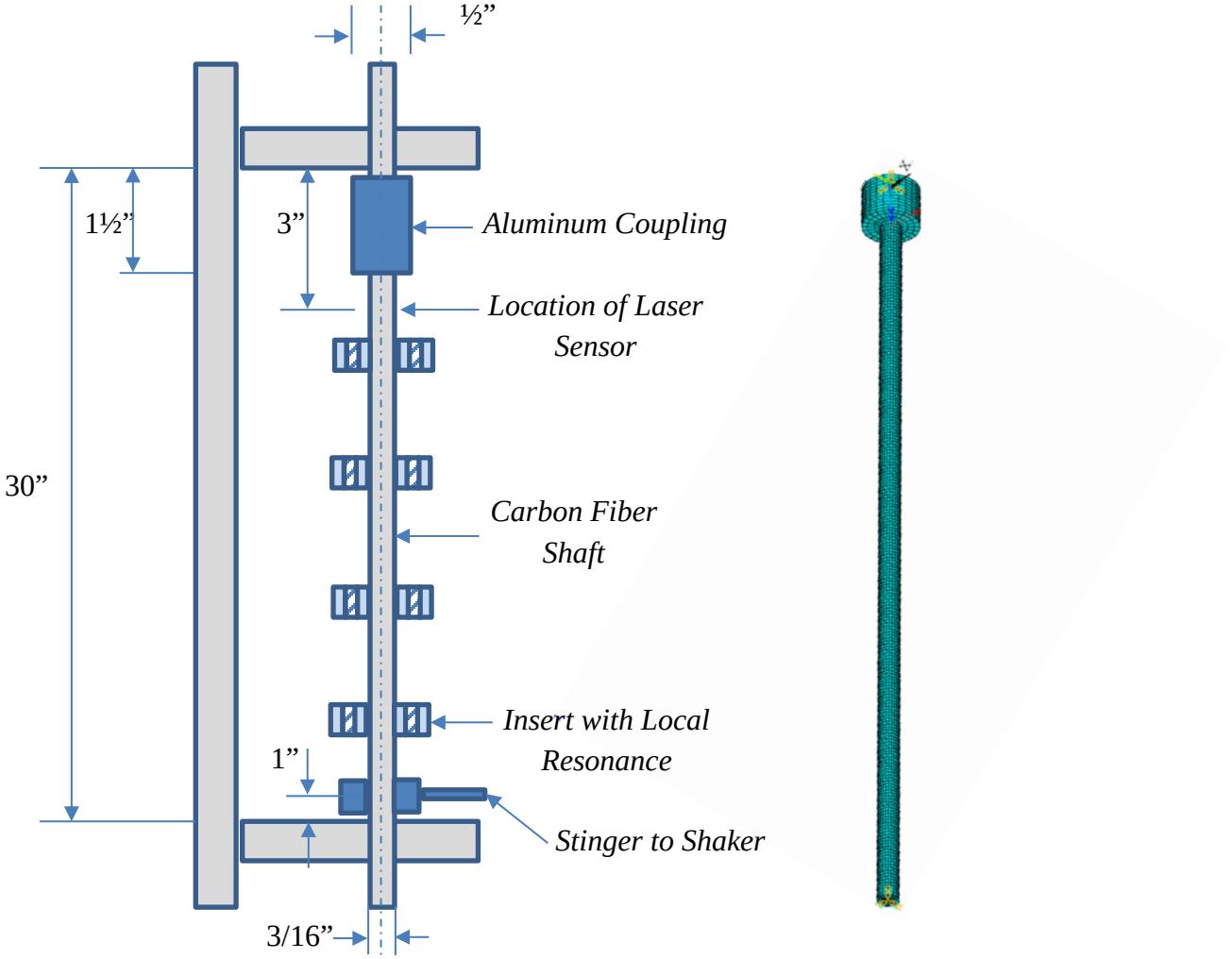

(a) – schematic drawing **(b) – The *FEM***

Figure (5.8) – Locations of the excitation and vibration measurement of the shaft/periodic sources of local resonance

The specifications of the electromechanical shaker are listed in Table 5.1.

Table 5.1 - Specifications of the electromechanical shaker

Shaker	**V408**
Standard LDS Amplifier	**PA500L**
Sine Force (peak) – forced air cooled	196 N
Armature Resonance (f_n)	9 kHz
Useful Frequency Range	5 Hz – 9 kHz
Effective Mass of Moving Element	0.200 kg
Velocity (sine peak)	1.78 m/s
Maximum Acceleration (sine peak) – naturally cooled	50 g
Maximum Acceleration (sine peak) – forced air cooled	100 g
Max. Random Force (rms)	89 N
Displacement (pk–pk) – continuous	17.6 mm
Suspension Axial Stiffness	12.3 N/mm
Aux. Suspension Axial Stiffness	35.1 N/mm
Shaker Body Mass – base mounted	14.1 kg
Shaker Body Mass – trunnion mounted	22.7 kg
Impedance at 500 Hz	2.5 Ω
Cooling Air Flow	0.014 m^3/s
Armature Diameter	38 mm
Armature Insert Pattern:	
Centre Insert	1
2.54 mm PCD†	6
Insert Threads	10/32 UNF

Figure (5.9) displays the frequency response of the shaft that has 10 periodic inserts with local resonance as compared to a uniform shaft.

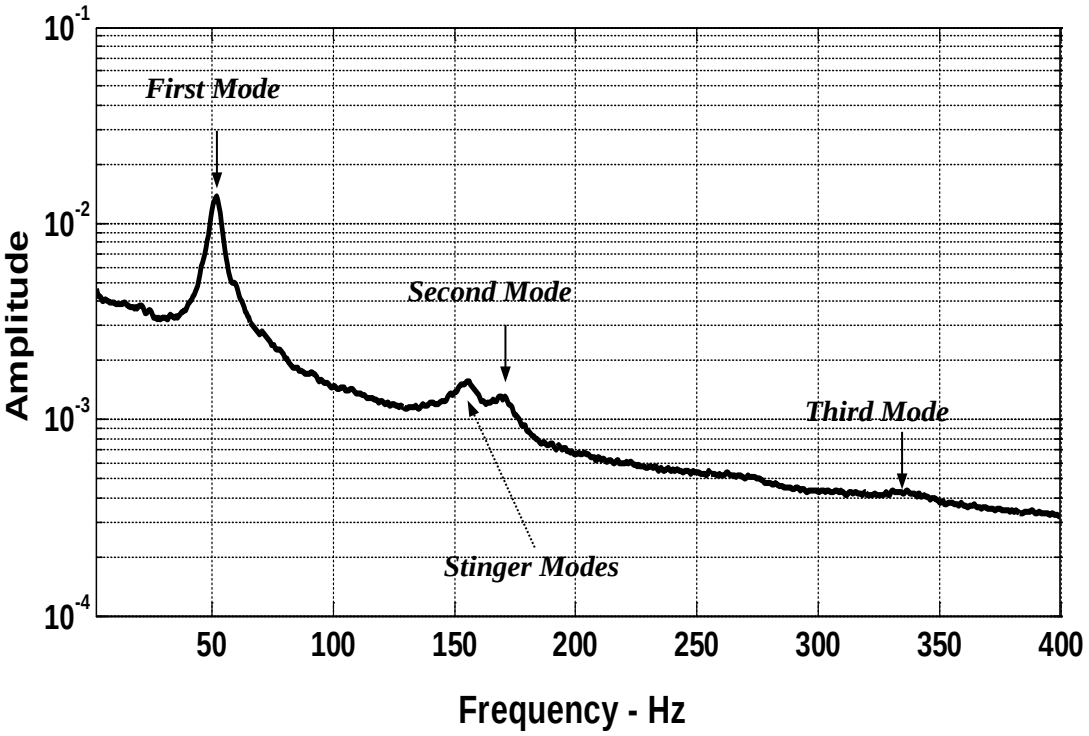

Figure (5.9) – Frequency response of a uniform shaft at 0 *rpm*

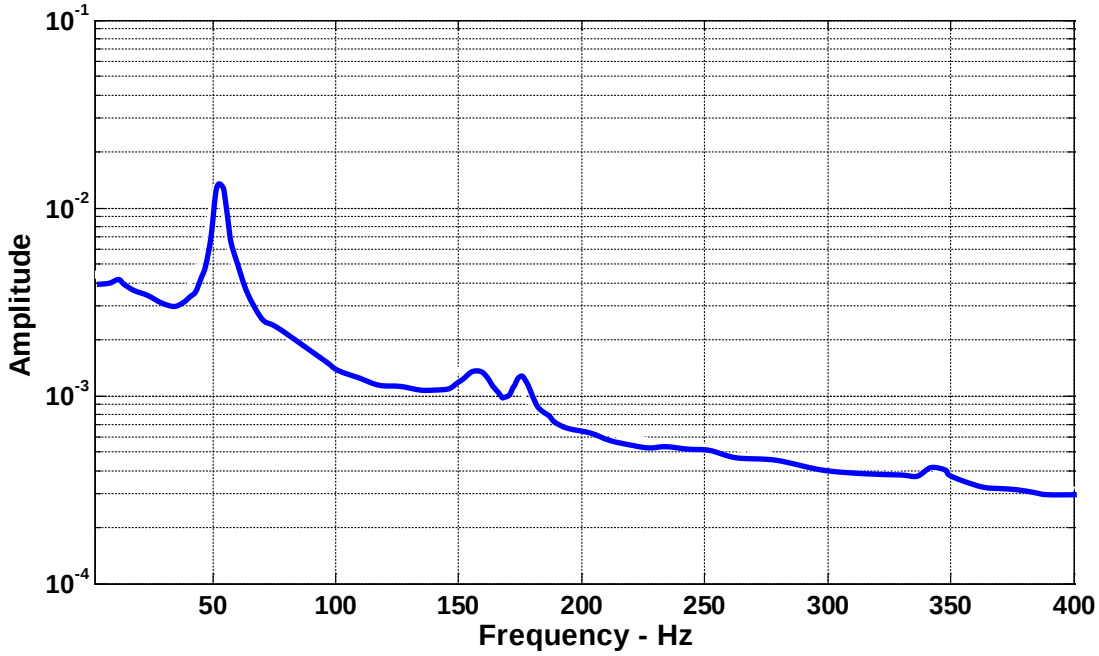

Figure (5.10) – Frequency response of a uniform shaft at 750 *rpm*

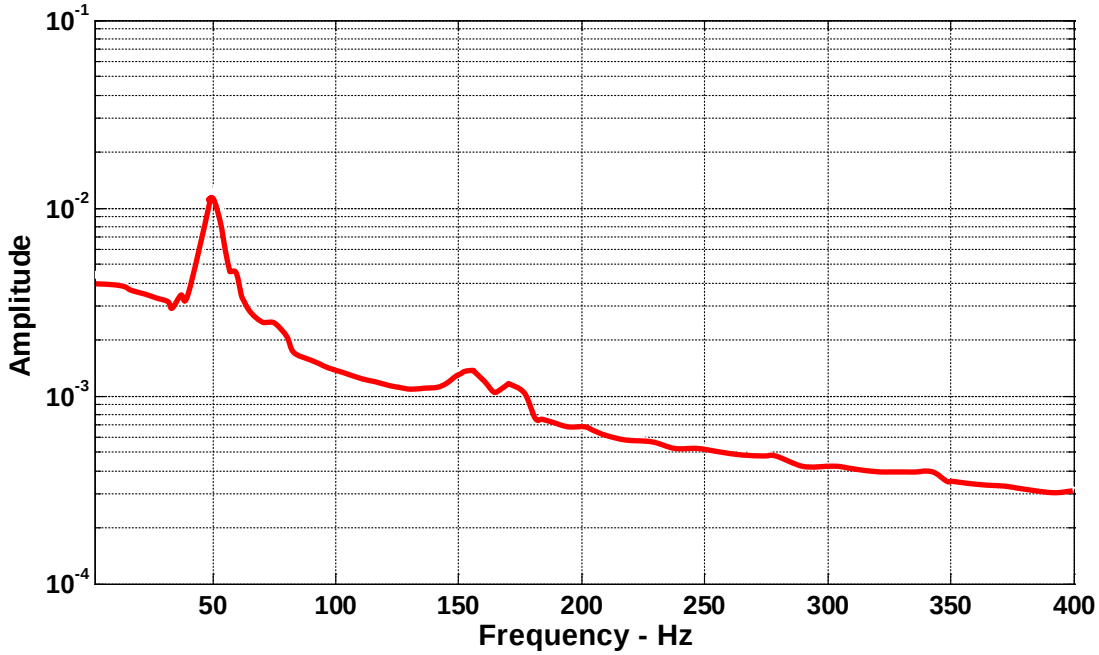

Figure (5.11) – Frequency response of a uniform shaft at 1500 *rpm*

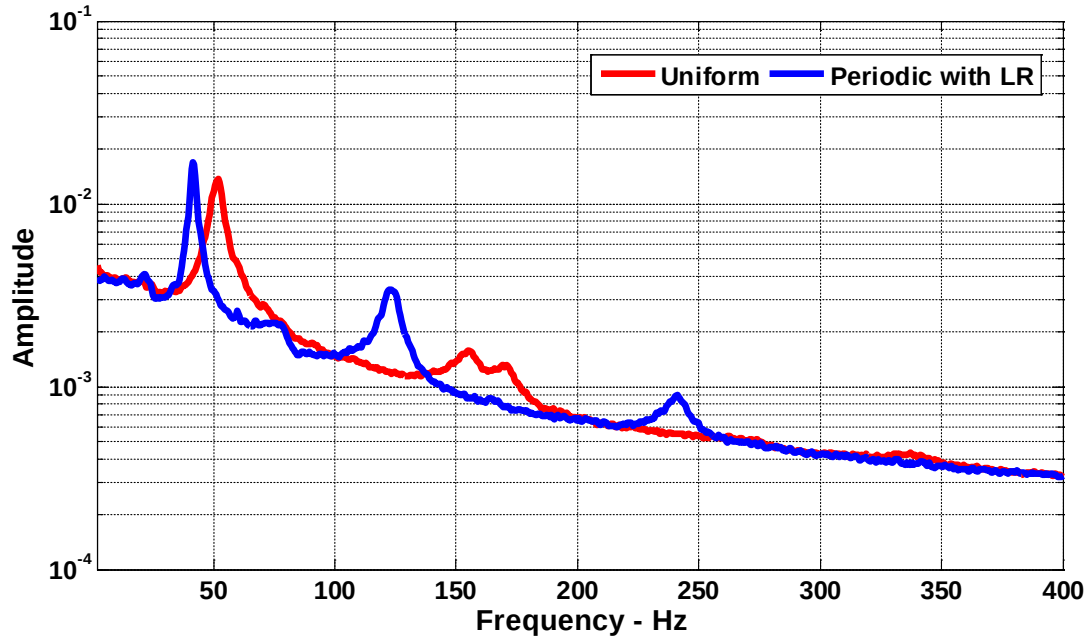

Figure (5.12) – Frequency response of a shaft that has 9 periodic inserts with local resonance as compared to a uniform shaft at 0 rpm.

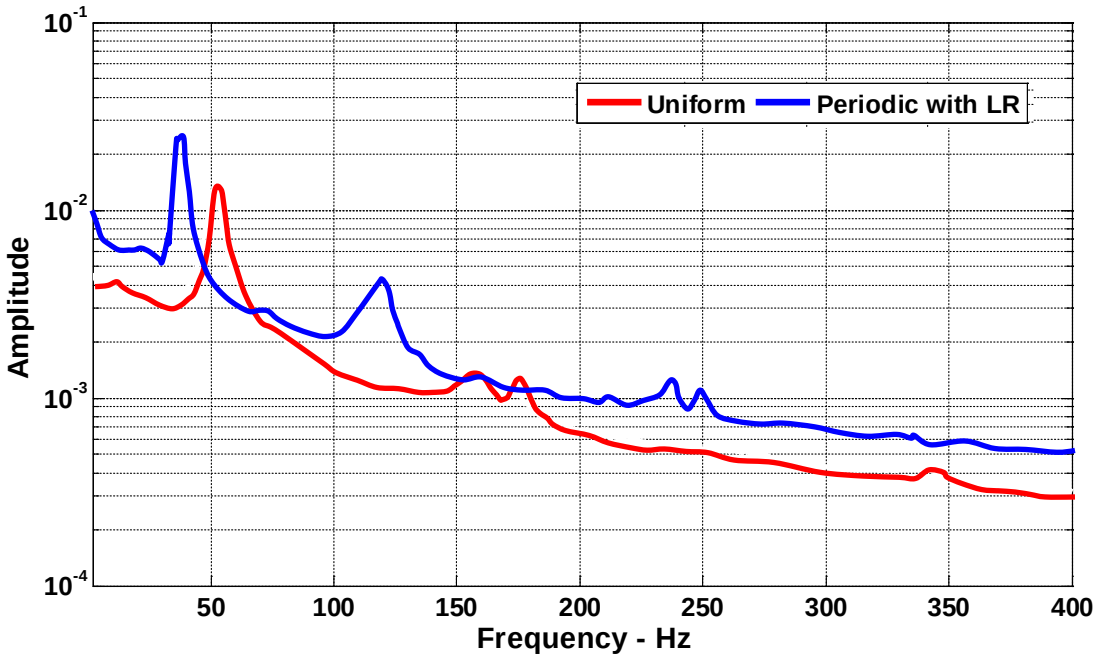

Figure (5.13) – Frequency response of a shaft that has 9 periodic inserts with local resonance as compared to a uniform shaft at 750 rpm.

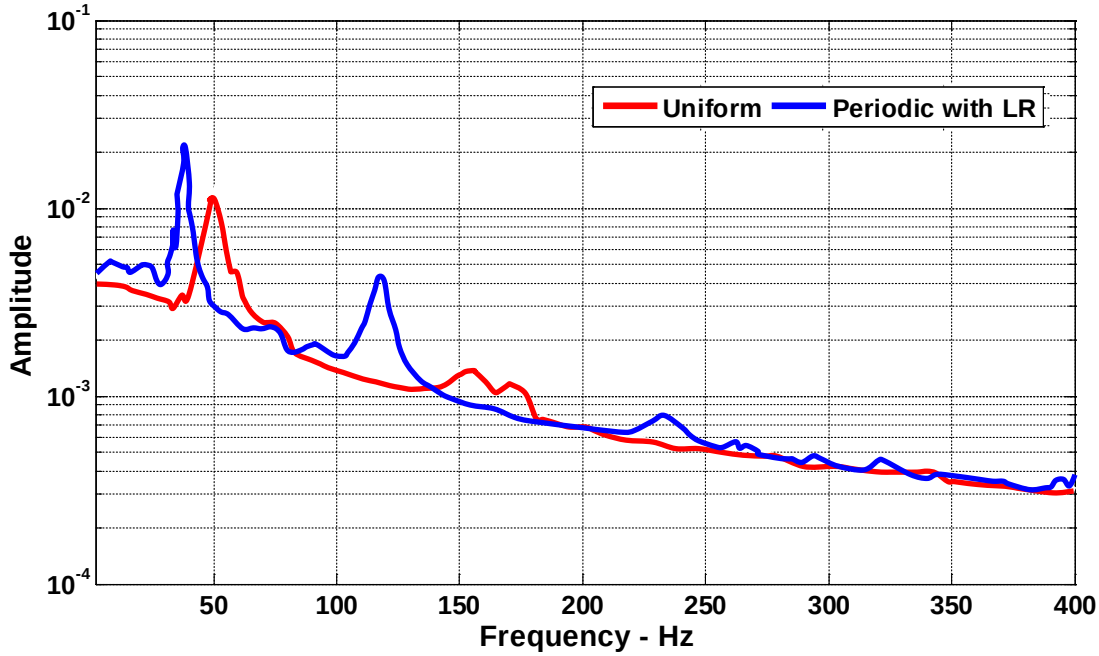

Figure (5.13) – Frequency response of a shaft that has 9 periodic inserts with local resonance as compared to a uniform shaft at 1500 rpm.

5.4. Modal Characteristics of the Shaft

Table 5.2 lists the natural frequencies of the uniform shaft as predicted by MATLAB FEM and ANSYS in comparison with the experimental results. It is evident that there is close agreements between the predictions of the finite element models and the experimental results.

Figure (5.14) displays the mode shapes corresponding to the first three natural frequencies of the uniform shaft

Table 5.2 – Comparison between the natural frequencies of the uniform shaft as determined by *MATLAB FEM, ANSYS* and experimentally

Mode	**1**	**2**	**3**
MATLAB *FEM* - *Hz*	**51.97**	**170.70**	**334.30**
ANSYS* – *Hz	**50.43**	**165.20**	**320.50**
Experimental - *Hz*	**51.00**	**171.00**	**336.50**

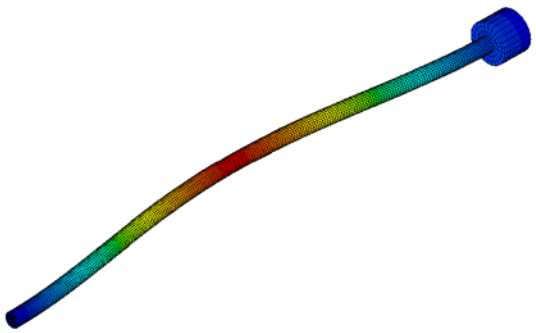

(a) – First mode (50.42 Hz)

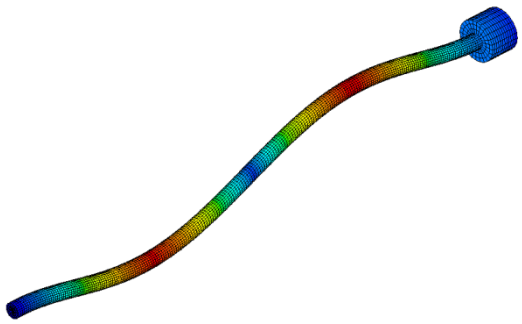

(b) - Second mode (165.20 Hz)

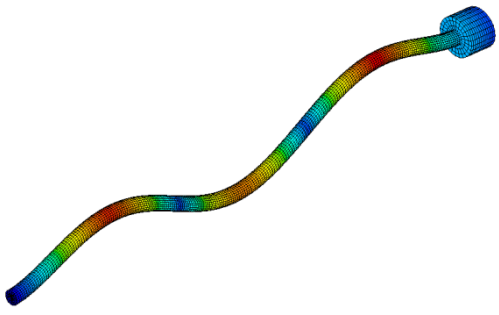

(c) – Third mode (320.50 Hz)

Figure (5.14) – The mode shapes of the first three natural frequencies of the uniform shaft

Figure (5.14) displays the frequency response of the uniform shaft as predicted by the finite element at speed of zero rpm.

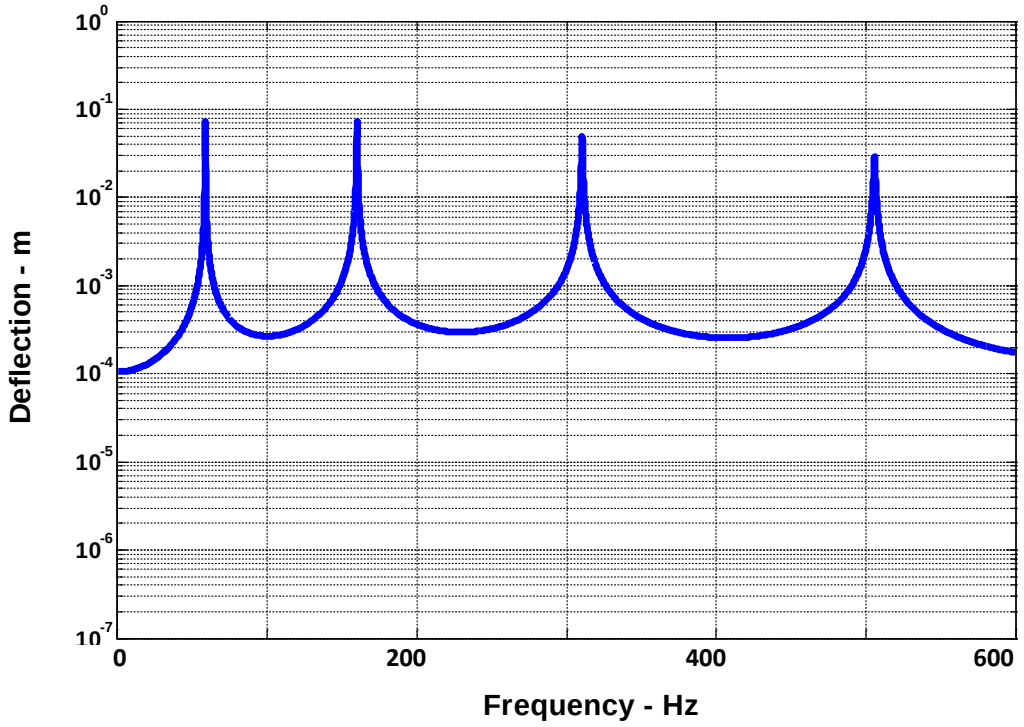

Figure (5.15) - Frequency response of the uniform shaft as predicted by the finite element at speed of zero *rpm*

Figure (5.16) displays the finite element of the periodic shaft with local sources of resonance.

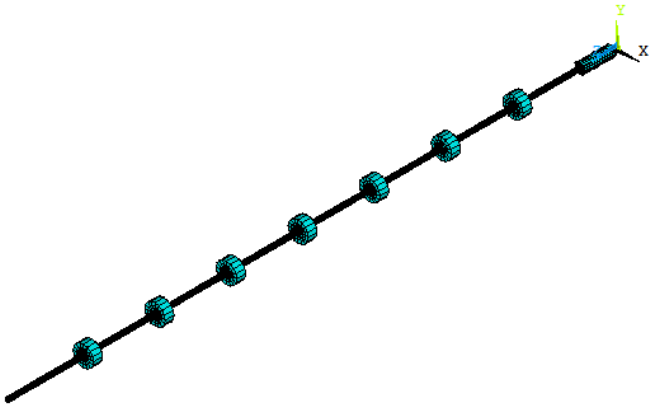

Figure (5.16) – Finite element of the periodic shaft with local sources of resonance.

Figures (5.17) and (5.18) display the frequency response of periodic shaft with local sources of resonance which are made of *ABS* and steel respectively.

The displayed results indicate that the use of the steel sources of local resonance has resulted in extending the stop bands to lower frequencies.

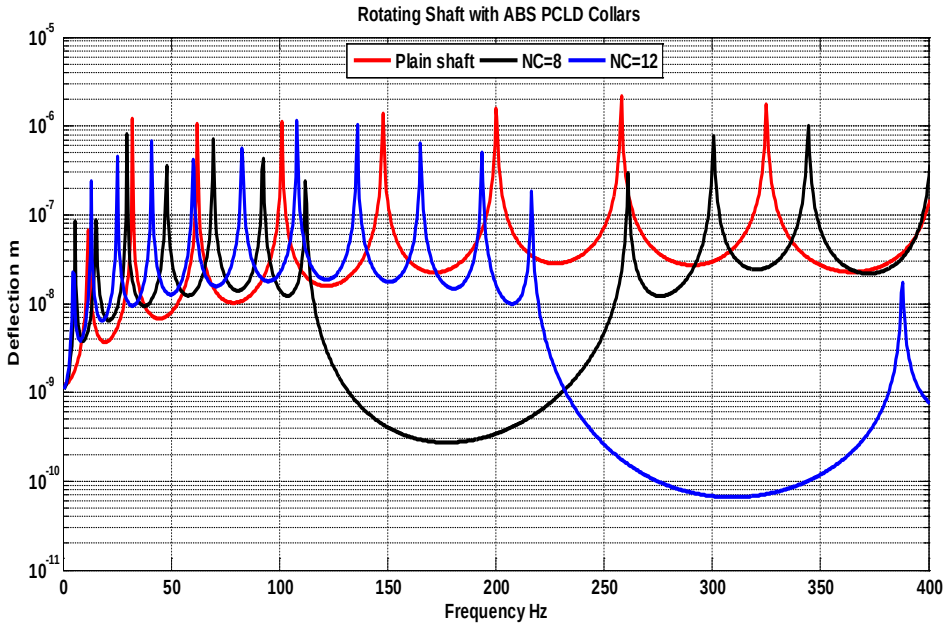

Figure (5.17) – Effect of number of periodic sources of ABS local resonance on the frequency response of the periodic shaft.

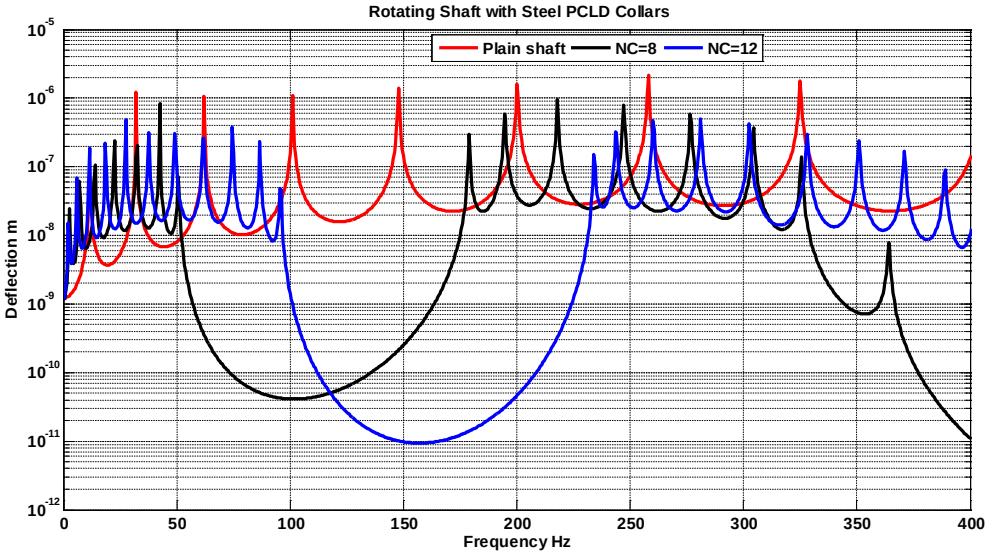

Figure (5.18) – Effect of number of periodic sources of steel local resonance on the frequency response of the periodic shaft.

5.5. Modified Design of the Shaft with Periodic Steel Sources of Local Resonance

According to the computations presented in section 5.4, the experimental shaft is provide with a set of steel inserts/*Dyad* 606 *VEM/ABS* constraining layer as shown in Figures (5.19) and (5.20).

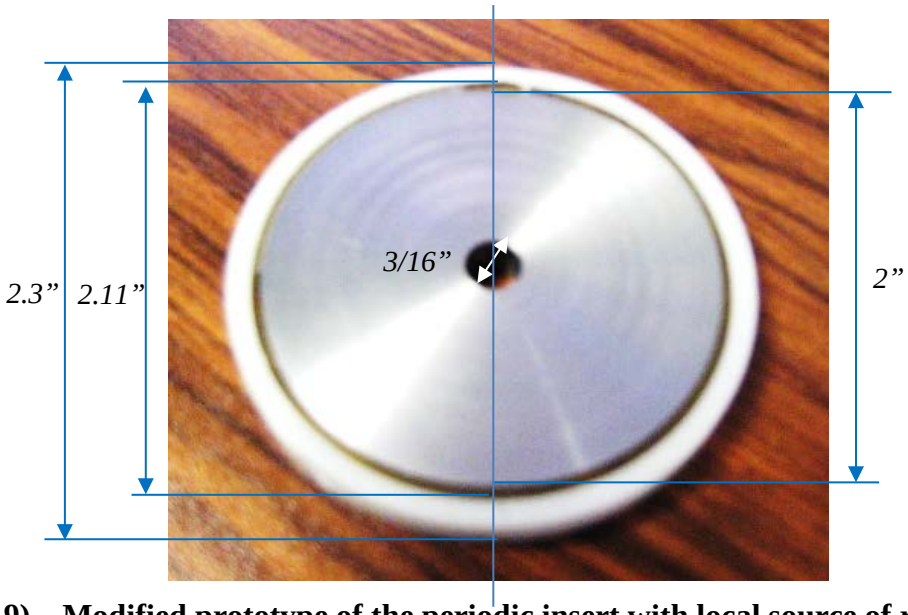

Figure (5.19) – Modified prototype of the periodic insert with local source of resonance as manufactured by stereolithography.

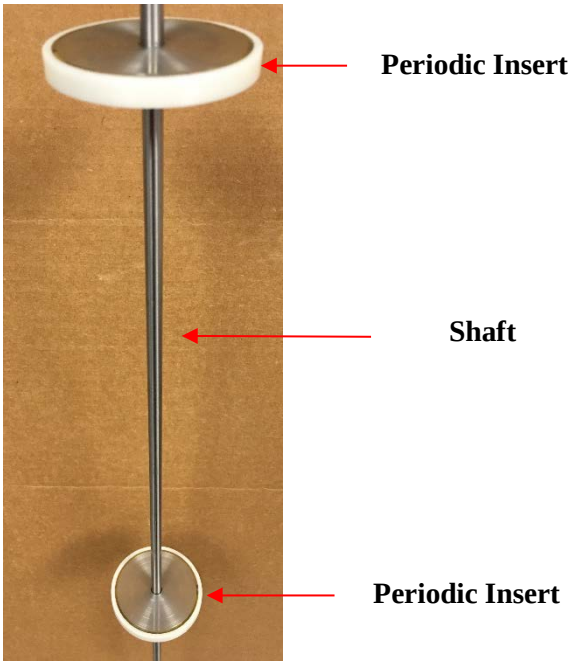

Figure (5.20) – Photograph of the shaft with modified periodic insert/local source of resonance assembly

The frequency response characteristics of the uniform shaft are determined using the excitation procedure outlined in Figure (5.8). These characteristics are shown in Figure (5.21). It can be seen that the shaft experiences continuous vibration over the considered frequency band from 0-200Hz. This band represent a continuous "*Pass Band*".

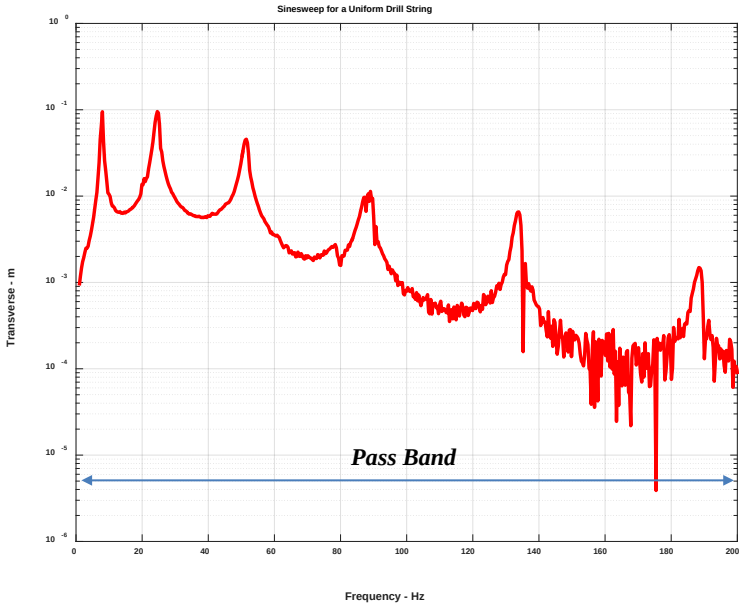

Figure (5.21) – Frequency response of the uniform shaft

The above characteristics are compared with those of the shaft when it is provided with 5 periodic *LR* inserts as displayed Figure (5.22).

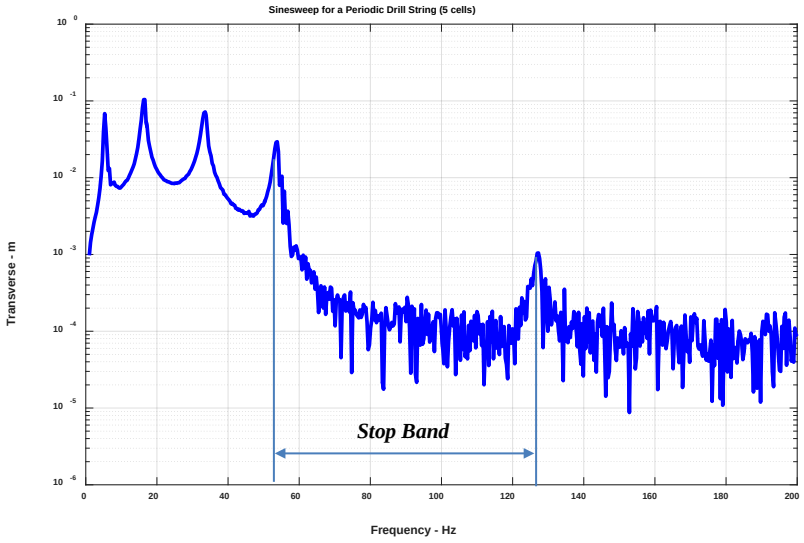

Figure (5.22) – Frequency response of the shaft with 5 periodic *LR* inserts

It can be seen from Figure (5.22) that the response exhibits a very wide "*stop band*" extending from 55Hz-126Hz. This demonstrated clearly the effectiveness of the proposed concept in mitigating the vibration experienced by the drillstring particularly if it is excited within the stop band.

Figure (5.23) displays comparison between the frequency responses of a shaft with 5 periodic *LR* inserts and a shaft with periodic inserts to emphasize the importance of including the *VEM* in the sources of *LR* to achieve effective vibration characteristics.

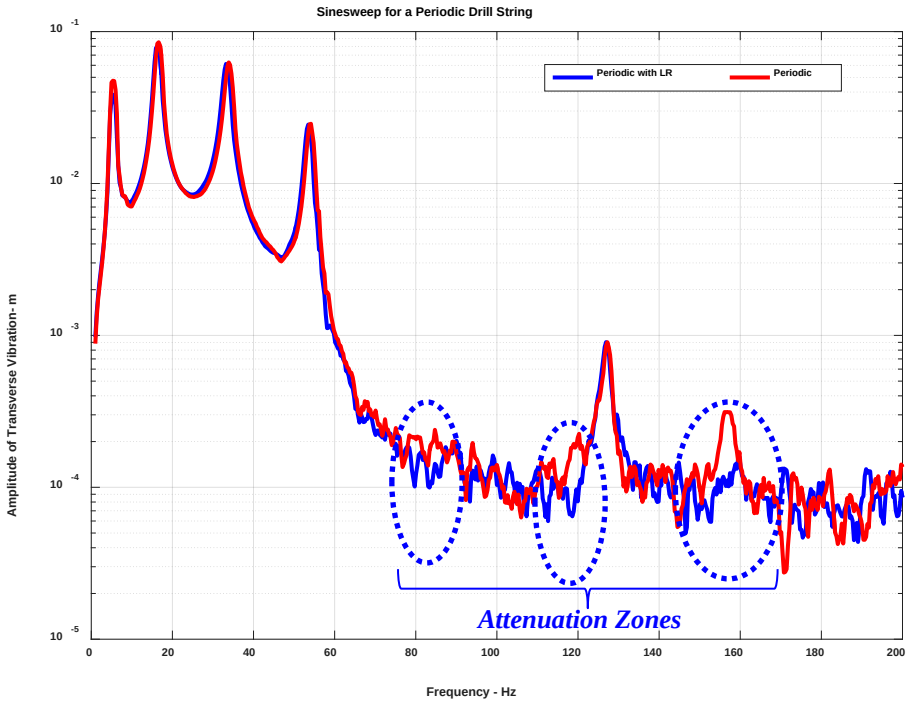

Figure (5.23) – Comparison between the frequency responses of a shaft with 5 periodic LR inserts and a shaft with periodic inserts

5.6. Summary

This chapter has presented a set of experimental results obtained by using prototypes of the uniform shaft and a shaft with sources of local resonance.

Particular emphasis has been placed on replacing the *VEM* by softer material to enhance the local damping characteristics. Also, the material of the rings of the sources of local resonance

has been replaced by steel instead of *ABS* as the finite element predictions shown in Figures (5.17) and (5.18) demonstrated that the use of steel rings is more effective than the *ABS* rings.

The experimental results are presented for modified inserts with *LR* to demonstrate clearly the effectiveness of the proposed concept in mitigating the vibration experienced by the drillstring particularly if it is excited within the stop band.

Furthermore, it has been demonstrated through comparisons between the frequency responses of a shaft with 5 periodic *LR* inserts and a shaft with periodic inserts that it is important to include the *VEM* in the sources of *LR* to achieve effective vibration mitigation characteristics.

Chapter 6: Conclusions and Future Recommendations

6.1 Overview

This chapter summarizes the conclusions arrived at and the recommended future work which may be need to expand the utility of the concepts proposed in this dissertation.

Included also in this chapter are the major contributions of the dissertation in relation to the current state-of-the-art.

6.2. Conclusions

This dissertation has presented a novel extension of the current state-of-the-art of the field of periodic structures by developing a class of rotating structures with periodic inserts with sources of local resonance in order to the control of the vibration of rotating shafts and drillstrings. Such a development constitutes the major contribution of this dissertation.

The development of such a class of structures involved the development of a finite element model (*FEM*) to describe the dynamics and vibrations of rotating structures at different rotating speeds. The developed *FEM* is exercised to generate the equivalent transfer matrix method of the rotating structures. The transfer matrices are utilized to study the pass and stop band characteristics of the rotating structures as influenced by the design parameters of the local sources of resonances under undamped conditions. For damped conditions, the theory of Bloch wave theory is employed to study the effect of the wave number on the resonant frequencies and damping ratio of the unit cell. Such an approach is also utilized to extract the shop bands of the drillstring with *LR* inserts.

It is demonstrated that the proposed class of periodic structures have enhanced ability of operating over frequency bands that are wider than those possible with conventional periodic structures.

The effectiveness of the proposed periodic inserts with local resonances are demonstrated numerically. The predictions of the numerical models have also been validated experimentally for prototypes of the rotating shafts.

Comparisons have also been established between the performance of the proposed periodic inserts with local resonances and that of conventional periodic inserts in order to emphasize the potential and merits of the proposed approach.

In chapter 2, the development of a finite element model is presented to describe the dynamics and vibration of rotating shafts with periodic inserts with local resonances. The model development involved the derivation of expressions of the potential and kinetic energies of the shaft assembly. Expressions of the energy dissipated in the damping treatments and the work done by all external forces acting on the shaft assembly have also been developed and integrated with the expressions of the potential and kinetic energies using the Lagrange dynamics approach. This approach is employed to extract the equations of motion of the shaft assembly. The resulting equations of motion are exercised to predict the performance characteristics of the shaft assembly at different rotational speeds and design parameters. The emphasis is placed on determining the model parameters of the assembly, the stop and pass band behavior, and Campbell diagram.

The predicted characteristics are validated, in chapter 3, against the predictions of the commercial finite element code *ANSYS*. The established comparisons aim at demonstrating the effectiveness of the drillstrings with periodic *LR* inserts in simultaneously controlling the axial, bending, and torsional modes of vibration of practical drillstrings particularly at low excitation frequencies. Such effectiveness stems from the ability of the periodic local sources of resonance in shifting the zones of the stop bands to low frequencies which are compatible to the frequencies experienced by practical drillstrings.

The favorable filtering characteristics of the drillstrings with periodic *LR* inserts are achieved when the *VEM* are tuned to have storage moduli that can coincide with the frequencies of the drillstrings. Stop bands are obtained at frequencies as low as 5 Hz which makes the application of the proposed concept practical for many of the existing drillstrings

Furthermore, the developed finite element model has been utilized to extract the transfer matrix of the assembly as is outlined in chapter 4 in order to validate the predictions of the stop and pass band behavior of the shaft system. The transfer matrix method is applied to undamped periodic drillstrings whereas the Bloch wave theory is employed for drillstrings with damped *LR* inserts.

In chapter 5, further validation of the predictions of the *FEM* will be carried out against the performance of experimental prototype of the rotating shaft. The obtained experimental results are presented for modified inserts with *LR* to demonstrate clearly the effectiveness of the proposed concept in mitigating the vibration experienced by the drillstring particularly if it is excited within the stop band.

Furthermore, it has been demonstrated through comparisons between the frequency responses of a shaft with 5 periodic *LR* inserts and a shaft with periodic inserts that it is important to include the *VEM* in the sources of *LR* to achieve effective vibration mitigation characteristics.

6.3. Future Recommendations

Although this dissertation has offered a major extension to the state-of-the art in the field of mitigation of the vibration of drillstrings, it has presented new opportunities for extending this

work in many directions to ensure the practical application and successful transition to the oil fields.

Among the potential directions is the natural extension of the presented work is the need to integrate the developed finite element model with active control means to ensure tenability of the proposed concept to various operating conditions and speeds.

Further work is needed to study the effect of the nonlinear interactions between the drillstring and the rock formation of the system stability. Studying the effect of the loading and operating conditions on the orbits of the drillstring and its convergence to attraction manifolds and avoiding any undesirable chaotic vibrations is essential to prove the viability of the proposed concept. Such investigations should be supported both from theoretical and experimental points of views.

The effect of the rotation speed of the drillstring on its vibration and stop band characteristics has to be demonstrated experimentally and theoretically. Further interest should focus on studying the effect of axial loading on the vibration, orbits, and stop band characteristics.

Parametric studies are needed to investigate the effect of the design parameters of the *LR* inserts on the vibration, orbits, and stop band characteristics.

More comparisons should be established between the vibration of conventional drillstring and conventional periodic drillstings in order to quantify the merits and effectiveness of the proposed concept of periodic drillstring with inserts that have built-in sources of local resonance.

6.4. Major Contributions of the Dissertation

This dissertation has presented the concept of drillstrings with periodic inserts that have built-in sources of local resonance along with their performance characteristics.

The comprehensive presentation of the periodic drillstrings through mathematical modeling and experimental realization and evaluation emphasizes the following major contributions of the work to the current state-of-the-art of vibration mitigation of drillstrings:

1. The concept of drillstrings with periodic inserts that have built-in sources of local resonance is original and has not been considered at all in the open-literature for application to drillstrings.
2. The comprehensive theoretical and experimental demonstration of the effectiveness of the concept of drillstrings with periodic inserts that have built-in sources of local resonance in mitigating the low-frequency vibration of drillstrings is one of the major contributions of this dissertation.

3. The ability of the periodic inserts that have built-in sources of local resonance in the simultaneous control of the torsional, axial and transverse bending vibrations is another important contribution of the dissertation.

6.5. Summary

This chapter has summarized the conclusions arrived at and the recommended future work which needs to be carried out to ensure practical application and technology transfer of the proposed concepts. The dissertation has successfully demonstrated theoretically and experimentally the viability of the proposed concept of drillstrings with periodic *LR* inserts in effectively mitigating the vibration of the drillstings in the axial, torsional, and bending modes.

In this chapter several directions of future work are proposed to naturally extend the presented work both experimentally and theoretically. These future directions aim at gaining better insight in the fundamental behavior of the drillstring and broaden the understanding of the underlying physical phenomena involved in the operation of the drillstring with periodic inserts that have built-in sources of local resonances.

The chapter has included also are the major contributions of the dissertation in relation to the current state-of-the-art.

REFERENCES

Aarrestad T. V., Tonnesen H. A., and Kyllingstad A., "Drillstring Vibrations: Comparison Between Theory and Experiments on a Full-Scale Research Drilling Rig," *Proceedings of SPE/ADC 14760 Drilling Conference*, February 10-12, Dallas, TX, 1986.

Ahmadabadi Z. N. and Khadem S. E., Self-excited oscillations attenuation of drill-string system using nonlinear energy sink, *Proceedings of the Institution of Mechanical Engineers, Part C: Journal of Mechanical Engineering Science*, Vol. 227, No. 2 pp.230-245, 2013.

Aldushaishi M. F., "Investigation of drillstring vibration reduction tools", *Master Thesis*, Missouri University of Science and Technology, 2012

Al-Hiddabi S. A., Samanta B. and Seibi A., "Non-linear control of torsional and bending vibrations of oilwell drillstrings ", *Journal of Sound and Vibration*, Vol. 265, No. 2, pp. 401-415, 2003.

ANSI/IEEE, 1987, "Standard on Piezoelectricity," ANSI/IEEE STD No. 176-1987.

Asiri S., Baz A., and Pines D., "Active Periodic Struts for a Gearbox Support System", *Journal of Smart Materials and Structures*, Vol. 15, pp. 1707–1714, 2006.

Asiri S., Baz A., and Pines D., "Periodic Struts for Gearbox Support System", *Journal of Vibration and Control*, Vol. 11, No. 6, pp. 709-721, 2005.

Baz, **A.** "Active Control of Periodic Structures", *ASME Journal of Vibration and Acoustics*, Vol. 123, pp. 472-479, 2001.

Bazoune A., Khulief Y. A., and Stephen N. G., "Shape Functions of Three-Dimensional Timoshenko Beam Element", *Journal of Sound and Vibration*, Vol. 259, No. 2, pp. 473-480, 2003.

Besaisow A. and Payne M., "A Study of Excitation Mechanisms and Resonances Inducing Bottomhole-Assembly Vibrations", *SPE Drilling Engineering*, Vol. 3, No. 1, 93–101, 1988.

Boussaada I., Mounier H., Niculescu S. I. and Cela A., "Analysis of drilling vibrations: a time-delay system approach", Paper# ThA1.4, 2012 *20th Mediterranean Conference on Control & Automation* (MED), Barcelona, Spain, July 3-6, 2012

Chen L. H. and Huang S. C., "Vibration attenuation of a cylindrical shell with constrained layer damping strips treatment," *Computers and Structures*, Vol. 79, 2001, pp. 1355-1362.

Chen S. L. and Géradin M., " An improved transfer matrix technique as applied to *BHA* lateral vibration analysis ", *Journal of Sound and Vibration*, Vol.185, No. 10 , pp. 3-106,1995.

Christoforou A. P. and Yigit A. S., "Fully coupled vibrations of actively controlled drillstrings", *Journal of Sound and Vibration*, Vol. 267, No. 5, pp. 1029-1045, 2003.

Choi S. H., Pierre C. and Ulsoy A. G. " Consistent modeling of rotating Timoshenko shafts subject to axial loads", *ASME Journal of Vibration and Acoustics*, Vol. 114, pp. 249-259,**1992.**

Christoforou A. P. and Yigit A. S., " Dynamic modeling of rotating drillstrings with borehole interactions", *Journal of Sound and Vibration*, Vol. 206, No. 2, pp. 243-260, 1997.

Downton G.C., "Challenges of modeling drilling systems for the purposes of automation and control", Paper# FrPIT3.2, *Proceedings of the 2012 IFAC Workshop on Automatic Control in Offshore Oil and Gas Production*, Norwegian University of Science and Technology, Trondheim, Norway, May 31 - June 1, 2012

El-Raheb M. and Wagner P., "Damped response of shells by a constrained viscoelastic layer," *ASME Journal of Applied Mechanics*, Vol. 53, 1994, pp. 902-908.

Esmaeili A. , Elahifar B. , Fruhwirth R.K., and Thonhauser G. , Axial vibration monitoring in laboratory scale using CDC miniRig and vibration sensor sub, *2012 IEEE International Instrumentation and Measurement Technology Conference* (I2MTC), 13-16 May 2012, pp. 512-517, 2012.

Ghasemloonia A., Rideout D. G. and Butt S. D., "Coupled transverse vibration modeling of drillstrings subjected to torque and spatially varying axial load", *Proc. IMechE Part C: J. Mechanical Engineering Science*, Online 2013.

Ghoneim H., and Lawrie D. J., "Analysis of flexural vibration of a composite drive shaft with a cylindrical constrained layer damping", *Smart Structures and Materials 2004*, edited by K.W. Wang, Proc. Of SPIE Vol. 5386, pp.132-140, 2004.

Golla D. F., and Hughes P. C., "Dynamics of Viscolelastic Structures-A Time Domain Finite Element Formulation", *ASME Journal of Applied Mechanics*, Vol. 52, pp. 897-600, 1985.

Hoie B., "Drillstring oscillations during connections when drilling from a semi-submersible platform", Master Thesis, Stavanger University, Stavanger, Norway, 2012.

Hu Y. C. and Huang S. C., "A linear theory for three-layer sandwich shell vibration," *ASME conference, Active Control of Vibration and Noise*, DE-Vol 93, 1996, pp. 229-238.

Huang H. H., and Sun C. T., "A study of band-bang phenomena of two locally resonant acoustic metamaterials", *Proc. of IMechE Part N: J. of Nanoengineering and Nanosystems*, Vol. 224, pp. 83-92, 2011.

Hussein M. I., and Frazier M. J., "Metadamping: An emergent phenomenon in dissipative metamaterials", *Journal of Sound and Vibration*, Vol. 332, pp. 4767-4774, 2013.

Hussein M. I.,"Theory of damped Bloch waves in elastic media," *Physical Review B*, Vol. 80, p. 212301, December 2009.

Hussein M. I. and Frazier M. J., "Band structure of phononic crystals with general damping," *Journal of Applied Physics*, Vol. 108, p. 093506, November 2010.

Jansen J. D. and van den Steen L., "Active damping of self-excited torsional vibrations in oil well drillstrings ", *Journal of Sound and Vibration*, Vol. 179, No. 4, , pp. 6-668, 1995.

Jansen J. D., "Non-linear rotor dynamics as applied to oilwell drillstring vibrations", *Journal of Sound and Vibration*, Vol. 147, No. 1, pp. 115-135, 1991.

Karkoub M., Zribi M., Elchaar L., and Lamon L., "Robust μ -synthesis controllers for suppressing stick-slip induced vibrations in oil well drillstrings", *Multibody System Dynamics*, Vol. 23, pp. 191–207, 2010.

Khulief Y. A. and Al-Naser H., "Finite element dynamic analysis of drillstrings", *Finite Elements in Analysis and Design*, Vol. 41 , No. 13, pp. 1270 - 1288 , 2005.

Khulief Y.A., Al-Sulaiman F.A., and Bashmal S., "Vibration analysis of drillstrings with self-excited stick-slip oscillations", *Journal of Sound and Vibration*, Vol. 299, No. 3, pp. 540–558, 2007.

Khulief Y.A., Al-Sulaiman F.A., and Bashmal S., "Vibration analysis of drillstrings with string–borehole interaction, *Proc. IMechE Part C: J. Mechanical Engineering Science*, Vol. 222, pp. 2099-2110, 2008.

Khulief Y.A. and Al-Sulaiman F.A., "Laboratory investigation of drillstring vibrations", *Proc. IMechE Part C: J. Mechanical Engineering Science*, Vol. 223, pp. 2249-2262, 2009.

Kim W., Argento A., and Scott R. A., "Forced vibration and dynamic stability of a rotating tapered composite Timoshenko shaft: bending motions in end-milling operations," *Journal of Sound and Vibration*, Vol. 246 (4), 2001, pp. 563-600.

Leine R. I., van Campen D. H., Keultjes W. J. G., "Stick-slip Whirl Interaction in Drillstring Dynamics", *Journal of Vibration and Acoustics*, Vol. 124, pp. 209-220, 2002.

Li L., Zhang Q., and Rasol N., "Time-varying sliding mode adaptive control for rotary drilling system", *Journal of Computers*, Vol. 6, No. 3, pp. 564-570, 2011.

Liu Z., Chan C. T., and Sheng P., "Analytic model of phononic crystals with local resonances", *Phys. Rev. B*, 71 (2005) 014103.

Liu, X., Vlajic, N., Long, X., Meng, G., and Balachandran, B., "State-Dependent Delay Influenced Drill-String Oscillations and Stability Analysis," *ASME Journal of Vibration and Acoustics*, Vol. 136(5), pp. 051008-1-051008-9, 2014a.

Liu, X., Vlajic, N., Long, X., Meng, G., and Balachandran, B., "Coupled Axial-Torsional Dynamics in Rotary Drilling with State-Dependent Delay: Stability and Control," *Nonlinear Dynamics*, Vol. 78, pp. 1891-1906, 2014b.

Meirovitch L., *Fundamentals of Vibration*, Waveland, Long Grove, IL, 2010

Melakhessou H., Berlioz A., and Ferraris G., "A Nonlinear Well-Drillstring Interaction Model," *ASME Journal of Vibration and Acoustics*, Vol. 125, No. 1, pp. 46-52, 2003.

Mihajlovic N., van de Wouw N., Hendriks M. P. M. and Nijmeijer H., "Friction-induced limit cycling in flexible rotor systems: An experimental drill-string set-up", *Journal Nonlinear Dynamics*, Vol. 46, No. 3, pp. 273-291, 2006.

Mihajlovic N., "Torsional and Lateral Vibrations in Flexible Rotor Systems with Friction" Ph.D. Dissertation, Eindhoven: Technische Universiteit Eindhoven, 2005.

Milton G. W., and Willis J. R., "On modifications of Newton's second law and linear continuum elastodynamics", *Proc. R. Soc. A* , Vol. 463, pp. 855–880, 2007.

Moradi H., Bakhtiari-Nejad F. and Sadighi M., Suppression of the bending vibration of drill strings via an adjustable vibration absorber, *International Journal of Acoustics and Vibration*, Vol. 17, No. 3, pp. 155163, 2012.

Napolitano K. L., Grippo W., Kosmatka J. B., and Johnson C. D., "A comparison of two cocured damped composite torsion shafts," *Composite Structures*, Vol. 43, 1998, pp. 115-125.

Qin Q. H. and Mao C. X., "Coupled Torsional-Flexural Vibration of Shaft Systems in Mechanical Engineering-I. Finite Element Model", *Computers & Structures*, Vol. 58. No. 4, pp. 835-843. 1996

Ritto T. G., Sampaio R., and Soize C., "Drill-string nonlinear dynamics accounting for drilling fluid", *30º CILAMCE-Iberian-Latin-American Congress on Computational Methods in Engineering*, Armação dos Búzios, RJ : Brazil, 2009a.

Ritto T.G., Soize C., and Sampaio R., "Nonlinear dynamics of a drill-string with uncertain model of the bit-rock interaction", *International Journal of Non-Linear Mechanics*, Vol. 44, No.8, pp. 865-876, 2009b.

Ritto T.G., Soize C., and Sampaio R., "Stochastic dynamics of a drill-string with uncertain weight-on-hook", *Journal of the Brazilian Society of Mechanical Sciences and Engineering*, Vol. 32, No. 3, pp.250-258, 2010.

Ritto T.G., Escalante M.R., Sampaio R., Rosales M.B., Drill-string horizontal dynamics with uncertainty on the frictional force, *Journal of Sound and Vibration*, Vol. 332, No.1, pp. 145-153, 2013.

Sarker M. M., Rideout D. G., and Butt S. D., "Advantages of an *LQR* controller for stick-slip and bit-bounce mitigation in an oilwell drillstring", Paper# IMECE2012-87856, *Proceedings of the ASME 2012 International Mechanical Engineering Congress & Exposition* IMECE2012 November 9-15, 2012, Houston, Texas, USA.

Singh S. P., and Gupta K., "Composite shaft rotordynamic analysis using a layerwise theory," *Journal of Sound and Vibration*, Vol. 191(5), 1996, pp. 739-756.

Smith N., "Vibration of a hollow cylindrical shells with partial constrained layer damping", M.Sc., Rochester Institute of Technology, Rochester, NY, 2004.

Song O., Limbrescu L., and Jeong N-H, "Vibration and stability control of smart composite rotating shaft via structural tailoring and piezoelectric strain actuation," *Journal of Sound and Vibration*, Vol. 257(3), 2002, pp. 503-525.

Spanos P.D., Chevallier A.M., Politis N. P. and Payne M.L., "Oil and Gas Well Drilling: A Vibrations Perspective", *The Shock and Vibration Digest*, Vol. 35, No. 2, pp. 85–103, 2003.

Toso M., Baz A. and Pines D., "Active vibration control of periodic rotating shafts", paper# IMECE2004-61514, *Proceedings of IMECE, 2004 ASME International Mechanical Engineering Congress*, Anaheim, CA, November 2004.

Utkin, V., *Sliding Modes in Control Optimization*, Springer-Verlag, Berlin, 1992.

van de Vrande B. L., van Campen D. H., and de Kraker A., "An Approximate Analysis of Dry-Friction-Induced Stick-Slip Vibrations by a Smoothing Procedure", *Nonlinear Dynamics* 19: 157–169, 1999.

Yang T. Y., *Finite Element Structural Analysis*, Prentice Hall, Englewood Cliffs, New Jersey, 1986.

Yigit A. S. and Christoforou A. P., "Coupled torsional and bending vibrations of actively controlled drillstrings ", *Journal of Sound and Vibration*, Vol. 234, No.1, pp. 67-83, 2000.

Yigit A. S. and Christoforou A. P., "Coupled torsional and bending vibrations of drillstrings subject to impact with friction", *Journal of Sound and Vibration*, Vol. 215, No. 1, pp. 167-181, 1998.

Yigit A. S. and Christoforou A. P., "Coupled axial and transverse vibrations of oil well drillstrings ", *Journal of Sound and Vibration*, Vol.195, No. 29, pp. 617-627, 1996.

Zhu X. Z., He Y. D., Chen L., and Yuan H. Q., Nonlinear dynamics analysis of a drillstring-bit-wellbore system for horizontal oil well, *Advanced Science Letters*, Vol. 16, No. 1, pp. 13-19, 2012.

Zhu X. and Lai C. Design and performance analysis of a magnetorheological fluid damper for drillstring, *International Journal of Applied Electromagnetics and Mechanics*, Vol. 40, No. 1, pp.67-83, 2012.